

AD A113698

**RADC-TR-82-16**  
Final Technical Report  
February 1982



12

## **USERS CODE FOR THE FINITE-DIFFERENCE TIME-DOMAIN METHOD**

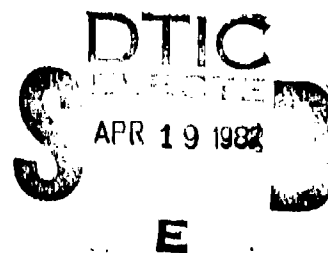
**IIT Research Institute**

**Dr. Allen Taflove**  
**Dr. Korada Umashankar**

APPROVED FOR PUBLIC RELEASE; DISTRIBUTION UNLIMITED

ITTC FILE COPY

**ROME AIR DEVELOPMENT CENTER**  
**Air Force Systems Command**  
**Griffiss Air Force Base, New York 13441**



82 04 19 002

This report has been reviewed by the RADC Public Affairs Office (PA) and is releasable to the National Technical Information Service (NTIS). At NTIS it will be releasable to the general public, including foreign nations.

RADC-TR-82-16 has been reviewed and is approved for publication.

APPROVED: *Daniel E. Warren*

DANIEL E. WARREN  
Project Engineer

APPROVED: *David C. Luke*

DAVID C. LUKE, Colonel, USAF  
Reliability & Compatibility Division

FOR THE COMMANDER: *John P. Huss*

JOHN P. HUSS  
Acting Chief, Plans Office

If your address has changed or if you wish to be removed from the RADC mailing list, or if the addressee is no longer employed by your organization, please notify RADC (RBCT) Griffiss AFB NY 13441. This will assist us in maintaining a current mailing list.

Do not return copies of this report unless contractual obligations or notices on a specific document requires that it be returned.

UNCLASSIFIED

SECURITY CLASSIFICATION OF THIS PAGE (When Data Entered)

REPORT DOCUMENTATION PAGE		READ INSTRUCTIONS BEFORE COMPLETING FORM
1. REPORT NUMBER RADC-TR-82-16	2. GOVT ACCESSION NO. AD-113598	3. RECIPIENT'S CATALOG NUMBER
4. TITLE (and Subtitle) USERS CODE FOR THE FINITE-DIFFERENCE TIME- DOMAIN METHOD		5. TYPE OF REPORT & PERIOD COVERED Final Technical Report 30 Sep 80 - 30 Sep 81
		6. PERFORMING ORG. REPORT NUMBER N/A
7. AUTHOR(s) Dr. Allan Taflove Dr. Korada Umashankar		8. CONTRACT OR GRANT NUMBER(s) F30602-80-C-0302
9. PERFORMING ORGANIZATION NAME AND ADDRESS IIT Research Institute 10 West 35th Street Chicago IL 60616		10. PROGRAM ELEMENT, PROJECT, TASK AREA & WORK UNIT NUMBERS 64747F 20640308
11. CONTROLLING OFFICE NAME AND ADDRESS Rome Air Development Center (RBCT) Griffiss AFB NY 13441		12. REPORT DATE February 1982
		13. NUMBER OF PAGES 111
14. MONITORING AGENCY NAME & ADDRESS (if different from Controlling Office) Same		15. SECURITY CLASS. (of this report) UNCLASSIFIED
		16. DECLASSIFICATION/DOWNGRADING SCHEDULE N/A
18. DISTRIBUTION STATEMENT (of this Report) Approved for public release; distribution unlimited.		
17. DISTRIBUTION STATEMENT (of the abstract entered in Block 20, if different from Report) Same		
19. SUPPLEMENTARY NOTES RADC Project Engineer: Daniel E. Warren (RBCT)		
20. KEY WORDS (Continue on reverse side if necessary and identify by block number) Electromagnetic Coupling Electromagnetic Compatibility Aperture Coupling Time Domain Solutions Finite Difference Techniques		
20. ABSTRACT (Continue on reverse side if necessary and identify by block number) Electromagnetic penetration and scattering problems are difficult to treat with many analytical or numerical methods because of the inability of these methods to simply deal with the effects of structure materials, apertures, curvatures, corners, and internal contents. In previous programs, a new approach for the direct modeling of very complex electromagnetic interaction problems was studied: the finite-difference, time-domain (FD-TD) solution of Maxwell's equations. The FD-TD method has key		

DD FORM 1 JAN 73 1473 EDITION OF NOV 68 IS OBSOLETE

UNCLASSIFIED

(Cont'd)

SECURITY CLASSIFICATION OF THIS PAGE (When Data Entered)

UNCLASSIFIED

SECURITY CLASSIFICATION OF THIS PAGE (When Data Entered)

Item 20 (Cont'd)

advantages relative to available modeling approaches. These advantages permit it to accurately treat complex problems that are beyond the scope of solution by any other method.

The goals of the present research program included the development of specific algorithms of high importance to help provide a flexible, simple-to-use, and highly accurate user-oriented FD-TD computer program. Five key improvements in the FD-TD algorithm were tested during this effort, including the following:

- (1) Total-field/scattered-field lattice division,
- (2) Variable angle of incidence,
- (3) Second-order accurate radiation condition,
- (4) Magnitude and phase computation condition for the sinusoidal steady state, and
- (5) Near-to-far field transformation.

Accession For	
NTIS GRA&I	<input checked="checked" type="checkbox"/>
DTIC TAB	<input type="checkbox"/>
Unannounced	<input type="checkbox"/>
Justification	
By	
Distribution/	
Availability Codes	
Dist	Avail and/or Special
A	



UNCLASSIFIED

SECURITY CLASSIFICATION OF THIS PAGE (When Data Entered)

## REPORT SUMMARY AND DISCUSSION

Electromagnetic penetration and scattering problems are difficult to treat with many analytical or numerical methods because of the inability of these methods to simply deal with the effects of structure materials, apertures, curvatures, corners, and internal contents. In two earlier RADC contracts, F30602-77-C-0163 and F30602-79-C-0039, IIT Research Institute (IITRI) investigated the application of a new approach for the direct modeling of very complex electromagnetic interaction problems: the finite-difference, time-domain (FD-TD) solution of Maxwell's equations. The FD-TD method has key advantages relative to available modeling approaches. These advantages permit it to accurately treat complex problems that are beyond the scope of solution by any other method. The ultimate aim of research in this area is to develop an accurate, easily-used, general computer program solving for either electromagnetic field penetration, scattering, or radiation for arbitrary metal/dielectric structures spanning up to 10 or more wavelengths in three dimensions with a spatial resolution better than 0.1 wavelength.

In order to more fully determine the usefulness of the FD-TD method, RADC thought it is desirable to distribute this technique to as wide a range of users as possible so that it can be tested by actual implementation. The overall objectives of algorithm development in this case are to allow RADC to write a user-oriented computer program for the FD-TD technique.

The goals of the present IITRI research effort for RADC, Contract F30602-80-C-0302, included the development of specific algorithms of high importance to help provide a flexible, simple-to-use, and highly accurate user-oriented FD-TD computer program. To meet these goals, IITRI tested five key improvements in the FD-TD algorithm during this effort, including the following:

1. Total-field/scattered-field lattice division.

This permits a very high computational dynamic range to accurately model fields within shadow zones or cavities. This further permits programming of variable angle of incidence and the second-order correct radiation condition, summarized below.

2. Variable angle of incidence.

For two-dimensional problems, this permits a single data card or Fortran statement to specify in a very accurate manner the angle of incidence of a plane wave illuminating a structure. For three-dimensional problems, both the angle of incidence and polarization could be specified. There is no requirement to rotate the geometry of the interacting structure in the FD-TD lattice.

3. Second-order accurate radiation condition.

This reduces the uncertainty of the final computed results by as much as ten-to-one. FD-TD computations using this radiation condition now have estimated field-magnitude uncertainties of better than  $\pm 2.5\%$  ( $\pm 0.2$  dB) versus previous uncertainties of  $\pm 10\%$ - $\pm 15\%$  ( $\pm 1$  dB).

4. Magnitude and phase computation condition for the sinusoidal steady state

This permits accurate determination of the magnitude and phase of FD-TD computed fields at any desired points for later use in computations involving scattering, radiation, or coupling to wires. This approach avoids any ambiguity due to either a possible DC offset of the fields or the repetitive nature of the sinusoidal waveform.

5. Near-to-far field transformation.

This permits the far scattered fields and radar cross section of arbitrary structures modeled by the FD-TD method to be easily and accurately determined. Observed accuracy of the radar cross section using this feature is in the order of  $\pm 1\%$  ( $\pm 0.09$  dB).

These FD-TD algorithm improvements are documented in this report. In addition to the algorithm improvements tested by IITRI, this report also summarizes a FD-TD feature which has recently appeared in the literature that permits computation of the coupling of currents to thin wires and struts.

The conclusions of this report are as follows:

1. The accuracy of the pure FD-TD method for electromagnetic interaction problems can reach the high levels previously attained only by method-of-moments (MOM) approaches when the second-order accurate radiation condition is used in the FD-TD algorithm. The FD-TD method retains its significant advantages over MOM in terms of the much larger electrical size and greater complexity of the structures that can be modeled.
2. The specification of variable angle of incidence and polarization of an illuminating wave can be achieved with the FD-TD method using only a single data card or Fortran statement.<sup>1</sup>

The total-field/scattered-field regional division of the FD-TD lattice can be successfully implemented and offers the significant advantage of a high computational dynamic range. In addition, this lattice division provides a framework for programming variable wave incidence and polarization, improved radiation conditions, and the near-field to far-field transformation for scattering problems.

4. The near-to-far field transformation along a rectangular virtual surface surrounding a scatterer makes it possible to use the FD-TD method to compute the far scattered fields and radar cross section of complex, arbitrary structures with great precision.

It is the opinion of the authors of this report that the FD-TD method deserves additional investigation to probe just what are the limits of application of this extremely promising approach to accurately model electromagnetic penetration, scattering, and radiation problems.

---

<sup>1</sup>This incident wave specification is now as simple for the FD-TD method as it has been with MOM. However, the FD-TD approach requires re-running the entire problem for each new incident wave angle. With MOM, only a single inversion of the system matrix is required. Subsequently, arbitrary wave excitation is treated as a simple matrix multiplication of the equivalent excitation vector. MOM therefore permits a conceptually simpler treatment of the variable wave incidence problem.

## PREFACE

IIT Research Institute (IITRI) is pleased to submit this Final Report on "User's Code for the Finite-Difference Time-Domain Method" to Rome Air Development Center (RADC/RBCT). The report covers work performed by IITRI under Air Force Contract No. F30602-80-C-0302, designated as IITRI Project No. E6502. This report covers details of the technical work, including relevant theory and numerical results. Appendix A provides a listing of the Fortran computer program used to obtain the results of this report.

The principal investigator on this program was Dr. Allen Taflove. The co-investigator was Dr. Korada Umashankar. The project duration was 1 September 1980 to 31 August 1981.

Respectfully submitted,

IIT RESEARCH INSTITUTE

*Allen Taflove*

Allen Taflove, Ph.D.  
Senior Engineer

APPROVED:

*Theodore A. Martin*

Theodore A. Martin  
Manager, EM Technology Section



## TABLE OF CONTENTS

	Page
REPORT SUMMARY AND DISCUSSION . . . . .	iii
PREFACE . . . . .	vi
1.0 INTRODUCTION . . . . .	1
2.0 THEORY AND BASIC ALGORITHMS OF THE FD-TD METHOD. . . . .	5
2.1 Ideas Behind the FD-TD Method . . . . .	5
2.2 Computational Details for a Uniform, Cubic Lattice. . . . .	12
2.2.1 Basic System of Equations. . . . .	12
2.2.2 Lattice Regions and Plane Wave Source Conditions . . . .	16
2.2.3 Lattice Truncation Conditions. . . . .	19
2.2.4 Sinusoidal Steady State Magnitude and Phase Information. . . . .	22
2.2.5 Far-Field Scattering Information via the Near-to-Far Field Transformation . . . . .	25
2.2.6 Penetrating Near Field Information via the Schelkunoff Aperture Electric Current Equivalence Principle. . . . .	31
2.2.7 Thin Wire Coupling Model . . . . .	36
3.0 EXAMPLES OF COMPUTED RESULTS OF THE FD-TD METHOD . . . . .	43
3.1 Pure FD-TD Method, Three-Dimensional Penetration Problems . .	43
3.1.1 Empty Cylindrical Metal Cavity, Broadside Incidence, Transverse Electric (TE) Polarization Case . . . . .	43
3.1.2 Loaded Missile Guidance Section, Axial Incidence Case. .	48
3.2 Hybrid MOM/FD-TD Method, Three-Dimensional Penetration Problem-- Loaded Missile Guidance Section, Axial Incidence Case. . . . .	52
3.3 Hybrid FD-TD Method, Two-Dimensional Scattering Problems. . .	57
3.3.1 Square Metal Cylinder, Normal (Broadside) Incidence, TM Polarization of Incident Wave . . . . .	57

TABLE OF CONTENTS (cont.)

	<u>Page</u>
3.3.2 Square Metal Cylinder, Oblique ( $45^\circ$ ) Incidence, TM Polarization of Incident Wave . . . . .	68
3.3.3 Verification of Near-to-Far Field Transformation for Circular Metal and Dielectric Cylinders. . . . .	76
4.0 SUMMARY AND CONCLUSIONS. . . . .	80
REFERENCES. . . . .	83
APPENDIX A-- Listing of Fortran Computer Program. . . . .	88

## LIST OF FIGURES

<u>Figure</u>		<u>Page</u>
1	Time-Domain Wave-Tracking Concept of the FD-TD Method . . . . .	6
2	Positions of the Field Components About a Unit Cell of the Yee Lattice. . . . .	8
3	Arbitrary Three-Dimensional Scatterer Embedded in a FD-TD Lattice. . . . .	9
4	Division of FD-TD Lattice Into Total-Field and Scattered- Field Regions . . . . .	17
5	Near-to-Far Field Transformation Geometry . . . . .	27
6	Geometry of Two-Dimensional Scattering, TM Polarization Case. .	30
7	Hybrid MOM/FD-TD Technique for Computing Penetration into Cavities. . . . .	34
8	Geometry for Computing the In-Cell Inductance of a Wire in a Cell of Rectangular Cross Section. . . . .	39
9	Partitioning $I^S$ into Current Densities $J_z^S$ at the Four Closest $E_z^S$ Mesh Points. . . . .	39
10	FD-TD Model Geometry of Open-Ended Aluminum Cylinder at Horizontal Symmetry Plane. . . . .	45
11	Transverse Cross Section of Cylinder Model of Figure 10 . . . . .	45
12	Comparison of Results for the Longitudinal Magnetic Field Along the Cylinder Axis of Figures 10 and 11. . . . .	46
13	FD-TD Computed Field Contours in Horizontal Symmetry Plane of Cylinder of Figures 10 and 11. . . . .	47
14	Geometry of Guidance Section Model at Vertical Symmetry Plane, Showing Component Materials. . . . .	49
15	Geometry of Guidance Section Model at Horizontal Observation Plane . . . . .	49
16	FD-TD Computed Field Contours in Vertical Symmetry Plane of Guidance Section of Figures 14 and 15. . . . .	51
17	Hybrid MOM/FD-TD Model of Loaded Missile Guidance Section for Axial Incidence Case. . . . .	53

# LIST OF FIGURES (cont.)

Figure		Page
18	Comparison of FD-TD and Hybrid MOM/FD-TD Data for $H_x$ Contours in Vertical Symmetry Plane. . . . .	54
19	Comparison of FD-TD and Hybrid MOM/FD-TD Data for Fields Along Vertical Cut Through Center of Guidance Section Near Sleeve-Fitting Aperture. . . . .	56
20	Geometry for Two-Dimensional Scattering Example: Square Conducting Cylinder Illuminated by a Plane Wave at Normal Incidence ( $\phi = 0^\circ$ ). . . . .	59
21a	Comparison of MOM and FD-TD Results for Magnitude of Electric Currents on Surface of Cylinder. . . . .	60
21b	Comparison of MOM and FD-TD Results for Phase of Electric Currents on Surface of Cylinder. . . . .	61
22a	Comparison of MOM and FD-TD Results for Near Electric Field Tangential to Contour $S_a$ . . . . .	62
22b	Comparison of MOM and FD-TD Results for Phase of Near Electric Field Tangential to Contour $S_a$ . . . . .	63
23a	Comparison of MOM and FD-TD Results for Near Magnetic Field Tangential to Contour $S_a$ . . . . .	64
23b	Comparison of MOM and FD-TD Results for Phase of Near Magnetic Field Tangential to Contour $S_a$ . . . . .	65
24	Equivalence of Computed Results for Radar Cross Section Obtained Using the MOM Surface Currents Approach and the Hybrid FD-TD Near-to-Far Field Transformation Technique . . . .	67
25	Geometry for Two-Dimensional Scattering Example: Square Conducting Cylinder Illuminated by a Plane Wave at Oblique Incidence ( $\phi = 45^\circ$ ). . . . .	69
26a	Comparison of MOM and FD-TD Results for Magnitude of Electric Currents on Surface of Cylinder, Oblique Incidence Case. . . . .	70
26b	Comparison of MOM and FD-TD Results for Phase of Electric Currents on Surface of Cylinder, Oblique Incidence Case . . . .	71
27a	Comparison of MOM and FD-TD Results for Near Electric Field Tangential to Contour $S_a$ for Oblique Incidence Case . . . . .	72

# LIST OF FIGURES (cont.)

<u>Figure</u>		<u>Page</u>
27b	Comparison of MOM and FD-TD Results for Phase of Near Electric Field Tangential to Contour $S_a$ for Oblique Incidence Case. . . . .	73
28a	Comparison of MOM and FD-TD Results for Near Magnetic Field Tangential to Contour $S_a$ for Oblique Incidence Case . . .	74
28b	Comparison of MOM and FD-TD Results for Phase of Near Magnetic Field Tangential to Contour $S_a$ for Oblique Incidence Case. . . . .	75
29	Equivalence of Computed Results for Radar Cross Section Obtained Using the MOM Surface Currents Approach and the Hybrid MOM Near-to-Far Field Transformation Technique . . . . .	77
30	Equivalence of Computed Results for Radar Cross Section Obtained Using the MOM Surface Currents Approach and the Hybrid MOM Near-to-Far Field Transformation Technique . . . . .	78

USER'S CODE FOR THE FINITE-DIFFERENCE TIME-DOMAIN METHOD

Air Force Contract No. F30602-80-C-0302

IITRI Project No. E6502

1 September 1980 - 31 August 1981

FINAL REPORT

1.0 INTRODUCTION

Electromagnetic penetration and scattering problems are difficult to treat with many analytical or numerical methods because of the inability of these methods to simply deal with the effects of structure materials, apertures, curvatures, corners, and internal contents. Usually, only relatively simple geometries are studied in an attempt to gain insight into the key interaction mechanisms and to allow an indirect estimate of the interaction for more complicated problems.

In earlier RADC Contracts F30602-77-C-0163 and F30602-79-C-0039, IITRI investigated the application of a new approach for the direct modeling of very complex electromagnetic interaction problems: the finite-difference, time-domain (FD-TD) solution of Maxwell's equations. The FD-TD method treats the illumination of a structure as an initial-value problem. At  $t = 0$ , a plane-wave source of frequency,  $f$ , is assumed to be turned on. The propagation of waves from this source is simulated by solving a finite-difference analog of the time-dependent Maxwell's equations on a lattice of cells, including the structure. Time-stepping is continued until the sinusoidal steady state is achieved at each cell. The field envelope, or maximum absolute value, during the final wave-cycle of time-stepping is observed to obtain the magnitude and phase of the steady-state field at any point.

This method has two key advantages relative to available modeling approaches. First, it is simple to implement for complicated metal/dielectric structures because arbitrary electrical parameters can be assigned to each lattice cell using a data card deck. Second, its computer memory and running time requirement is not prohibitive for many complex structures

of interest. In the RADC work, IITRI has shown the FD-TD method to be capable of accurately solving for more than one million unknown field components within a few minutes on an array-processing computer. Consistently, a  $\pm 1$ -dB accuracy relative to known analytical and experimental bench marks has been achieved for a variety of dielectric and metal geometries.

The objective of IITRI's previous RADC studies was to evaluate the suitability of the FD-TD method to determine the amount of electromagnetic coupling through an aperture into an enclosed conducting container and the interaction and coupling of the penetrating fields with internal electronics. Two specific container models were used for the evaluation. The first, a simple conducting cylinder with one open end. The other, the complex guidance section of a missile. Each of these two configurations was modeled to calculate the electromagnetic field coupled into the structure.

The ultimate aim of research in this area is two-fold. First, develop an accurate, easily-used, general code solving for either electromagnetic field penetration, scattering, or radiation for arbitrary metal/dielectric structures spanning up to 10 or more wavelengths in three dimensions with a spatial resolution better than 0.1 wavelength. Second, develop a more sophisticated intuitive understanding of basic wave interaction mechanisms in time domain, such as transient propagation through beyond-cutoff cavity interiors, field build-up at edges, convergence to the sinusoidal steady state, scattering, and radiation.

In order to more fully determine the usefulness of the FD-TD method, RADC thought that it is desirable to distribute this technique to as wide a range of users as possible so that it can be tested by actual implementation. However, the FD-TD computer programs previously developed by IITRI for RADC were research oriented rather than user oriented, i.e., they were written to apply to fairly specific types of interaction structures rather than completely general structures. Further, these FD-TD programs were optimized for a specific vector array processing computer, the Control Data

Cyber 203, in order to minimize the cost of purchased computer time. The Fortran used for these programs was specialized to benefit from the machine-specific features of the Cyber 203, and is not directly usable by common scalar-processing computers such as the Honeywell 6000 series, CDC 6600, CDC Cyber 76, or IBM 370 series.

The overall objectives of algorithm development in this case are to allow RADC to write a user-oriented program for the FD-TD technique. Such a program would ideally buffer the user from the complexities involved in specifying an interaction geometry in the form needed by the main program. Further, such a program would be suitable for arbitrary shaped bodies, material parameters, incident-wave angle of incidence and direction of polarization, and time dependence on the incident wave. Finally, such a computer program would be machine-independent, i.e., written in a standard language such as Fortran IV, so that implementation on a very wide variety of computers would be easily possible. However, the program would still be structured to make the best economy of computer resources such as memory storage and program execution time.

The goals of the present IITRI research effort for RADC include the development of specific algorithms of high importance to help provide a flexible, simple-to-use, and highly accurate user-oriented FD-TD computer program. IITRI has tested five key improvements in the FD-TD algorithm during this effort, and reports on these developments in this document. The following is a listing of these algorithm developments, including comments indicating the usefulness of each development.

1. Total-field/scattered-field lattice division.

This permits a very high computational dynamic range to accurately model fields within shadow zones or cavities. This further permits programming of variable angle of incidence and the second-order correct radiation condition, summarized below.



2. Variable angle of incidence.

For two-dimensional problems, this permits a single data card or Fortran statement to specify in a very accurate manner the angle of incidence of a plane wave illuminating a structure. For three-dimensional problems, both the angle of incidence and polarization could be specified. There is no requirement to rotate the geometry of the interacting structure in the FD-TD lattice.

3. Second-order accurate radiation condition.

This reduces the uncertainty of the final computed results by as much as ten-to-one. FD-TD computations using this radiation condition now have estimated field-magnitude uncertainties of better than  $\pm 2.5\%$  ( $\pm 0.2$  dB) versus previous uncertainties of  $\pm 10\%$  -  $\pm 15\%$  ( $\pm 1$  dB).

4. Magnitude and phase computation condition for the sinusoidal steady state

This permits determination of the magnitude and phase of FD-TD computed fields at any desired points for later use in computations involving scattering, radiation, or coupling to wires. This approach avoids any ambiguity due to either a possible DC offset of the fields or the repetitive nature of the sinusoidal waveform.

5. Near-to-far field transformation.

This permits the far scattered fields and radar cross section of arbitrary structures modeled by the FD-TD method to be easily and accurately determined. Observed accuracy of the radar cross section using this feature is in the order of  $\pm 1\%$  ( $\pm 0.09$  dB).

In addition to the five algorithm improvements tested by IITRI, this report will also summarize a FD-TD feature which has recently appeared in the literature that permits computation of the coupling of currents to thin wires and struts.

Section 2.0 of this report will provide a complete summary of the theory and basic algorithms of the FD-TD method, including the five new features tested by IITRI and the thin-wire coupling model. Sub-sections which contain discussion of these new features will be denoted by a double asterisk (\*\*) appearing before the headings. Section 3.0 of this report will provide examples of computed results which illustrate each of the key features of the FD-TD method examined to date. Again, examples of new features will be denoted by a double asterisk appearing before the appropriate heading. Appendix A provides a standard Fortran listing of a two-dimensional FD-TD computer program which illustrates the key features tested by IITRI during this research effort.

## 2.0 THEORY AND BASIC ALGORITHMS OF THE FD-TD METHOD

### 2.1 Ideas Behind the FD-TD Method

The FD-TD method is a direct solution of Maxwell's time-dependent curl equations. As shown in Figure 1, the goal is to model the propagation of an electromagnetic wave into a volume of space containing a dielectric or conducting structure. By time-stepping, i.e., repeatedly implementing a finite-difference analog of the curl equations at each cell of the corresponding space lattice, the incident wave is tracked as it first propagates to the structure and then interacts with it via surface-current excitation, diffusion, penetration, and diffraction. Wave-tracking is completed when the desired late-time or sinusoidal steady-state behavior is observed at each lattice cell. The rationale for this procedure is that it achieves simplification by analyzing the interaction of the wave-front with portions of the structure surface at a given instant in time, rather than attempting a simultaneous solution of the entire problem.

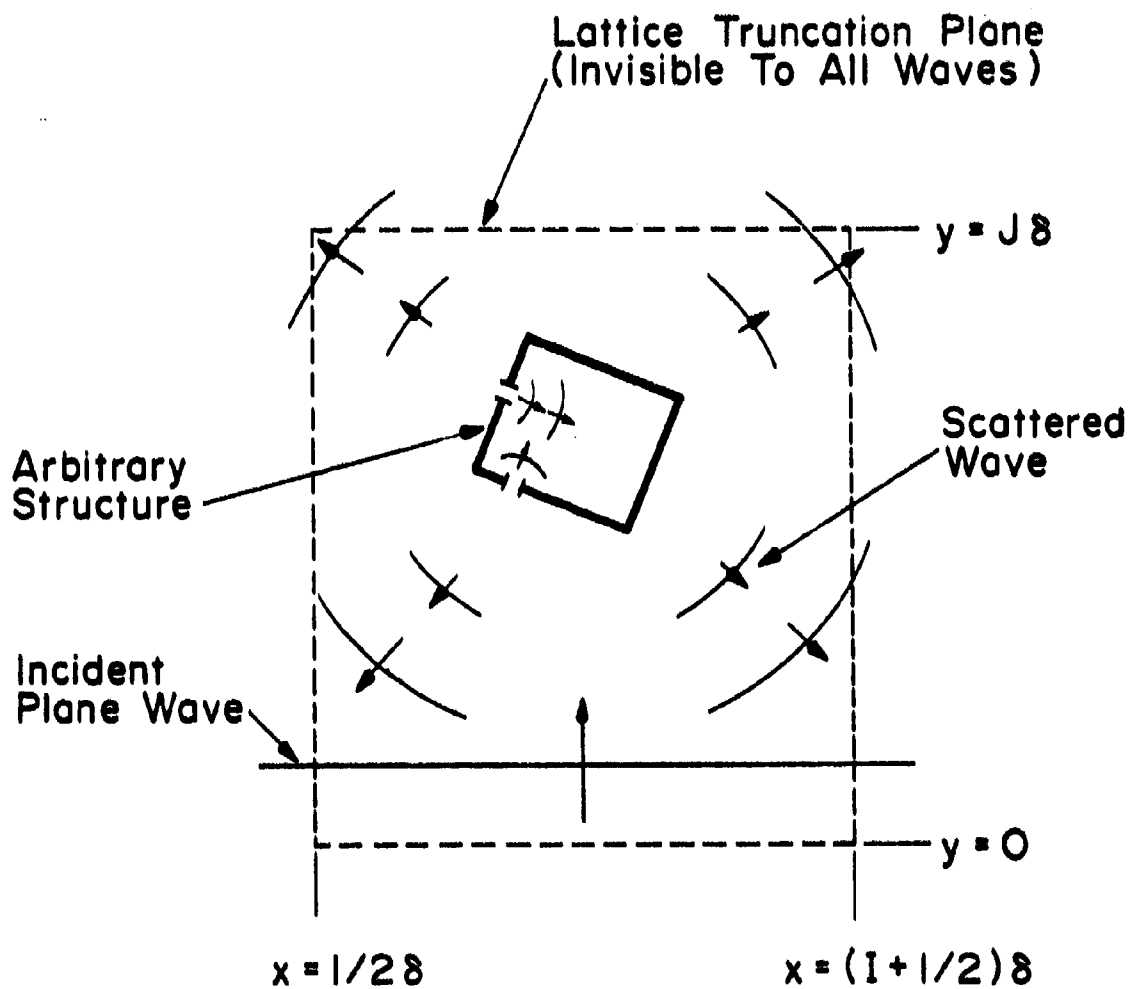


Figure 1. TIME-DOMAIN WAVE-TRACKING CONCEPT OF THE FD-TD METHOD

Time-stepping for the FD-TD method is accomplished by an explicit finite-difference procedure due to Yee [1]. For a cubic-cell space lattice, this procedure involves positioning the components of  $\vec{E}$  and  $\vec{H}$  about a unit cell of the lattice, as shown in Figure 2, and evaluating  $\vec{E}$  and  $\vec{H}$  at alternate half-time steps. In this manner, centered difference expressions can be used for both the space and time derivatives to attain second-order accuracy in the space and time increments without requiring simultaneous equations to compute the fields at the latest time step.

The finite-difference formulation of the FD-TD method allows the straightforward modeling of the surfaces and interiors of arbitrary dielectric or conducting structures. The structure of interest is mapped into the space lattice by first choosing the space increment and then employing a data card deck to assign values of permittivity and conductivity to each component of  $\vec{E}$ . No special handling of electromagnetic boundary conditions at media interfaces is required because the curl equations generate these conditions in a natural way by themselves. Therefore, the basic computer program need not be modified to change from structure to structure. In this manner, inhomogeneities or fine details of the structure can be modeled with a maximum resolution of one unit cell; thin surfaces can be modeled as stepped-edge sheets. Figure 3 shows an arbitrary three-dimensional scatterer embedded in a FD-TD lattice.

The explicit formulation of the FD-TD method is particularly suited for programming with minimum storage and execution time using recently developed array-processing computers. First, the required computer storage and running time increases only linearly with  $N$ , the total number of unknown field components. Computer techniques (such as the method-of-moments) which require the solution of simultaneous equations usually have a storage requirement proportional to  $N^2$  and a running time proportional to  $N^2$ - $N^3$  [2]. Second, since all FD-TD operations are explicit and can be performed in parallel, rapid array-processing techniques can be readily applied. As will be demonstrated later, these can be employed to solve for more than  $10^6$  field components in a single FD-TD problem, as opposed to a maximum of about  $10^3$  field components for conventional approaches using simultaneous-equation solutions [2].

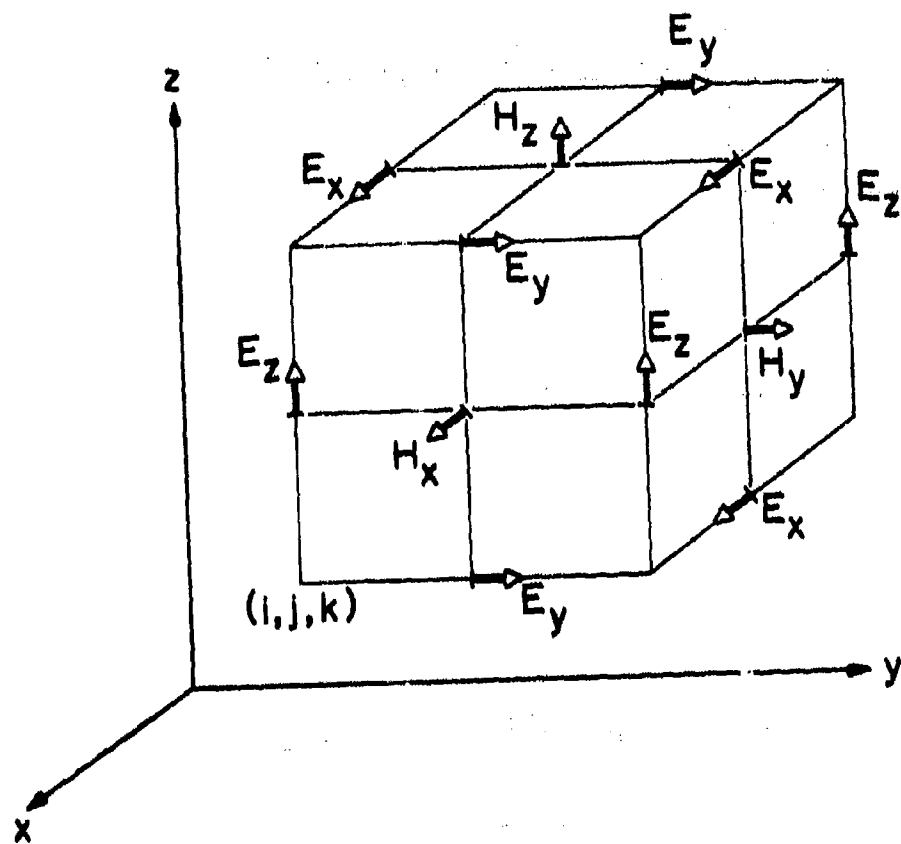


Figure 2. POSITIONS OF THE FIELD COMPONENTS ABOUT A UNIT CELL OF THE YEE LATTICE [1]

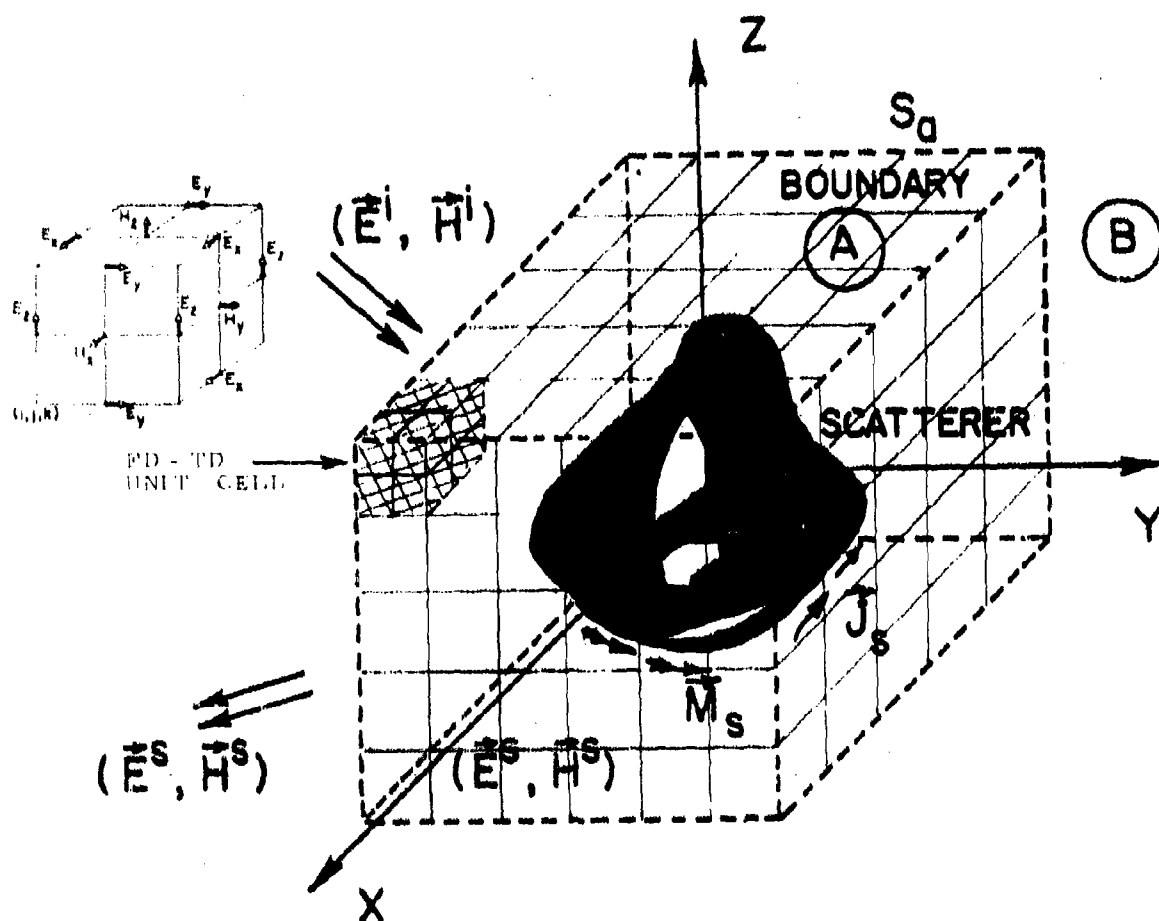


Figure 3. ARBITRARY THREE-DIMENSIONAL SCATTERER EMBEDDED IN A FD-TD LATTICE

Yee applied the FD-ID method to compute the waveforms of TM and TE pulses scattered from infinitely long, rectangular cross section, conducting cylinders [1]. Other workers investigated electromagnetic-pulse (EMP) interactions in time-varying inhomogeneous media [3]; with metallic bodies of revolution [4]; with detailed models of aircraft [5], [6]; with lossy dielectric structures [7]; and with thin struts and wires [8]. Four distinct problems emerged in the process of adapting the FD-TD method to model realistic situations:

1) Lattice Truncation Conditions. The field components at the lattice truncation planes cannot be determined directly from the Maxwell's-equations analog and must be computed using an auxiliary truncation condition. However, care must be exercised because this condition must not cause excessive spurious reflection of waves scattered outward by the structure modeled. The goal is to formulate truncation planes as close as possible to the structure (to minimize computer storage), and yet achieve virtual invisibility of these planes to all possible waves within the lattice.

2) Incident Plane-Wave Source Condition. The simulation of either a plane-wave pulse or single-frequency plane wave at arbitrary angles of incidence should not take excessive storage nor cause spurious wave reflections. The former would occur if the incident wave is programmed as an initial condition; the latter would occur if the incident wave is programmed as a fixed field excitation along a single lattice plane.

3) Sinusoidal Steady-State Information. Such data can be obtained either by a) directly programming a single-frequency incident plane wave or b) performing a separate Fourier transformation step on the pulse waveform response. Both methods require time-stepping to a maximum time equal to several wave periods at the desired frequency. The second method has two additional requirements. First, a short-rise-time pulse suffers from accumulating waveform error due to overshoot and ringing as it propagates through the space lattice. This leads to a numerical noise component which should be filtered before Fourier transformation. Second, Fourier trans-

formation of many lattice-cell field-versus-time waveforms (each probably extending over many hundreds of time steps) would significantly add to the total requirements for computer storage and execution time.

4) Total-Field versus Scattered-Field Formulation. A choice exists in whether to finite-difference only the scattered field instead of the total field (at each lattice cell). The scattered-field approach may lead to a relatively superior lattice truncation condition [4]. However, the total-field approach is more useful in determining the fields penetrating structures having shielding properties, or the fields in the shadow regions of scatterers, where the total field can diminish to levels far below the incident. Scattered-field codes have traditionally run into numerical "noise" problems for such cases since they achieve interior or shadow-zone field reduction by the subtraction of nearly equal scattered and incident field quantities. Computed shielding or shadowing of more than 30 dB may be difficult to achieve in this manner because of a residual "noise" floor inherent in this subtraction process. A total-field approach does not suffer from the subtraction-noise problem and hence is suitable for computing field penetration within shielded structures or into shadow zones.

Previous work by IITRI described initial efforts to solve the first three problems above for the case of a total-field FD-TD program employing a cubic-unit-cell space lattice [9] - [13]. Simple truncation conditions were developed for two and three-dimensional lattices that reduced the reflection coefficient of closely positioned truncation planes to the order of 0.1 for waves of arbitrary incidence. A plane-wave source condition was described that allowed generation of an arbitrary pulsed or sinusoidal wave (at a fixed angle of incidence) without requiring any additional storage and without causing spurious wave reflections. Finally, it was shown that sinusoidal steady-state data could be computed using the FD-TD method by directly programming a single-frequency incident plane wave and time-stepping to the steady-state over several periods of the incident wave. Observed accuracy was  $\pm 1$  dB at points of electric-field maxima, and  $\pm 1$  lattice



cell in locating electric-field maxima and minima, when the lattice-cell size was chosen to be less than  $0.05 \lambda$ , as discussed in detail in [12] and [13].

The following sub-sections will provide a full review of the latest formulation of the FD-TD method, including the features developed during the current research effort as well as the thin-wire coupling model. These new developments will be indicated by a double-asterisk (\*\*) appearing before the sub-section heading.

## 2.2 Computational Details for a Uniform, Cubic Lattice

### 2.2.1 Basic System of Equations

Using the MKS system of units, and assuming that the material parameters,  $\mu$ ,  $\epsilon$  and  $\sigma$  are independent of time, the following system of scalar equations is equivalent to Maxwell's equations in the rectangular coordinate system  $(x, y, z)$ :

$$\frac{\partial H_x}{\partial t} = \frac{1}{\mu} \left( \frac{\partial E_y}{\partial z} - \frac{\partial E_z}{\partial y} \right) \quad (1a)$$

$$\frac{\partial H_y}{\partial t} = \frac{1}{\mu} \left( \frac{\partial E_z}{\partial x} - \frac{\partial E_x}{\partial z} \right) \quad (1b)$$

$$\frac{\partial H_z}{\partial t} = \frac{1}{\mu} \left( \frac{\partial E_x}{\partial y} - \frac{\partial E_y}{\partial x} \right) \quad (1c)$$

$$\frac{\partial E_x}{\partial t} = \frac{1}{\epsilon} \left( \frac{\partial H_z}{\partial y} - \frac{\partial H_y}{\partial z} - \sigma E_x \right) \quad (1d)$$

$$\frac{\partial E_y}{\partial t} = \frac{1}{\epsilon} \left( \frac{\partial H_x}{\partial z} - \frac{\partial H_z}{\partial x} - \sigma E_y \right) \quad (1e)$$

$$\frac{\partial E_z}{\partial t} = \frac{1}{\epsilon} \left( \frac{\partial H_y}{\partial x} - \frac{\partial H_x}{\partial y} - \sigma E_z \right) \quad (1f)$$

Yee [1] originally introduced a set of finite-difference equations for the system of Equations (1a) - (1f). Following Yee's notation, we denote a space point in a cubic lattice as

$$(i,j,k) = (i\delta, j\delta, k\delta) \quad (2)$$

and any function of space and time as

$$F^n(i,j,k) = F(i\delta, j\delta, k\delta, n\delta t), \quad (3)$$

where  $\delta = \delta x = \delta y = \delta z$  is the space increment,  $\delta t$  is the time increment, and  $i, j, k$ , and  $n$  are integers. Yee used centered finite-difference expressions for the space and time derivatives that are both simply programmed and second-order accurate in  $\delta$  and in  $\delta t$ , respectively:

$$\frac{\partial F^n(i,j,k)}{\partial x} = \frac{F^n(i+\frac{1}{2},j,k) - F^n(i-\frac{1}{2},j,k)}{\delta} + O(\delta^2) \quad (4)$$

$$\frac{\partial F^n(i,j,k)}{\partial t} = \frac{F^{n+\frac{1}{2}}(i,j,k) - F^{n-\frac{1}{2}}(i,j,k)}{\delta t} + O(\delta t^2) \quad (5)$$

To achieve the accuracy of Equation (4), and to realize all of the space derivatives of Equations (1a) - (1f), Yee positioned the components of  $\vec{E}$  and  $\vec{H}$  about a unit cell of the lattice as shown in Figure 2. To achieve the accuracy of Equation (5), he evaluated  $\vec{E}$  and  $\vec{H}$  at alternate half time steps.

Many electromagnetic interaction problems involve nonpermeable media and can be approached using a fixed time step and space increment. For such problems, the quantity  $\delta t / \mu(i,j,k)\delta$  is constant for all  $(i,j,k)$  of the lattice, and the Yee system of equations can be simplified to reduce computer time in the following manner. We define the constants:

$$R = \delta t / 2\epsilon_0 \quad (6a)$$

$$R_a = \delta t^2 / (\delta^2 \mu_0 \epsilon_0) \quad (6b)$$

$$R_b = \delta^+ / \mu_0 \delta \quad (6c)$$

$$C_a(m) = \frac{1 - R\sigma(m)/\epsilon_r(m)}{1 + R\sigma(m)/\epsilon_r(m)} \quad (6d)$$

$$C_b(m) = \frac{R_a}{\epsilon_r(m) + R\sigma(m)} \quad (6e)$$

where  $m$  is an integer denoting a particular dielectric or conducting medium in the space to be modeled. We also define the proportional electric-field vector

$$\vec{E} = R_b \vec{E}. \quad (7)$$

Using the definitions of Equations (6a) - (6e) and (7), we reformulate Yee's finite-difference system for the  $\vec{H}$  time-stepping equations as:

$$\begin{aligned} H_x^{n+1/2}(i, j+1/2, k+1/2) &= H_x^{n-1/2}(i, j+1/2, k+1/2) + \tilde{E}_y^n(i, j+1/2, k+1) - \tilde{E}_y^n(i, j+1/2, k) \\ &\quad + \tilde{E}_z^n(i, j, k+1/2) - \tilde{E}_z^n(i, j+1, k+1/2) \end{aligned} \quad (8a)$$

$$\begin{aligned} H_y^{n+1/2}(i+1/2, j, k+1/2) &= H_y^{n-1/2}(i+1/2, j, k+1/2) + \tilde{E}_z^n(i+1, j, k+1/2) - \tilde{E}_z^n(i, j, k+1/2) \\ &\quad + \tilde{E}_x^n(i+1/2, j, k) - \tilde{E}_x^n(i+1/2, j, k+1) \end{aligned} \quad (8b)$$

$$\begin{aligned}
H_z^{n+1/2}(i+1/2, j+1/2, k) &= H_z^{n-1/2}(i+1/2, j+1/2, k) + \tilde{E}_x^n(i+1/2, j+1, k) - \tilde{E}_x^n(i+1/2, j, k) \\
&\quad + \tilde{E}_y^n(i, j+1/2, k) - \tilde{E}_y^n(i+1, j+1/2, k)
\end{aligned} \tag{8c}$$

Assuming  $m = \text{MEDIA}(i, j, k)$  denotes the type of medium at an electric field component location,  $E_{x,y,z}(i, j, k)$ , the  $\vec{E}$  time-stepping equations are:

$$\begin{aligned}
\tilde{E}_x^{n+1}(i+1/2, j, k) &= C_a(m) \tilde{E}_x^n(i+1/2, j, k) + C_b(m) [H_z^{n+1/2}(i+1/2, j+1/2, k) - H_z^{n+1/2}(i+1/2, j-1/2, k) \\
&\quad + H_y^{n+1/2}(i+1/2, j, k-1/2) - H_y^{n+1/2}(i+1/2, j, k+1/2)]
\end{aligned} \tag{8d}$$

$$\begin{aligned}
\tilde{E}_y^{n+1}(i, j+1/2, k) &= C_a(m) \tilde{E}_y^n(i, j+1/2, k) + C_b(m) [H_x^{n+1/2}(i, j+1/2, k+1/2) - H_x^{n+1/2}(i, j+1/2, k-1/2) \\
&\quad + H_z^{n+1/2}(i-1/2, j+1/2, k) - H_z^{n+1/2}(i+1/2, j+1/2, k)]
\end{aligned} \tag{8e}$$

$$\begin{aligned}
\tilde{E}_z^{n+1}(i, j, k+1/2) &= C_a(m) \tilde{E}_z^n(i, j, k+1/2) + C_b(m) [H_y^{n+1/2}(i+1/2, j, k+1/2) - H_y^{n+1/2}(i-1/2, j, k+1/2) \\
&\quad + H_x^{n+1/2}(i, j-1/2, k+1/2) - H_x^{n+1/2}(i, j+1/2, k+1/2)]
\end{aligned} \tag{8f}$$

This reformulation eliminates the three multiplications needed by Yee to compute  $H_x$ ,  $H_y$ , and  $H_z$ . Further, it eliminates the need for computer storage of separate  $\epsilon$  and  $\sigma$  arrays. Now, only a MEDIA array which specifies the type-integer of the dielectric or conducting medium at the location of each electric field component in the lattice need be stored. In addition, the

$\epsilon_r$  and  $\sigma$  of each medium can now be changed without having to re-punch a large data card deck, if the basic structure geometry is unchanged. Such a change involves only the recalculation of the few values of  $C_a(m)$  and  $C_b(m)$ .

With the system of Equations (8a) - (8f), the new value of a field vector component at any lattice point depends only on its previous value and on the previous values of the components of the other field vector at adjacent points. Therefore, at any given time step, the computation of a field vector may proceed either one point at a time, or, with a parallel processing computer, at many points at a time.

The choice of  $\delta$  and  $\delta t$  is motivated by the reasons of accuracy and algorithm stability, respectively. To insure the accuracy of the computed spatial derivatives of the electromagnetic fields,  $\delta$  must be small compared to a wavelength (usually  $\leq \lambda/10$ ). Further, to insure that the cubic lattice approximation to the surfaces of the structure modeled is not too coarse,  $\delta$  must be small compared to the overall dimensions of the structure.

To insure the stability of the time-stepping algorithm of Equations (8a) - (8f),  $\delta t$  is chosen to satisfy the inequality

$$\delta t \leq \left( \frac{1}{\delta x^2} + \frac{1}{\delta y^2} + \frac{1}{\delta z^2} \right)^{-\frac{1}{2}} c_{\max}^{-1} = \frac{\delta}{c_{\max} \sqrt{3}} \quad (\text{for a cubic lattice}) \quad (9)$$

where  $c_{\max}$  is the maximum wave phase velocity within the model [9]. The corresponding stability criterion set forth by Yee in Equations (7) and (8) of his paper [1] is incorrect.

#### **\*\*2.2.2 Lattice Regions and Plane Wave Source Condition [14]-[16]**

As shown in Figure 4a, the latest formulation of the FD-TD lattice involves the division of the computation space into two distinct regions, separated by a rectangular surface which serves to connect fields in each region. In two dimensions, the surface has four faces; in three dimensions, the surface has six faces.

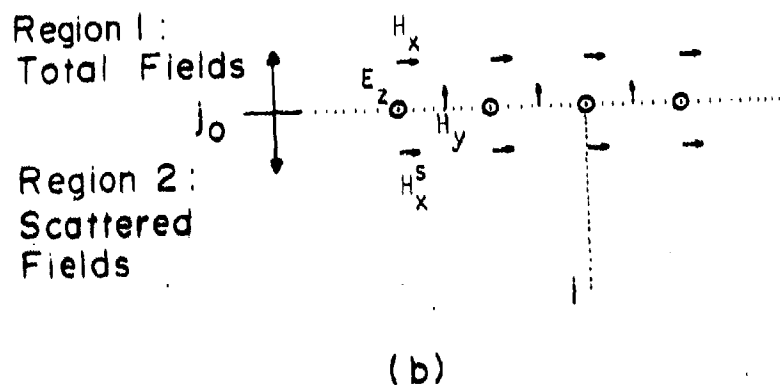
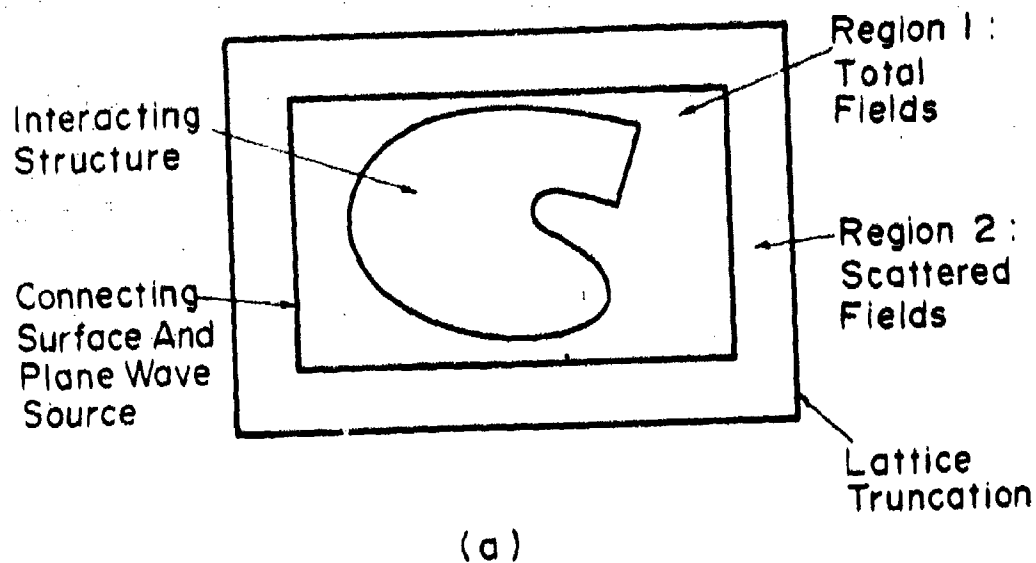


Figure 4. DIVISION OF FD-TD LATTICE INTO TOTAL-FIELD AND SCATTERED-FIELD REGIONS. (a) Lattice division; (b) Field component geometry at connecting plane  $y = j_0 \delta$

Region 1 of the FD-TD lattice is denoted as the total-field region. Here, it is assumed that all computed field quantities are comprised of the sum of the incident wave and the scattered field. The interacting structure of interest is embedded within this region.

Region 2 of the FD-TD lattice is denoted as the scattered-field region. Here, it is assumed that all computed field quantities are comprised only of the scattered field. The outer lattice planes bounding Region 2, called the lattice truncation planes, serve to implement the free-space radiation condition, discussed in the next subsection.

The rectangle faces comprising the boundary between Regions 1 and 2 contain E and H field components which, according to the system of equations (8a) - (8f), require the formulation of various field-component differences across the boundary planes for proceeding one time step. Typical FD-TD computations at these boundary points are as follows, using the spatial coordinates shown in Figure 4b.

$$\tilde{E}_z^{n+1}(i, j_0) = \tilde{E}_z^{n+1}(i, j_0)|_{\text{Eqn. (8f)}} + C_b(m)H_x^{i, n+1/2}(i, j_0 - 1/2) \quad (10a)$$

$$H_x^{n+1/2}(i, j_0 - 1/2) = H_x^{n+1/2}(i, j_0 - 1/2)|_{\text{Eqn. (8a)}} + \tilde{E}_z^{i, n}(i, j_0) \quad (10b)$$

Here,  $\tilde{E}_z^{n+1}(i, j_0)$  is the usual FD-TD value of the total  $E_z$  component evaluated at point  $(i, j_0)$  and time step  $n+1$ . Similarly,  $H_x^{n+1/2}(i, j_0 - 1/2)$  is the usual FD-TD value of the scattered  $H_x^s$  component evaluated at point  $(i, j_0 - 1/2)$  and time step  $n+1/2$ .  $C_b(m)$  denotes a proportionality factor defined in Equation (6e). The superscript "i" denotes the known incident field component value. These computations assure consistency of the subtraction operations of field components across the Region 1/Region 2 boundary. In effect, total-field quantities are always subtracted from similar total-field quantities; and scattered-field quantities are always subtracted from

similar scattered-field quantities. This enforcement of consistency serves to precisely connect the total-field and scattered-field regions. Further, the inclusion of arbitrary values of  $\tilde{E}^i$  and  $H^i$  in the consistency relations permits the precise specification of the desired plane wave of arbitrary angle of incidence and arbitrary polarization.

There are a number of key advantages to this methodology: (a) The high-dynamic-range, total-field formalism is retained for the entirety of the interacting structure, permitting accurate computations of low-level fields penetrating into cavities through apertures, and in the shadow regions of scatterers. (b) The scattered-field formalism is retained for the lattice truncation region, permitting a very accurate simulation of the radiation condition. (c) The incident wave contribution need be computed or stored only for the field components at the rectangular surface connecting Regions 1 and 2. This results in much less computation or storage than if the incident field were to be computed at all points within the interacting structure to implement a pure scattered-field formalism. (d) The scattered near field in Region 2 can be easily integrated to derive the far-field scattering and radar cross section, as discussed later.

### **\*\*2.2.3 Lattice Truncation Conditions**

A basic consideration with the FD-TD approach to solve electromagnetic field problems is that most such problems are usually considered to be "open" problems where the domain of the computed field is ideally unbounded. Clearly, no computer can store an unlimited amount of data, and the field computation zone must be limited. The computation zone must be large enough to enclose the structure of interest, and a suitable boundary condition on the outer perimeter of the computation zone must be used to simulate the extension of the computation zone to infinity. Outer boundary conditions of this type have been called either radiation conditions, absorbing boundary conditions, or lattice truncation conditions by various recent workers in this area.



Let us now consider this problem in more detail. Inspection of Equations (8a) - (8f) indicates that the values of field components at lattice truncation planes cannot be determined from the system of finite-difference equations because of the centered nature of the spatial derivatives. Therefore, these values must be computed using an auxiliary truncation condition. However, care must be taken because this condition must not cause the spurious back-reflection of outgoing scattered waves (as observed by Yee), and must not cause numerical instability. The goal of formulating the truncation condition is to make the lattice truncation planes invisible to all possible waves propagating within the lattice, as shown in Figure 1.

A desirable truncation condition relates in a simple way the values of the field components at the truncation planes to field component values at points one or more  $\delta$  within the lattice. We now review several possible approaches which have been recently published.

1. First-order approximations. In three dimensions, an outgoing scattered-wave field component,  $F^S$  (either an electric or magnetic field) has a  $(r, \theta, \phi)$  variation of the type [17].

$$F^S = F_0 e^{j(\omega t - k_0 r)} \left( \frac{A(\theta, \phi)}{r} + \frac{B(\theta, \phi)}{r^2} + \dots \right) \quad (11)$$

Here, the bracketed infinite series represents in effect a multipole expansion of the scattered field, where  $A, B, \dots$  are initially unknown functions of angular position.

First-order simulations of the outer lattice boundary condition approximate the  $A(\theta, \phi)/r$  dependence only. These approximations include those of: a) Taylor et al [3], using a radial field extrapolation method; b) Taflov and Brodwin [9], [12], using simulation of near-field outgoing waves with propagation delay, a field averaging process, and the possible use of electric or magnetic loss in the scattered-field zone; and c) Merewether [4] and Kunz and Lee [6] simulating the radiation condition at large distances from the center of the scatterer.

2. Second and higher-order approximations. These simulate the  $B(0,\phi)/r^2$  and higher-order  $r$ -dependent behavior of  $F^S$  in addition to the  $A(0,\phi)/r$  term. These approximations include those of: a) Engquist and Majda [18]; and b) Kriegsmann and Morawetz [19]. In general, these approaches involve the construction of mixed radial and time-derivative operators,  $D_i$  on  $F^S$ , which result in  $D_i(F^S) = O(r^{-i-1})$  so that arbitrary precision at any  $r$  can be obtained by increasing the order,  $i$ , of  $D_i$  (here  $O$  represents the order of a function).

A second-order approximation of this type at truncation plane  $x = 0$  is given by [18]

$$\left( \frac{1}{c} \frac{\partial^2 F^S}{\partial x \partial t} - \frac{1}{c^2} \frac{\partial^2 F^S}{\partial t^2} + \frac{1}{2} \left( \frac{\partial^2 F^S}{\partial y^2} + \frac{\partial^2 F^S}{\partial z^2} \right) \right)_{x=0} = 0 + O\left(\frac{1}{r^3}\right) \quad (12)$$

for the radiation condition at the lattice truncation plane  $x = 0$ . (Here  $c$  is the free-space phase velocity). A typical FD-TD computation realizing this radiation condition is given by [16]:

$$\begin{aligned} \tilde{E}_z^{n+1}(0, j, k+\frac{1}{2}) &= -\tilde{E}_z^{n-1}(1, j, k+\frac{1}{2}) \\ &+ \frac{c\delta t - \delta}{c\delta t + \delta} \left[ \tilde{E}_z^{n+1}(1, j, k+\frac{1}{2}) + \tilde{E}_z^{n-1}(0, j, k+\frac{1}{2}) \right] \\ &+ \frac{2\delta}{c\delta t + \delta} \left[ \tilde{E}_z^n(0, j, k+\frac{1}{2}) + \tilde{E}_z^n(1, j, k+\frac{1}{2}) \right] \\ &+ \frac{(c\delta t)^2}{2\delta(c\delta t + \delta)} \left[ \begin{aligned} &\tilde{E}_z^n(0, j+1, k+\frac{1}{2}) - 2\tilde{E}_z^n(0, j, k+\frac{1}{2}) + \tilde{E}_z^n(0, j-1, k+\frac{1}{2}) \\ &+ \tilde{E}_z^n(1, j+1, k+\frac{1}{2}) - 2\tilde{E}_z^n(1, j, k+\frac{1}{2}) + \tilde{E}_z^n(1, j-1, k+\frac{1}{2}) \\ &+ \tilde{E}_z^n(0, j, k+\frac{3}{2}) - 2\tilde{E}_z^n(0, j, k+\frac{1}{2}) + \tilde{E}_z^n(0, j, k-\frac{1}{2}) \\ &+ \tilde{E}_z^n(1, j, k+\frac{3}{2}) - 2\tilde{E}_z^n(1, j, k+\frac{1}{2}) + \tilde{E}_z^n(1, j, k-\frac{1}{2}) \end{aligned} \right] \end{aligned} \quad (13)$$

In Equation (13),  $\tilde{E}_z^{n+1}(0, j, k + \frac{1}{2})$  is the desired truncation-plane value of  $\tilde{E}_z$  at point  $(0, j, k + \frac{1}{2})$ ;  $\delta$  is the lattice cell size; and  $\delta t$  is the time step. An analogous condition can be written for  $E_y$  at  $x = 0$ , as well as for  $E_z$  and  $E_y$  at truncation plane  $x_{\max}$ ;  $E_z$  and  $E_x$  at truncation planes  $y = 0$  and  $y_{\max}$ ; and  $E_x$  and  $E_y$  at truncation planes  $z = 0$  and  $z_{\max}$  (in three-dimensional problems).

#### \*\*2.2.4 Sinusoidal Steady-State Magnitude and Phase Information

Such data can be obtained either by (a) directly programming a single-frequency incident plane wave, or (b) performing a separate Fourier transformation step on the pulse waveform response. Both methods require time-stepping to a maximum time equal to several wave periods at the desired frequency. The second method has two additional requirements. First, a short-rise-time pulse suffers from accumulating waveform error due to overshoot and ringing as it propagates through the space lattice. This leads to a numerical noise component which must be filtered before Fourier transformation. Second, Fourier transformation of many lattice-cell field-versus-time waveforms would significantly add to the total requirements for computer storage and execution time [3,4].

Recent IITRI work has shown that very accurate magnitude and phase information for sinusoidal steady-state FD-TD problems can be obtained by method (a) above and observing the peak positive and negative-going excursions of the fields over a complete cycle of the incident wave (after having time-stepped through 2-5 cycles of the transient period following the beginning of time stepping). For certain two and three-dimensional scattering problems, a dc offset of particular computed field components can be possible. This leads to the following requirements to obtain correct magnitude and phase data:

1. The peak-to-peak value of the sinusoidal response at any point must be observed to eliminate the effects of any dc offset upon the computation of the phasor magnitude.
2. The zero-crossing of the field waveform may not be useful in determining relative phase. Rather, it may be necessary to locate the zero-derivative points of the waveform for this purpose.

The following is an algorithm to locate the zero-derivative points of a field-vs-time waveform computed using the FD-TD method. This particular algorithm has an uncertainty of one time step or less, and operates by noting where the sign of the waveform time derivative changes from positive to negative, or negative to positive.

For ease of understanding the algorithm and relating it to the Fortran program of Appendix A, the algorithm is given here in the form of a simplified Fortran program. The symbols used here are defined as follows:

- NCYCS = the number of complete cycles of the sinusoidal incident wave that the FD-TD program is time-stepped;
- FREQ = the frequency of the sinusoidal incident wave (in Hz);
- DT = the time step of the FD-TD program (in seconds);
- NMIN = the number of time steps spanning one complete cycle of the sinusoidal incident wave;
- NMAX = the total number of time steps that the FD-TD program is time-stepped;
- NMINA = the number of time steps spanning one-half cycle of the sinusoidal incident wave;
- N = absolute time-step number (from beginning of time-stepping), ranging from 1 to NMAX;
- NA = number of time steps since the start of the present full-wave-cycle observation period for zero-derivative points, ranging from 0 to NMIN-1;
- F = field component (either  $E_x$ ,  $E_y$ ,  $E_z$ ,  $H_x$ ,  $H_y$ , or  $H_z$ );
- DF, DFNU = time derivatives of the F waveform;
- ENF = stored value of F, taken at the time of each zero-derivative event of F;
- IPHF = stored value of NA, taken at the time of a zero-derivative event of F coupled with a change of sign of the F derivative from positive to negative.

The algorithm is as follows:

NMIN = 1.0/FREQ/D1	
NMID = NMIN	
NMAX = NCYCS * NMIN	
NMINA = FLOAT(NMIN)/2.0	} Define constants
NMIDA = NMINA	
NMAXA = NCYCS * 2 * NMINA	
DO 21 N=1, NMAX	
FNMOD = FLOAT(N)/FLOAT(NMID)	
NA = N - IFIX(FNMOD)*NMID	
DO zzz J = jlimits	} Test field component F(i,j) for change of sign of time derivative
DO zzz I = ilimits	
STORE = F(I,J)	
F(I,J) = new F computed using Eqns.(8a-8f)	
DFNU = F(I,J) - STORE	
IF(DFNU*DF(I,J).GT.0.0) GO TO xxx	
ENF(I,J) = F(I,J)	
IF (DFNU.LT.0.0) IPHF(I,J)= NA	
xxx DF(I,J) = DFNU	
zzz CONTINUE	
DO 12 K=NMINA,NMAXA,NMIDA	} Test for half-cycle intervals of time- stepping
IF(N.EQ.K) GO TO 13	
12 CONTINUE	
GO TO 20	
13 Fortran statements which first print out the ENF array and then reset the ENF array to zero.	
20 DO 512 K=NMIN,NMAX,NMID	} Test for full-cycle intervals of time- stepping
IF (N.EQ.K) GO TO 513	
512 CONTINUE	
GO TO 520	
513 Fortran statements which first print out the IPHF array, and then reset the IPHF array to zero.	

520 CONTINUE

21 CONTINUE

STOP

END

— End of main time-  
stepping loop

Every time step, the above algorithm tests the desired field waveform,  $F$ , for a change of sign of the time derivative. If a sign change is detected, the latest computed value of  $F$  is stored in the array ENF. Note that this value can be either positive or negative. If, further, the new sign of the time derivative is negative, indicating that a "peak" of the  $F$  waveform has just occurred, the time-step number, NA, is stored in the array IPHF.

The above algorithm also tests to determine when half-cycle and full-cycle intervals of time stepping have passed. Each half-cycle, the stored values of ENF are first printed out and then reset to zero. Each full-cycle, the stored values of IPHF are first printed out and then reset to zero. Therefore, the desired zero-to-peak value of  $F$  is determined by subtracting the last printed value of ENF from the immediately-preceding printed value of ENF, taking the absolute value, and then dividing by two. Also, the desired relative phase of  $F$  can be obtained by subtracting values of IPHF (as given in the last printout of IPHF) from some fixed reference value at a specified point. This methodology avoids any ambiguity due to either a possible DC offset of the  $F$  waveform or the repetitive nature of the  $F$  waveform.

#### **\*\*2.2.5 Far-Field Scattering Information via the Near-to-Far Field Transformation**

In principle, the electromagnetic scattering by an arbitrary conducting body can be determined by solving an integral equation for the induced electric currents on the surface of the body. Then, the induced currents can be integrated to calculate the near or the far fields. However, the body surface may have a complex shape or may be loaded with dielectrics in some way as to make implementation of the needed integral equation and surface integrals very difficult, and in fact, a unique problem for each scatterer. A useful alternative would be to obtain the scattered-field

information from off-surface, near field data, rather than surface-current data. Here, the near field information could be computed using the FD-TD method, which can easily account for the complexities introduced by the object's shape and composition. Further, the near-field data could be integrated along arbitrary, planar, virtual surfaces which completely surround the object of interest. In this manner, accounting of the data would be simple and would be independent of the precise shape of the object which resides within the integration surfaces. Fortunately, this near-field to far-field transformation can be shown to be feasible by using powerful electromagnetic equivalence relations.

Figure 5 demonstrates a procedure to implement the electromagnetic equivalence needed to obtain far-field data from FD-TD-computed near-field information at an arbitrary, closed, virtual boundary,  $S_a$ , fully enclosing a scatterer.  $S_a$  separates Region A (FD-TD computation zone) from Region B (exterior scattered-field zone).  $S_a$  is optimally a rectangular surface which conforms with distinct planes of the FD-TD lattice located in the scattered-field region (Region 2) of Figure 4.

To apply the hybrid FD-TD method, the tangential components of the scattered fields,  $\vec{E}^S$  and  $\vec{H}^S$ , are first obtained at  $S_a$  using FD-TD. Then, as indicated in Figure 5b, an equivalent problem is set up external to  $S_a$  which is completely valid for Region B. The new excitation data are  $\vec{J}_{seq}$  and  $\vec{M}_{seq}$ , the equivalent surface electric and magnetic currents, respectively, on  $S_a$  which are obtained according to [20]:

$$\vec{J}_{seq}(\vec{r}) = \hat{n} \times \vec{H}^S(\vec{r}) \quad (14a)$$

$$\vec{M}_{seq}(\vec{r}) = -\hat{n} \times \vec{E}^S(\vec{r}) \quad (14b)$$

where  $\hat{n}$  is the outward unit normal vector at the surface  $S_a$ .

The equivalent surface currents on  $S_a$  produce the same scattered field ( $\vec{E}^S$ ,  $\vec{H}^S$ ) external to  $S_a$  as in the original problem. Region A is now made empty with zero fields and no sources, and also forced to have the same medium characteristics as Region B.

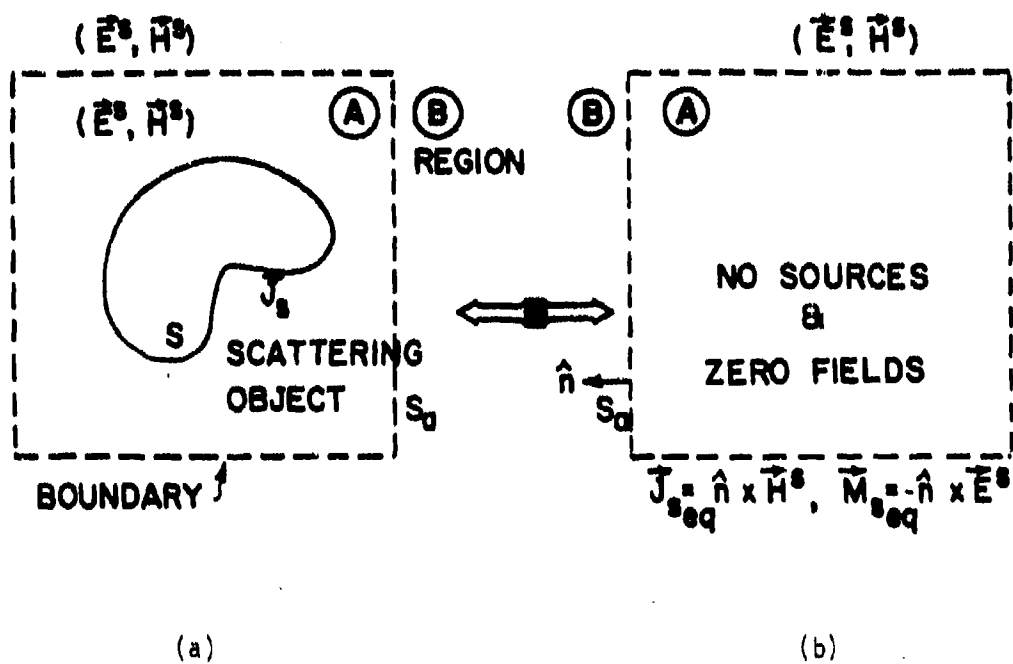


Figure 5. NEAR-TO-FAR FIELD TRANSFORMATION GEOMETRY  
 (a) Original problem; (b) Equivalent problem external to the virtual surface,  $S_a$



The scattered far fields are thus given by the transform of the equivalent currents of Eqns. (14) over the free-space Green's function [17]. If  $(\mu_0, \epsilon_0, \sigma_0)$  are the Region-B medium characteristics, and if we define the relation  $s = j\omega$ , we have the following general scattered-field expressions [17] in three dimensions for  $\vec{r} > \vec{r}_a$ :

$$\vec{E}^S(\vec{r}, s) = -\frac{s}{\gamma_0^2} \{ \nabla[\nabla \cdot \vec{A}_m(\vec{r}, s)] - \gamma_0^2 \vec{A}_m(\vec{r}, s) \} + \frac{1}{\mu_0} \nabla \times \vec{A}(\vec{r}, s) \quad (15a)$$

$$\vec{E}^S(\vec{r}, s) = \frac{s}{\gamma_0^2} \{ \nabla[\nabla \cdot \vec{A}(\vec{r}, s)] - \gamma_0^2 \vec{A}(\vec{r}, s) \} + \frac{s}{(\sigma_0 + s\epsilon_0)} \nabla \times \vec{A}_m(\vec{r}, s) \quad (15b)$$

In Eqns. (15a) and (15b), the electric vector potential is given by

$$\vec{A}_m(\vec{r}, s) = \frac{(\sigma_0 + s\epsilon_0)}{4\pi s} \iint_{S_a} \vec{M}_{\text{eq}}(\vec{r}_a', s) G(\vec{r}, \vec{r}_a', s) dS_a' \quad (16a)$$

$$G(\vec{r}, \vec{r}_a', s) = \frac{e^{-\gamma_0 |\vec{r} - \vec{r}_a'|}}{|\vec{r} - \vec{r}_a'|} \quad (16b)$$

$$|\vec{r} - \vec{r}_a'| = [(x - x_a')^2 + (y - y_a')^2 + (z - z_a')^2]^{1/2} \quad (16c)$$

and the magnetic vector potential is given by

$$A(\vec{r}, s) = \frac{\mu_0}{4\pi} \int \int_{S_a} J_{s_{eq}}(\vec{r}', s) G(\vec{r}, \vec{r}', s) dS_a' \quad (16d)$$

where the propagation constant is

$$\gamma_0 = [\pm \mu_0(\sigma_0 + s\epsilon_0)]^{1/2} = jk_0. \quad (16e)$$

Taking the limit  $r \rightarrow \infty$  gives the required far-field scattering distribution [17].

In order to validate the feasibility of the proposed hybrid method, the scattering of a transverse-magnetic (TM) polarized plane wave by a two-dimensional conducting cylinder of arbitrary cross section was considered during the present research program. This canonical problem, shown in Figure 6, is well documented [17, 21, 22] and therefore serves as a good test of feasibility and accuracy of the hybrid method.

The near-field to far-field transformation discussed above is now specialized for this two-dimensional canonical problem. Assuming that  $k_0$  is the free-space propagation constant and  $\eta_0$  is the intrinsic impedance equal to  $\sqrt{\mu_0/\epsilon_0}$ , we have in the far-field region:

$$E_z^S = -j\omega\mu_0\Psi_{z_{eq}} + jk_0[-F_{x_{eq}}\sin\phi + F_{y_{eq}}\cos\phi] \quad (17a)$$

where

$$\Psi_{z_{eq}} \sim \eta_0 k_0 K \int_{S_a} J_{s_{eq_z}}(x', y') e^{+jk(x'\cos\phi + y'\sin\phi)} dx' \quad (17b)$$

$$F_{x,y_{eq}} \sim \eta_0 k_0 K \int_{S_a} M_{s_{eq_{x,y}}}(x', y') e^{+jk(x'\cos\phi + y'\sin\phi)} dx' \quad (17c)$$

$$K = \frac{e^{-jkr}}{\sqrt{8\pi kr}} e^{-j\frac{3\pi}{4}} \quad (17d)$$

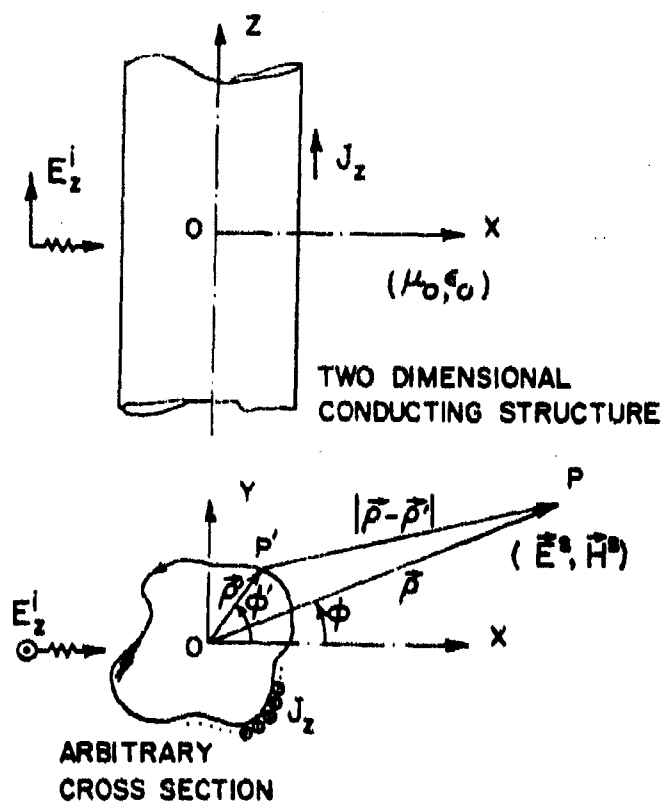


Figure 6. GEOMETRY OF TWO-DIMENSIONAL SCATTERING, TM POLARIZATION CASE

and the scattering cross section based on the equivalent currents is given by:

$$RCS_{eq} = \lim_{\rho \rightarrow \infty} \{ 2\pi\rho |E^S(\phi)/E^i|^2 \} . \quad (17e)$$

For comparison, the far fields and scattering cross section obtained by the usual surface electric currents ( $J_z$ ) approach is based upon solving the following integral equation using the method of moments (MOM):

$$E_z^i(\vec{\rho}) = \frac{k_0 n_0}{4} \int_C J_z(\vec{\rho}') H_0^{(2)}(k_0 |\vec{\rho} - \vec{\rho}'|) d\ell' \quad \text{for } \vec{\rho} \in C \quad (18a)$$

$$E_z^i(\vec{\rho}) = E_0 e^{-jk_0 \rho \cos(\phi - \phi^i)} \quad (18b)$$

In Eqns. (18a) and (18b),  $\phi^i$  is the angle of incidence (angle between the x axis and the direction of propagation), and  $H_0^{(2)}$  is the Hankel function of the second kind and zero order. Now, the far-field distribution is obtained directly from the induced cylinder currents,  $J_z$ , by:

$$E_z^S(\phi) \sim \frac{k_0 n_0}{\sqrt{8\pi k_0 \rho}} e^{-j(k\rho + \frac{3\pi}{4})} \int_C J_z(x', y') e^{+jk(x' \cos\phi + y' \sin\phi)} d\ell \quad (19)$$

The scattering cross section is again given by Equation (17e).

#### 2.2.6 Penetrating Near-Field Information via the Schelkunoff Aperture Electric Current Equivalence Principle [13]

The analysis of the electromagnetic excitation of an aperture on an arbitrarily shaped object is a complex problem [23]. This problem has been given special attention in the broad area of EMP penetration and simulation studies [24] with great efforts being applied to assess coupling to objects present behind apertures on finite, metallic, hollow scattering bodies.

The problem of the penetration and coupling of electromagnetic energy through an aperture has been studied extensively by many investigators using

analytical and method-of-moments (MOM) numerical approaches [21] to characterize the behavior of simple aperture shapes in a conducting screen [25] - [29] or in a finite, scattering body [30, 31]. However, the analysis becomes very complex if there are other scattering objects in the vicinity which are coupled to the aperture [23], [32, 33] wherein the mutual interaction must be fully taken into account.

One powerful alternate approach is the pure FD-TD method previously discussed in References [12] and [13] which allows computation of the penetrated internal electromagnetic fields by direct modeling of the complete object of interest, including apertures and internal contents. However, the pure FD-TD method is best suited for modeling localized regions. When such a region is part of a larger structure that significantly affects the electromagnetic excitation, it becomes difficult to account for the physics of the entire coupling problem using a single FD-TD model having a constant space lattice cell size. In fact, electromagnetic coupling problems involving the need to account simultaneously for the effects of both large and small spatial details (the "global-local problem") have been difficult to structure with any single analytical or numerical technique.

In order to treat such coupling problems more effectively, a new hybrid MOM/FD-TD technique was developed based on a novel use of a field equivalence theorem due to Schelkunoff [13], [20], [34, 35]. This hybrid technique, described in this section, is basically an equivalent aperture excitation method. This allows analysis of the coupling problem in two distinct steps:

- Step 1- Analysis of the relatively simple exterior problem using MOM to compute the equivalent excitation currents in the apertures leading to the interior region. This can be done independent of any knowledge of the contents of the interior region.
- Step 2- Use of the FD-TD method to analyze the relatively complex interior region, assuming as an excitation the equivalent currents found in Step 1.

In this way, each analysis method is applied in the range of structure size and complexity that it is best suited for, allowing an overall solution that is accurate for large, simple structures that are penetrated by apertures leading to complex, interior cavities.

Figure 7a illustrates the classical problem of a perfectly conducting scatterer,  $S_C$ , with an aperture,  $S_A$ . External to the scatterer in Region 1, an incident field  $(\vec{E}^i, \vec{H}^i)$  illuminates the aperture, and part of the energy penetrates into the cavity (Region 2) through the aperture. To compute the total field  $(\vec{E}_2, \vec{H}_2)$  in Region 2, many analytical and MOM numerical approaches studied in the literature have employed integral-equation formulations treating Regions 1 and 2 simultaneously. These approaches characterize either  $S_A$  or  $S_C$  in terms of tangential fields or equivalent surface currents [20], [21].

An alternative is to employ a field equivalence theorem due to Schelkunoff (Theorem no. 3 in [20]) to permit sequential treatment of Region 1 and Region 2. This theorem is based upon an equivalent aperture electric current formulation which connects the exterior and interior regions. This formulation expresses fields in a region as the superposition of the so-called short-circuit fields  $(\vec{E}_{sc}, \vec{H}_{sc})$  with the aperture not present (shorted) plus the aperture field contribution,  $(\vec{E}^A, \vec{H}^A)$ , maintaining the required continuity of the fields across the aperture. The first partial field,  $(\vec{E}_{sc}, \vec{H}_{sc})$ , is simply equal to zero in the Region 2. The second partial field, designated  $(\vec{E}^A, \vec{H}^A)$ , is generated by the non-physical current distribution,  $\vec{J}_O^A$ , flowing through the empty space of the open-circuit aperture locus, where  $\vec{J}_O^A = -\vec{J}_O^A$ , the short-circuit aperture current distribution.

In Figures 7b and 7c, the MOM/FD-TD hybrid method is illustrated schematically, and is summarized below as a four-step computation.

#### Region 1: MOM Technique

- (a) The aperture region,  $S_A$ , is short-circuited, and the straightforward exterior problem is solved via MOM to obtain the induced electric current distribution,  $\vec{J}_O^A$ , in the short-circuited aperture region (Figure 7b).
- (b)  $\vec{J}_O^A$  is now placed in the open aperture region with a sign change (Figure 7c) to account for the continuity of the fields in the aperture region. The electric current,  $-\vec{J}_O^A$ , non-physically placed in the open aperture region acts as an equivalent source for the fields in Regions 1 and 2.

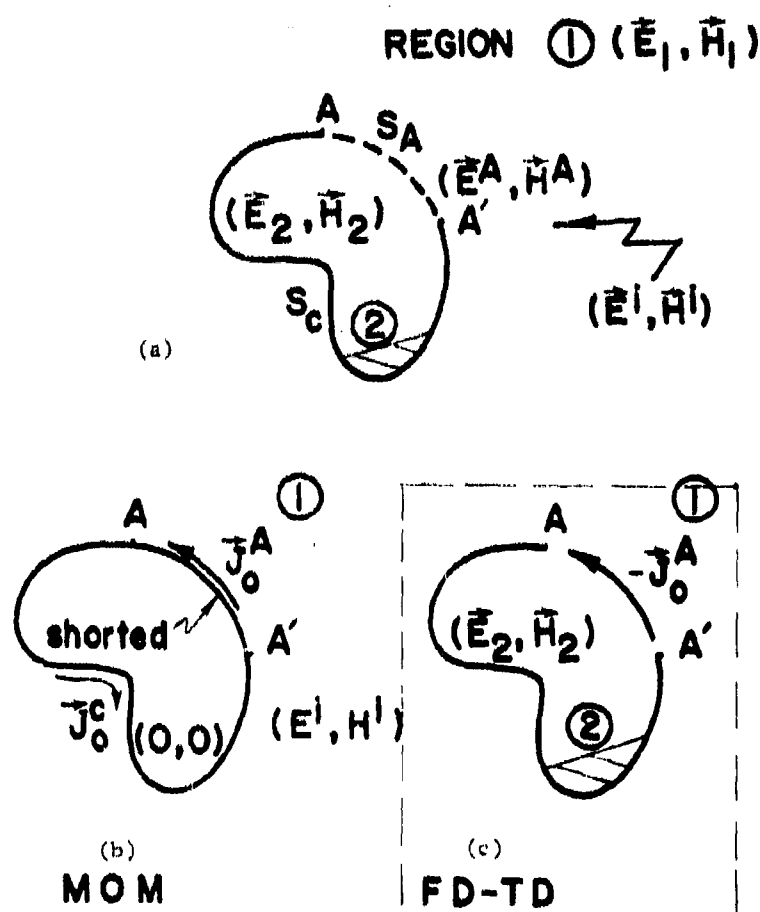


Figure 7. HYBRID MOM/FD-TD TECHNIQUE FOR COMPUTING PENETRATION INTO CAVITIES. (a) Original problem; (b) MOM solution of exterior problem for shorted-aperture case; (c) FD-TD solution of interior problem using equivalent aperture-current excitation

## Region 2: FD-TD Technique

- (c) We note that the MOM technique gives the equivalent current source distribution,  $-\vec{J}_0^A$ , in the frequency domain as a spatial distribution of phasor quantities having both magnitude (relative to the incident fields) and phase (relative to some phase reference, normally at the origin of the coordinate system). With the FD-TD method being a time-domain technique, the phase distribution of  $-\vec{J}_0^A$ , is interpreted as a time-delay distribution with respect to the original phase reference location. The magnitude distribution is taken intact without interpretation or modification. In this manner, the FD-TD aperture equivalent current source distribution assumes sinusoidal steady-state quantities starting at the very beginning of time-stepping, with the proper time delay to account for phase shift.
- (d) Using the FD-TD approach, the interior fields ( $\vec{E}_2, \vec{H}_2$ ) are computed directly by using  $-\vec{J}_0^A$  as a source term distribution in the  $\nabla \times \vec{H}$  difference equations. For example, if  $-\vec{J}_0^A$  is a source term, Eqn. (8d) is re-written for the aperture points as:

$$\begin{aligned}
 m &= \text{MEDIA}(i+\frac{1}{2}, j, k) \\
 \vec{E}_x^{n+1}(i+\frac{1}{2}, j, k) &= C_a(m) \vec{E}_x^n(i+\frac{1}{2}, j, k) + C_b(m) [H_z^{n+\frac{1}{2}}(i+\frac{1}{2}, j+\frac{1}{2}, k) \\
 &\quad - H_z^{n+\frac{1}{2}}(i+\frac{1}{2}, j-\frac{1}{2}, k) + H_y^{n+\frac{1}{2}}(i+\frac{1}{2}, j, k-\frac{1}{2}) - H_y^{n+\frac{1}{2}}(i+\frac{1}{2}, j, k+\frac{1}{2}) \\
 &\quad - J_{0x}^{n+\frac{1}{2}}(i+\frac{1}{2}, j, k)] \quad (20)
 \end{aligned}$$

Here, specifying  $\vec{J}_0^A$  in the aperture is equivalent to specifying the addition of a discontinuity in the z-directed tangential magnetic field,  $H_z$ , across the aperture source plane. Namely, we have added

$$J_{0x} = H_z^- - H_z^+ \quad (21)$$



where  $H_2^-$  and  $H_2^+$  are tangential magnetic fields located an infinitesimal distance to either side of the equivalent aperture source plane. This procedure is consistent with the partial-field approach discussed by Schelkunoff [20].

Note that, unlike possible hybrid MOM/MOM methods, the hybrid MOM/FD-TD method does not require computation of an equivalent aperture electric field excitation,  $E^A$ . This is because the interior-region FD-TD solution easily accepts the non-physical aperture electric current distribution,  $-J_0^A$ , as the excitation. Thus, there is no need to set up and solve for the mutual interactions of the cavity contents and the apertures, and no need to compute the cavity Green's function. The hybrid MOM/FD-TD method easily permits the modeling of the cavity interior to as fine an extent as desired without any additional numerical complication. For realistic, general cavities having Green's functions that are difficult or impossible to compute, the hybrid MOM/FD-TD approach may be the only way to calculate the penetrated interior fields.

## 2.2.7 Thin-Wire Coupling Model

### 2.2.7.1 Simplified Model for Total-Field FD-TD Formulation

A very simple way of approximating electromagnetic coupling to a round, thin wire having a diameter,  $2r_w$ , less than the FD-TD lattice-cell size,  $\delta$ , is indicated in Reference [13]. This method can be easily used when the wire of interest is embedded in a total-field modeling region of the FD-TD lattice. It is based upon modeling the thin wire as a thicker, square-cross section wire occupying exactly one cell of the lattice. Simply, the electrical conductivity,  $\sigma_m$ , assigned to the E components tangential to the model-wire space cells is adjusted so that the high-frequency internal impedance of the model wire equals that of the actual thin wire of interest. For example, the high-frequency internal impedance of a thin wire is given by [36]

$$Z_{i\_wire} = \left( \frac{\pi f \mu_w}{\sigma_w} \right)^{1/2} \frac{(1+j)}{2\pi r_w} \text{ ohms/meter} \quad (22a)$$

where  $f$  is the frequency of the wave excitation,  $\mu_w$  is the permeability of the wire material,  $\sigma_w$  is the conductivity of the wire material, and  $r_w$  is the radius of the wire. The high-frequency internal impedance of a model wire having a square cross section occupying one lattice cell is well approximated by

$$Z_{i\_model} = \left( \frac{\pi f \mu_0}{\sigma_m} \right)^{1/2} \frac{(1+j)}{4\delta} \text{ ohms/meter} \quad (22b)$$

where  $\mu_0$  is the vacuum permeability,  $\sigma_m$  is the conductivity of the model wire material, and  $\delta$  is the width of the model wire (one lattice cell size). Equating (22a) and (22b), the desired conductivity of the model wire is given by

$$\sigma_m = \frac{\mu_0}{\mu_w} (\pi r_w / 2\delta)^2 \sigma_w \text{ mhos/m} \quad (22c)$$

It should be pointed out that this procedure achieves extreme simplicity at the expense of neglecting the exact geometrical relation of the thin wire and its surroundings. The internal impedance of the thin wire is adequately modeled here, but the precise capacitance and inductance linking the thin wire to adjacent structures is somewhat in error due the larger effective radius used for the model wire. The following discussion summarizes a procedure for taking into account the radius of the thin wire with regard to these external impedances. This procedure is considerably more complicated than the above, and is usable mainly for a scattered-field version of the FD-TD method. The relative accuracy of the two approaches remains to be determined.

## \*\*2.2.7.2 Holland-Simpson Model [8] for Scattered-Field FD-TD Formulation

Holland and Simpson [8] have recently described a scattered-field-only FD-TD code (which they name "THREDE") that permits the modeling of electromagnetic coupling to thin wires having a diameter of less than one space cell of the FD-TD lattice. This sub-section summarizes the theoretical background and the thin-wire coupling algorithm published by these authors.

Figure 8 shows a cross section of a FD-TD cell with a wire running perpendicularly to the plane of the figure. Holland and Simpson separate the electromagnetic field into an incident and a scattered part

$$\vec{E} = \vec{E}^s + \vec{E}^i \quad (23a)$$

$$\vec{H} = \vec{H}^s + \vec{H}^i \quad (23b)$$

They then write Maxwell's equations in polar coordinates about the wire center. The  $\theta$  component of the curl- $\vec{E}$  equation is given by

$$\frac{\partial E_r^s}{\partial z} + \frac{\partial E_r^i}{\partial z} - \frac{\partial E_z^s}{\partial r} - \frac{\partial E_z^i}{\partial r} = -\mu_0 \left( \frac{\partial H_\theta^s}{\partial t} + \frac{\partial H_\theta^i}{\partial t} \right) \quad (24)$$

At  $r = a$ , there is the boundary condition

$$E_z^s + E_z^i = 0 \quad (25)$$

They integrate Equation (24) out to some radius  $r$  to yield

$$E_z^s(r) + E_z^i(r) = \mu_0 \frac{\partial}{\partial t} \left[ \int_a^r (H_\theta^s + H_\theta^i) d\rho + \frac{1}{\partial z} \int_a^r (E_r^s + E_r^i) d\rho \right] \quad (26)$$

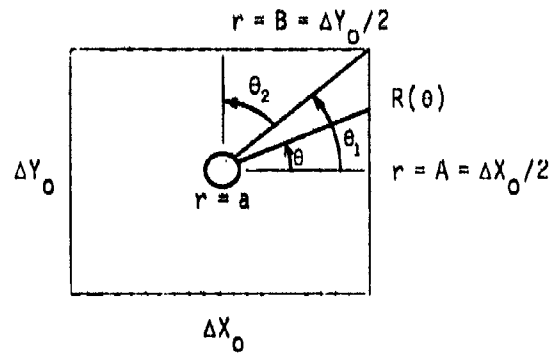
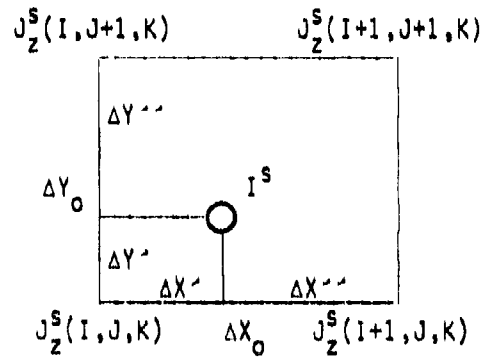


Figure 8. GEOMETRY FOR COMPUTING THE IN-CELL INDUCTANCE OF A WIRE IN A CELL OF RECTANGULAR CROSS SECTION [8]



$$J_2^S(I, J, K) = (\Delta X' / \Delta X_0) (\Delta Y' / \Delta Y_0) I^S / (\Delta X_0 \Delta Y_0)$$

$$J_2^S(I+1, J, K) = (\Delta X' / \Delta X_0) (\Delta Y'' / \Delta Y_0) I^S / (\Delta X_0 \Delta Y_0)$$

$$J_2^S(I, J+1, K) = (\Delta X'' / \Delta X_0) (\Delta Y' / \Delta Y_0) I^S / (\Delta X_0 \Delta Y_0)$$

$$J_2^S(I+1, J+1, K) = (\Delta X'' / \Delta X_0) (\Delta Y'' / \Delta Y_0) I^S / (\Delta X_0 \Delta Y_0)$$

Figure 9. PARTITIONING  $I^S$  INTO CURRENT DENSITIES  $J_2^S$  AT THE FOUR CLOSEST  $E_2^S$  MESH POINTS [8]

By hypothesis, the cell sizes, and thus all  $r$ 's of interest, are small compared to the shortest wavelength present. Then, in an average sense around  $\theta$ , Holland and Simpson write

$$H_{\theta}^s + H_{\theta}^i = \frac{I^s + I^i}{2\pi r} \quad (27)$$

$$E_r^s + E_r^i = \frac{Q^s}{2\pi r \epsilon_0} \quad (28)$$

where  $I$  is the current on the wire and  $Q$  is the charge per unit length on the wire. If the wire is driven by current injection,  $I^i$  locally represents the relevant injected current. (Normally, a scatterer would not be excited by an incident field and current injection in the same event. Thus, Holland and Simpson usually have either  $E^i = 0$  or  $I^i = 0$ ). The  $I^s$  and  $Q^s$  represent the scattered current and charge per unit length on the wire. Holland and Simpson use Equations (27) and (28) to re-express Equation (26) as

$$\begin{aligned} E_z^s(r) + E_z^i(r) = & \frac{\partial(I^s + I^i)}{\partial t} \cdot \mu_0 \frac{\ln(r/a)}{2\pi} \\ & + \frac{\partial Q^s}{\partial z} \cdot \frac{\ln(r/a)}{2\pi \epsilon_0} \end{aligned} \quad (29)$$

They provide similar treatment of the  $r$  component of the  $\text{curl } \vec{H}$  equation, resulting in

$$\frac{\partial Q^s}{\partial t} + \frac{\partial I^s}{\partial z} = - \frac{\partial I^i}{\partial z} \quad (30)$$

(Integrating over  $\theta$  from 0 to  $2\pi$  to obtain the average around  $\theta$  causes the  $(1/r)(\partial H_z / \partial \theta)$  term in the  $\text{curl } \vec{H}$  equation to go to zero. Equation (30) alternatively can be interpreted as merely a statement of conservation of charge on the wire.)

Holland and Simpson point out that the incident quantities  $E^i$ ,  $H^i$ , and  $I^i$  are known, externally-defined variables and are input quantities to their THREDE FD-TD system. However, they note that the scattered quantities  $E^s$ ,  $H^s$ ,  $Q^s$ , and  $I^s$  are unknowns which are solved for by means of their FD-TD program.

They next re-write Equation (29) as

$$E_z^s(r) + E_z^i(r) = \begin{cases} \left[ \mu_0 \frac{\partial(I^s + I^i)}{\partial t} + \frac{1}{\epsilon_0} \frac{\partial Q^s}{\partial z} \right] \frac{\ln(r/a)}{2\pi}, & r > a \\ 0, & r \leq a \end{cases} \quad (31)$$

They state that most of the uncertainty in their modeling of the coupling to a thin wire depends on the next operation performed on Equation (31). Their common manipulation is to average Equation (31) over the area bounded by  $r = R$  where  $\pi R^2 =$  the cell area,  $\Delta X_0 \Delta Y_0$ . Averaging removes the  $r$  dependence of the equation and yields

$$L \left( \frac{\partial(I^s + I^i)}{\partial t} + \frac{1}{\epsilon_0 \mu_0} \frac{\partial Q^s}{\partial z} \right) = \langle E_z^s \rangle + \langle E_z^i \rangle \quad (32)$$

where  $L$  has the dimensions of inductance per unit length and is given by

$$L = \frac{\mu_0}{2\pi} \frac{\int_a^R \ln(r/a) r \, dr}{\int_0^R r \, dr} = \frac{\mu_0}{2\pi} \left( \ln(R/a) - \frac{1}{2} + \frac{a^2}{2R^2} \right). \quad (33)$$

Holland and Simpson found empirically [8] that the lower limit of  $r=0$  on the denominator integral of Equation (33) results in a better fit of their computed results to known analytic solutions of simple problems than does a choice of  $r=a$ . Thus, the limit choice used in Equation (33) is more pragmatic than rigorous. The numerator integral of this equation must begin at  $r=a$  because  $E_z^s + E_z^i$  vanishes for  $r \leq a$  as Equation (31) indicates.

Holland and Simpson implement their thin-wire coupling model by applying a finite-difference analog of Equations (30) and (32) as well as Maxwell's equations. Thus, a cell with a wire running through it requires eight quantities (six field components and  $Q^s$  and  $I^s$ ) to be advanced each program time step. For a wire segment parallel to the  $z$  axis, they found that it is easiest computationally to place  $I^s$  mesh points in the planes of  $E_z^s$  mesh points, and  $Q^s$  mesh points in the planes of  $H_z^s$  mesh points.

The Holland-Simpson thin-wire coupling algorithm therefore proceeds as follows [8]:

- 1) Evaluate  $\langle E^i \rangle$  and  $\partial I^i / \partial t = \dot{I}^i$  at the  $I^s$  mesh points.
- 2) Evaluate  $\langle E^s \rangle$  at the  $I^s$  mesh points. For a wire along  $z$ , it is desirable to run the wire through the  $E_z^s$  mesh points. Then  $\langle E_z^s \rangle$  is just  $E_z^s$  at that point. If the wire cannot conveniently be run through the  $E_z^s$  mesh point,  $\langle E_z^s \rangle$  should be interpolated from the four closest mesh points, as shown in Figure 8 or 9.
- 3) Advance  $I^s$  according to the following finite-difference analog of Equation (32):

$$I^s(k)^n = I^s(k)^{n-1} - \Delta t \dot{I}^i(k)^{n-1/2} + \frac{\Delta t}{L} \left( -E_z^s(k)^{n-1/2} + E_z^i(k)^{n-1/2} - L \frac{Q^s(k+1)^{n-1/2} - Q^s(k)^{n-1/2}}{\epsilon_0 \mu_0 \Delta z_0} \right) \quad (34)$$

- 4) Advance  $\bar{H}^S$  in the usual way from the curl- $\bar{E}$  equation.
- 5) Advance time by  $\Delta t/2$ .
- 6) Partition  $I^S + I^I$  among the four closest  $E_z^S$  mesh points according to Figure 9. If the wire runs through the  $E_z^S$  mesh point, as preferred, all  $I^S + I^I$  are associated with that mesh point,  $J_z^S(I, J, K) = (I^S(K) + I^I(K))/(\Delta x_0 \cdot \Delta y_0)$ .
- 7) Advance  $\bar{E}^S$  using the curl- $\bar{H}$  equation with  $\bar{J}^S$  as determined from partitioning the  $I^S + I^I$  according to step 6.
- 8) Advance  $Q^S$  according to the following finite-difference analog of Equation (30):

$$Q^S(K)^{n+1/2} = Q^S(K)^{n-1/2} - \Delta t \left( \frac{I^S(K)^n + I^I(K)^n - I^S(K-1)^n - I^I(K-1)^n}{\Delta z} \right) \quad (35)$$

- 9) Advance time by  $\Delta t/2$  and go back to step 1.

Holland and Simpson [8] also describe their treatment of wire junctions; evaluation of the in-cell inductance for non-cubic cells; boundary conditions for wires ending either in free space or at a conducting surface; resistive wires; and applications to a linear antenna and a circular loop antenna. The reader is referred to their paper for the details.

### 3.0 EXAMPLES OF COMPUTED RESULTS OF THE FD-TD METHOD

#### 3.1 Pure FD-TD Method, Three-Dimensional Penetration Problems

##### 3.1.1 Empty Cylindrical Metal Cavity, Broadside Incidence, Transverse Electric (TE) Polarization Case [13].

This problem involved the computation of the fields within a 19.0-cm diameter, 68.5-cm long, circular aluminum cylinder with one open end. The incident plane wave was assumed to have a frequency of 300 MHz, have the



field components  $E_{z,inc}$  and  $H_{x,inc}$ , and propagate perpendicular to the cylinder axis with a transverse electric (TE) polarization. Since the cutoff frequency of the cylinder (as a waveguide) is above 900 MHz, the interior fields are expected to decay with distance from the aperture.

The geometry of the cylinder model relative to the 160 x 63 x 24-cell (1,450,000 unknown field components) FD-TD problem lattice is depicted in Figure 10 at lattice symmetry plane  $k = 24$  and in Figure 11 at a typical  $i = \text{constant}$  plane cutting through the cylinder transversely. Like the axial-incidence case discussed in [11],  $\delta = 0.5 \text{ cm} = \lambda_0/200$  was used;  $\delta t = 8.33 \text{ psec}$ ; and aluminum  $\sigma = 3.7 \cdot 10^7 \text{ mho/m}$ . First-order correct radiation conditions were available at the time; thus, an air conductivity,  $\sigma = 0.01 \text{ mho/m}$ , was used to attenuate scattered waves and accelerate convergence of the interior fields.  $2.5 \cdot 10^6$  words of memory and 9.4 minutes of central processor time were required on the Control Data Star 100 for a complete run of 800 time steps (2.0 periods of the incident wave at 300 MHz).<sup>1</sup>

Figure 12 compares the FD-TD computed  $|H_x/H_{x,inc}|$  along the cylinder axis with computed results by D. Wilton and A. Glisson using a frequency-domain, MOM, body-of-revolution computer program [37]. The FD-TD results, shown as a solid curve, are after 800 time steps; the MOM results are graphed as a dashed curve. Excellent agreement (within 0.5 dB) of the results of the two approaches is seen over the first 15 cm of field penetration into the cylinder. Over this span, the total  $H_x$  field decay is of the order of 50-55 dB. The rate of decay of  $H_x$  computed by either technique equals 3.3 dB/cm, which compares favorably with the 3.46 dB/cm rate predicted by simple waveguide mode theory for this beyond-cutoff case.

Figure 13 graphs contour maps of the FD-TD computed field components at the horizontal symmetry plane of the cylinder in an attempt to indicate the level of detail achieved.

<sup>1</sup>The computer memory and running time remains unchanged if the cavity is loaded by arbitrary metal and dielectric contents, for a fixed number of time steps.

Broadside incidence, TE polarization case:  $f = 300 \text{ MHz}$ ;  $E_{\text{inc}} = 1 \text{ V/m}$

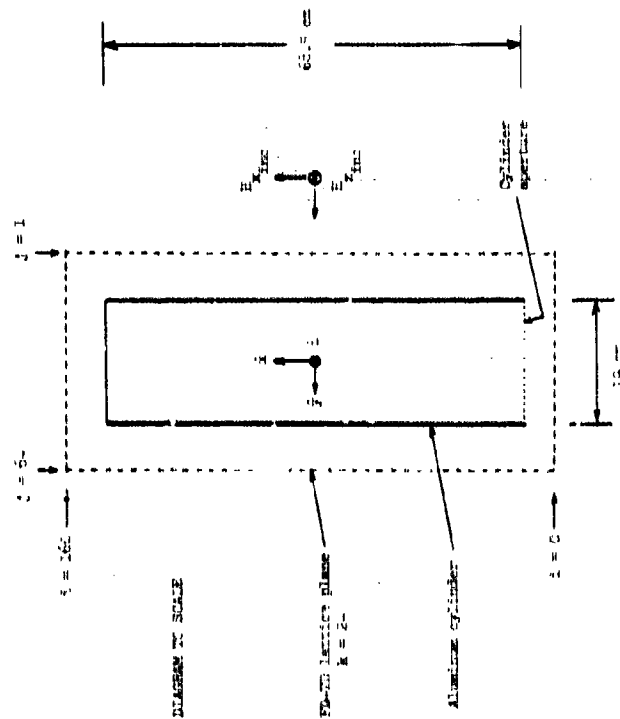


Figure 10. FD-TD MODEL GEOMETRY OF  
OPEN-ENDED ALUMINUM CYLINDER AT  
HORIZONTAL SYMMETRY PLANE

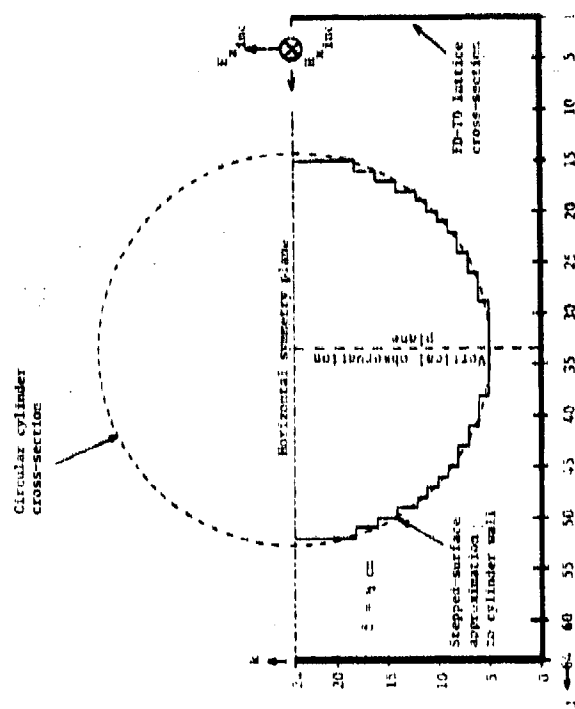


Figure 11. TRANSVERSE CROSS SECTION  
OF CYLINDER MODEL OF FIGURE 10

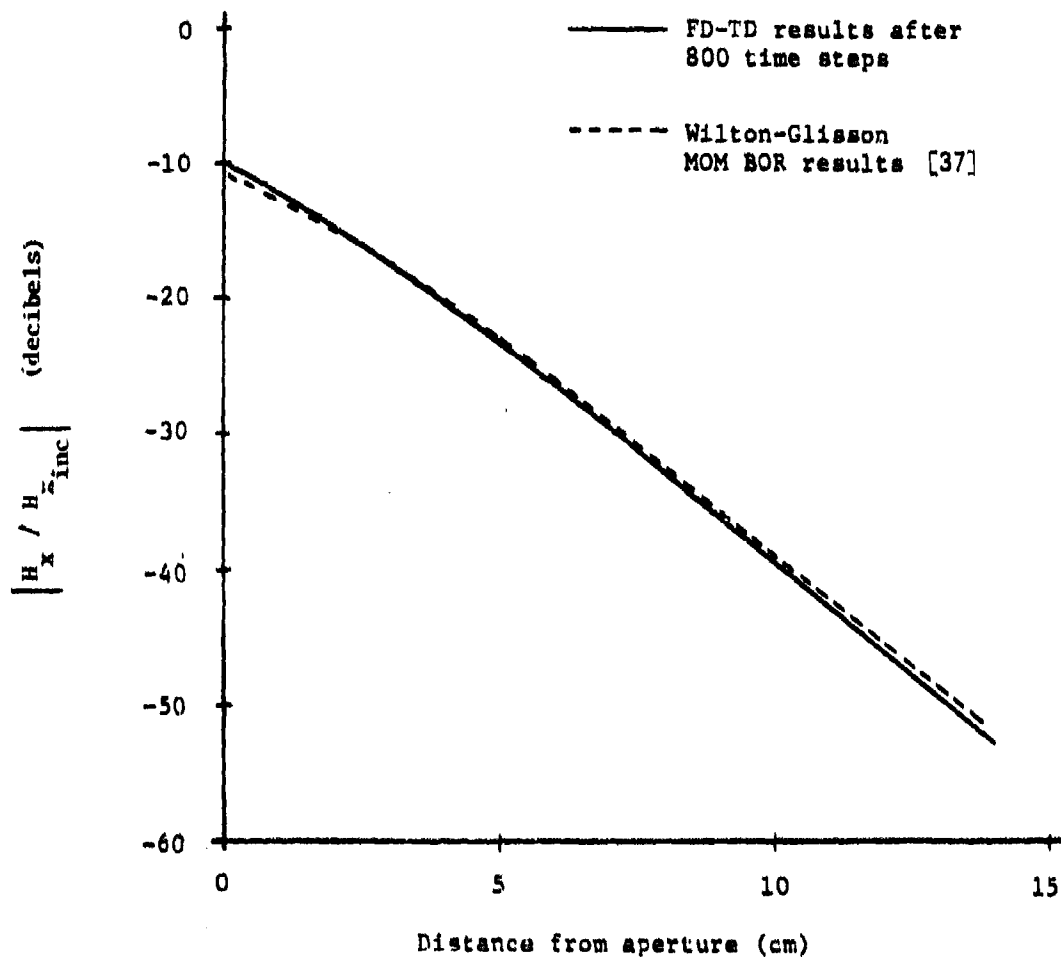


Figure 12. COMPARISON OF RESULTS FOR THE LONGITUDINAL MAGNETIC FIELD ALONG THE CYLINDER AXIS OF FIGURES 10 AND 11

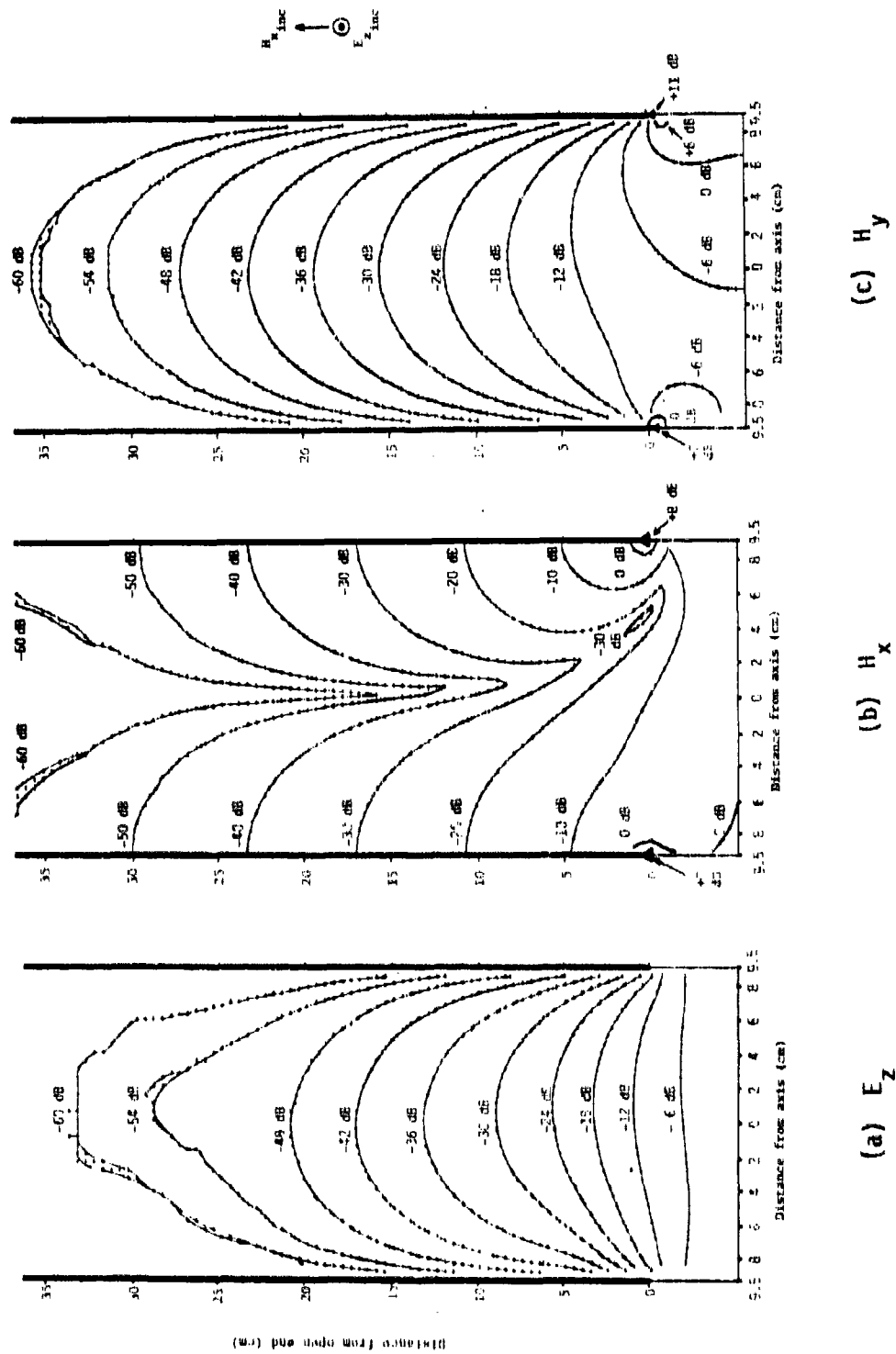


Figure 13. FD-TD COMPUTED FIELD CONTOURS IN HORIZONTAL SYMMETRY PLANE OF CYLINDER OF FIGURES 10 AND 11

### 3.1.2 Loaded Missile Guidance Section, Axial Incidence Case [13].

This problem involved the computation of the fields within a detailed model of a metal-coated missile guidance section, as shown in cross-section in Figures 14 and 15, illuminated at axial incidence by the 300 MHz plane wave,  $(E_{z_{inc}}, H_{x_{inc}})$ .

Two apertures were modeled: a circular one in the nose (behind the magnesium fluoride infrared dome); and a circumferential sleeve fitting 23 cm aft. The missile body beyond the sleeve fitting was assumed to continue to infinity with a constant cross-section shape. The following metal and dielectric interior components were modeled:

- 1) Head coil assembly (assumed solid metal);
- 2) Cooled detector unit - CDU (assumed solid metal);
- 3) Phenolic ring around the CDU;
- 4) Preamp can (metal);
- 5) Wire<sup>1</sup> connecting the CDU to the preamp can;
- 6) Wire<sup>1</sup> connecting the preamp can to the metal backplane; and
- 7) Longitudinal metal support rods.

The following electrical parameters were assumed for the media comprising the model:

Medium	Relative Permittivity, $\epsilon'_r$	Conductivity $\sigma$ (mhos/m)
Aluminum	1.0	$3.7 \cdot 10^7$
Fiberglass	5.5	$2.4 \cdot 10^{-3}$
Phenolic	4.5	$8.0 \cdot 10^{-4}$
Magnesium fluoride	5.3	0.0

<sup>1</sup>The two wires were really idealizations of a more complex situation in which two multiconductor wire bundles extended between the structures mentioned. By using a simple, single-wire model for each bundle, only the bulk current of each bundle (net metal-to-metal current) was modeled using the FD-TD method. The wire model was that of Section 2.2.7.1 of this report.

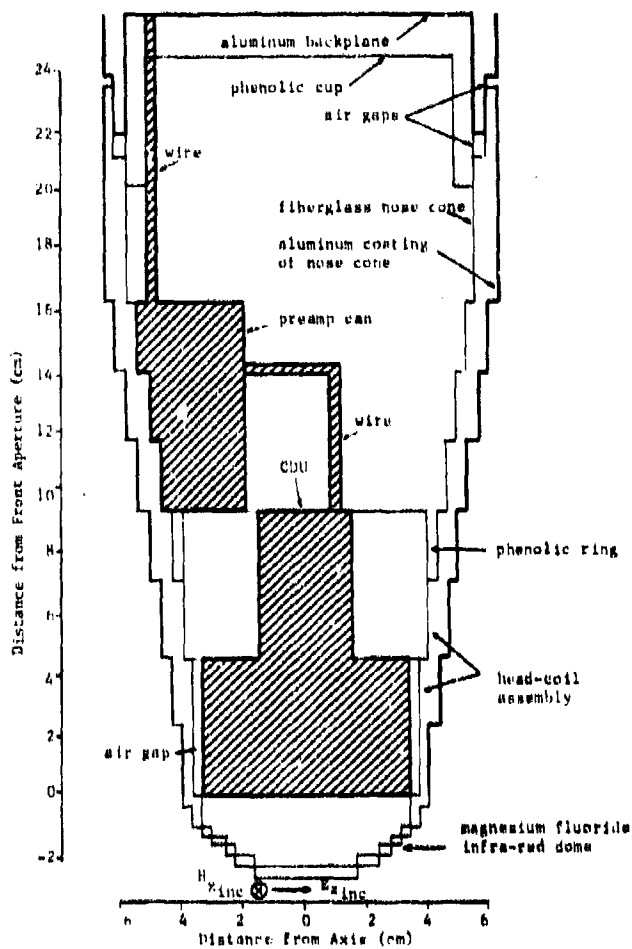


Figure 14. GEOMETRY OF GUIDANCE SECTION  
MODEL AT VERTICAL SYMMETRY PLANE.  
SHOWING COMPONENT MATERIALS

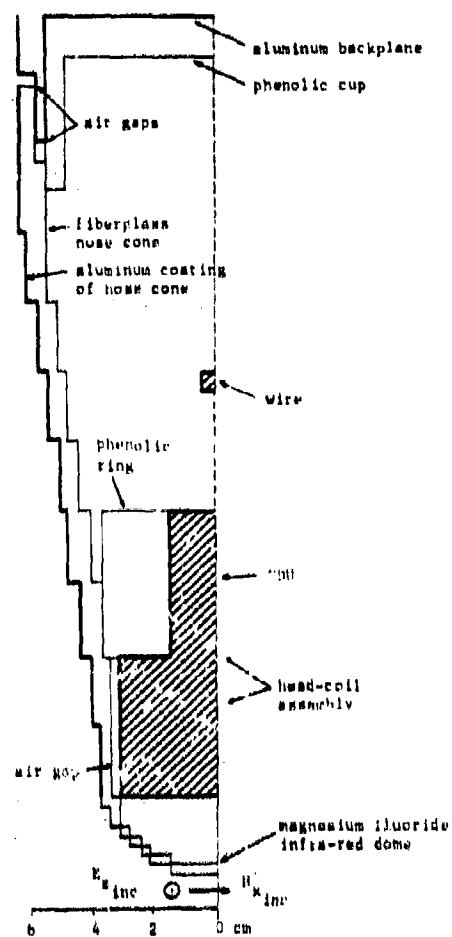


Figure 15. GEOMETRY OF GUIDANCE  
SECTION MODEL AT HORIZONTAL  
OBSERVATION PLANE

Since only first-order correct radiation conditions were available at the time, an air conductivity,  $\sigma = 0.025$  mho/m, was used to attenuate scattered waves. To accelerate convergence of the interior fields, an air conductivity,  $\sigma = 0.025$  mho/m, was applied to the total fields within the guidance section.

The model was implemented on a  $24 \times 100 \times 48$ -cell (690,000 unknown field components) FD-TD problem lattice. A lattice resolution  $\delta = 1/3$  cm  $= \lambda_0/300$  was used, with a time step  $\delta t = \delta/2c = 5.55$  ps.  $1.6 \cdot 10^6$  words of memory and 7.0 min of Control Data Star-100 central processor time were required to complete an 1800 time-step run (3.0 cycles of the incident wave).

Figure 16 graphs contour maps of the FD-TD computed field components at the vertical symmetry plane of the guidance section. An important observation is that the wires connecting the cooled detector unit, preamp can, and metal backplane are paralleled by high-level magnetic field contours (Figure 16b). This is indicative of substantial, uniform current flow along each wire. Such current flow would generate locally a magnetic field looping around the wire which, when "cut" by the vertical symmetry plane, shows up as parallel field contours spaced equally on each side of the wire. Using a simple Ampere's law argument,  $I_{\text{wire}}$  can be computed as being equal to  $H \cdot 2\pi r_0$ , where  $H$  is the magnitude of the parallel magnetic field contour and  $r_0$  is its separation from the wire center. In this manner, Table 1 lists the predicted values of  $I_1$  (current in the wire from the cooled detector unit to the pre-amp can) and  $I_2$  (current in the wire from the pre-amp can to the backplane). For the case of  $I_1$ , it is assumed that  $H = H_{\text{inc}}$  and  $r_0 = 1.5 \cdot \delta = 0.005$  m. For the case of  $I_2$ , it is assumed that  $H = 3.16H_{\text{inc}}$  and  $r_0 = 1.5 \cdot \delta = 0.005$  m.

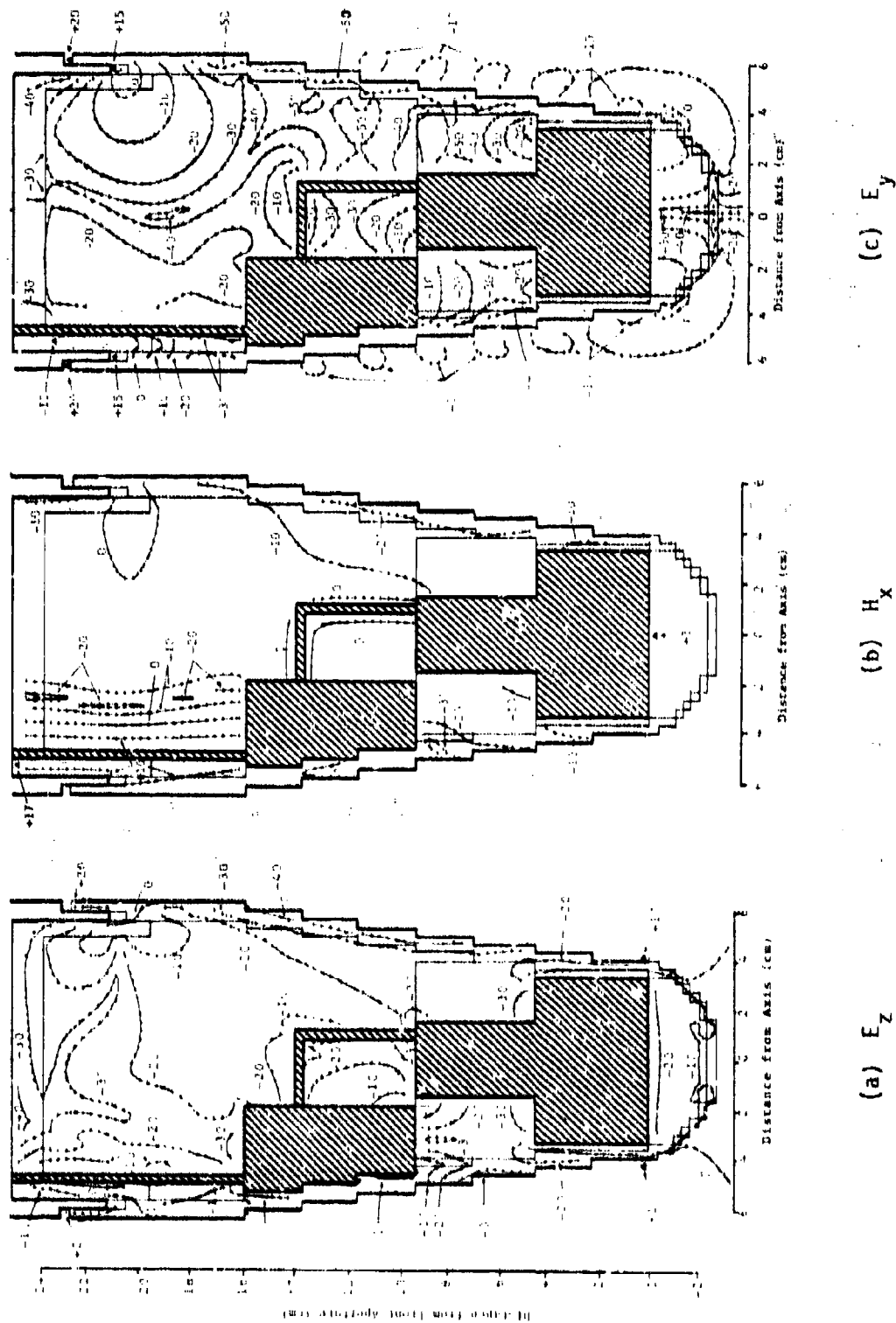


Figure 16. FD-TD computed field contours in vertical symmetry plane of guidance section of Figs. 14 and 15



TABLE 7  
PREDICTED GROUND WIRE CURRENTS

$E_{inc}$ (V/m)	$H_{inc}$ (A/m)	$P_{inc}$ ( $\mu$ W/cm <sup>2</sup> )	$I_1$ ( $\mu$ A)	$I_2$ ( $\mu$ A)
0.1	$2.65 \cdot 10^{-4}$	$2.65 \cdot 10^{-3}$	8.3	26.3
1.0	$2.65 \cdot 10^{-3}$	0.265	83	263
10.0	$2.65 \cdot 10^{-2}$	26.5	830	2630

The missile guidance section model demonstrates the capability of the pure FD-TD method to map fields penetrating into a complex structure that has multiple apertures and interior dielectric and metallic materials. Determination of the accuracy bound for this method, as applied to such complex structures, awaits the results of future experimental programs since alternative numerical approaches cannot deal with this level of complexity.

### 3.2 Hybrid MOM/FD-TD Method. Three-Dimensional Penetration Problem--Loaded Missile Guidance Section, Axial Incidence Case [13], [34], [35]

The MOM/FD-TD hybrid model for the axial-incidence case of the loaded missile guidance section (as shown in Figures 17 and 14, 15) was run for 1800 time steps (3.0 cycles of the incident wave at  $f = 300$  MHz). The excitation consisted of data for the magnitude and phase of the electric current distribution over the loci of the short-circuited nose aperture and sleeve-fitting aperture (as required by Schelkunoff's third theorem) computed using a MOM body-of-revolution code [37]. The results were compared to pure FD-TD results presented above in an attempt to establish the consistency of the MOM/FD-TD model for this case.

Figure 18 plots the comparison of the hybrid MOM/FD-TD results for the  $H_x$  field contours in the vertical symmetry plane with the pure FD-TD results already presented in Figure 16b. It is seen that, for both methods stepped to 1800 time steps, there is an excellent agreement for the 0 dB contours

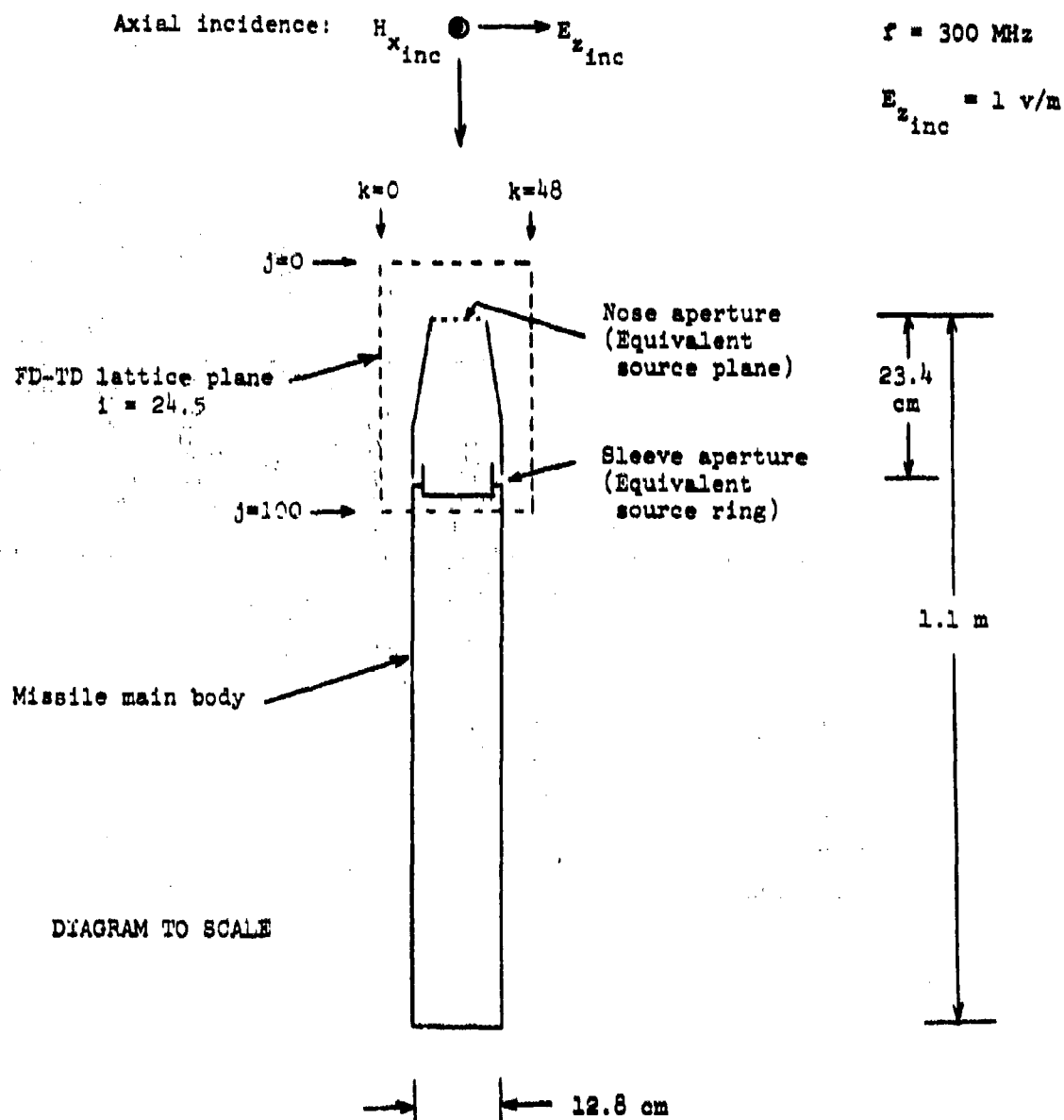


Figure 17. HYBRID MOM/FD-TD MODEL OF LOADED MISSILE GUIDANCE SECTION FOR AXIAL INCIDENCE CASE



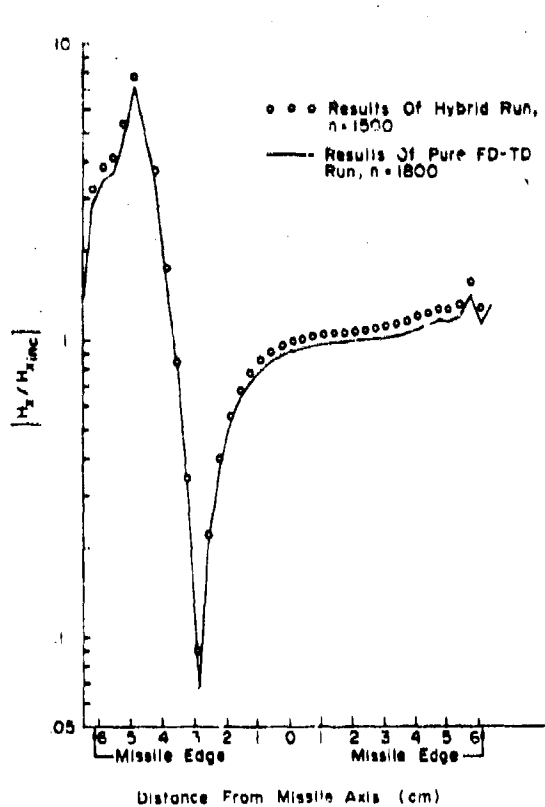
near the wire connecting the cooled detector unit to the pre-amp can. For this contour, the maximum spatial shift is only about 0.16 cm ( $\sim 0.5\delta$ ) in a direction further out from the wire. Further, there is observed to be excellent agreement of the +10 dB contour near the wire connecting the pre-amp can to the metal backplane. For this contour, the maximum spatial shift is only about 0.1 cm ( $\sim 0.3\delta$ ) in a direction further out from the wire. This implies that the currents in these two major wires are predicted to be almost the same by both the pure FD-TD method and the hybrid MOM/FD-TD method.

Figure 19 plots the comparison of the hybrid results for the  $H_x$  and  $E_z$  fields along with a vertical cut through the center of the guidance section at a point 21 cm in back of the nose aperture (about 2 cm in front of the sleeve fitting, at the point where the circumferential slot opens into the interior of the nose cone). The hybrid run results are after 1500 time steps, while the pure FD-TD results are after 1800 time steps. For this case, a very high level of agreement is observed between the two sets of data at all points of comparison. The worst-case difference between the results is only 1 dB, with most results consistent within only fractions of a decibel.<sup>1</sup>

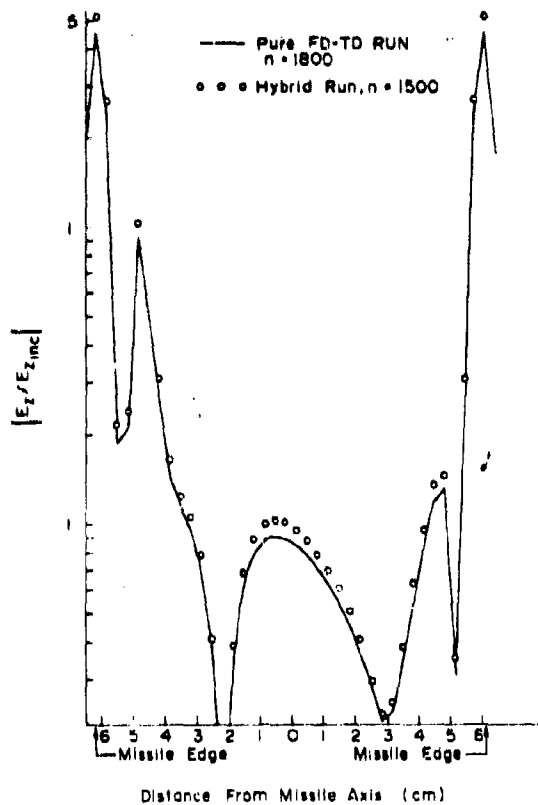
This case study shows that the hybrid MOM/FD-TD approach yields results for the missile guidance section wire current and electromagnetic fields which are consistent with the pure FD-TD data. The study implies that a wire passing very close to an aperture, and strongly coupled to that aperture (as for the case of the pre-amp can-to-backplane wire near the sleeve-fitting aperture), can be consistently modeled using the pure FD-TD approach

---

<sup>1</sup> Comparison of the data sets for the 1800 time-step case for each set results in slightly lessened agreement, such that the worst-case difference is about 1.7 dB. This may result from the hybrid program progressing to the sinusoidal steady state at a slightly faster rate than the pure FD-TD program, since a sinusoidal steady-state equivalent aperture current excitation is employed from the very beginning of the hybrid program, rather than an aperture excitation which must build to the steady state.



(a)  $H_x$



(b)  $E_z$

Figure 19. COMPARISON OF FD-TD AND HYBRID MOM/FD-TD DATA FOR FIELDS ALONG VERTICAL CUT THROUGH CENTER OF GUIDANCE SECTION NEAR SLEEVE-FITTING APERTURE

and the hybrid MOM/FD-TD approach. In the latter, it must be remembered that the MOM-derived equivalent aperture excitation takes into account none of the interior details of the structure. Finally, the study implies that complex sub-sections of large, simply-shaped structures are prime candidates for detailed modeling of the interior penetrating fields via the hybrid MOM/FD-TD method.

### \*\*3.3 Hybrid FD-TD Method, Two-Dimensional Scattering Problems

In order to validate the feasibility of the new formulation of the FD-TD lattice regions (Section 2.2.2), the new variable-angle plane wave source condition (Section 2.2.2), the new second-order correct lattice truncation conditions (Section 2.2.3), the new sinusoidal steady-state magnitude and phase computation (Section 2.2.4), and the new far-field scattering computation via the near-to-far field transformation (Section 2.2.5), several canonical, two-dimensional, conducting and dielectric structures were studied during the present research program. The numerical results<sup>1</sup> of the FD-TD computed surface electric current distribution and near electric and magnetic fields are presented for the case of a two-dimensional, square metal cylinder subject to TM-polarized illumination at normal and oblique incidence. These electric currents and near fields are compared to the MOM-computed results [21, 22]. The scattered-field pattern and the corresponding radar cross section (RCS) are derived from the near-to-far field transformation of the FD-TD data. These are then compared to the results obtained by using the MOM. Additional RCS results for the case of circular metal and dielectric cylinders are also presented. It is shown that a very high degree of correspondence is obtained using this method.

#### \*\*3.3.1 Square Metal Cylinder, Normal (Broadside) Incidence, TM Polarization of Incident Wave

We first consider the example of the scattering of a plane wave by a square conducting cylinder. The cylinder has the electrical size  $k_0 s = 2$ , where  $s$  is the width of the side of the cylinder. The plane-wave excitation

<sup>1</sup>The numerical results were obtained using the FD-TD computer program listed in Appendix A. Standard Fortran is used for this program.

is TM polarized, with field components  $E_z^i$  and  $H_x^i$ , and propagates in the +y direction so that it is at normal incidence to one side of the cylinder ( $\phi^i = 0^\circ$ ). An 84-point MOM solution of Equation (18a) is used as the benchmark for comparison with all FD-TD results, with pulse current expansion and point matching [21, 22].

For the FD-TD analysis, the square cylinder is embedded in a two-dimensional lattice as shown in Figure 4. Each side of the cylinder spans 20 lattice-cell divisions. The connecting virtual surface between the FD-TD total-field and scattered-field regions is located at a uniform distance of 5 cells from the cylinder surface. Figure 20 shows the geometry of the square cylinder, the incident plane wave, and the loci  $\overline{abcd}$  (cylinder surface) and  $\overline{ABCD}$  (off-surface, near-scattered field) along which comparative FD-TD and MOM results will be graphed.

Figures 21a and 21b graph the comparative results for the FD-TD and MOM analyses of the magnitude and phase of the cylinder surface electric current distribution for this case. Here, the FD-TD computed surface current is taken as  $\hat{n} \times \vec{H}_{\text{tan}}$ , where  $\hat{n}$  is the unit normal vector at the cylinder surface, and  $\vec{H}_{\text{tan}}$  is the FD-TD value of the magnetic field parallel to the cylinder surface, but at a distance of 0.5 space cell from the surface. (The displacement of the H component from the cylinder surface is a consequence of the spatially-interleaved nature of the E and H components of the FD-TD lattice, indicated in Figure 2). In Figure 21a, the magnitude of the FD-TD computed surface current agrees with the 84-point MOM solution to better than  $\pm 1\%$  (0.09 dB) at all comparison points more than 2 cells from the cylinder edges (current singularities). In Figure 21b, the phase of the FD-TD solution agrees with the MOM solution to within  $\pm 3^\circ$  at all comparison points, including the shadow region. The uncertainty bars shown in this figure indicate the present level of imprecision in using the FD-TD method to locate the constant-phase points of the computed time-domain  $\vec{H}_{\text{tan}}$  waveform (equivalent to  $\pm 1$  time step). This imprecision can be reduced in future FD-TD programs by incorporating a simple interpolation algorithm to achieve fractional time-step resolution of points of constant phase.

Figures 22a, 22b, 23a and 23b show the comparison of the magnitude and

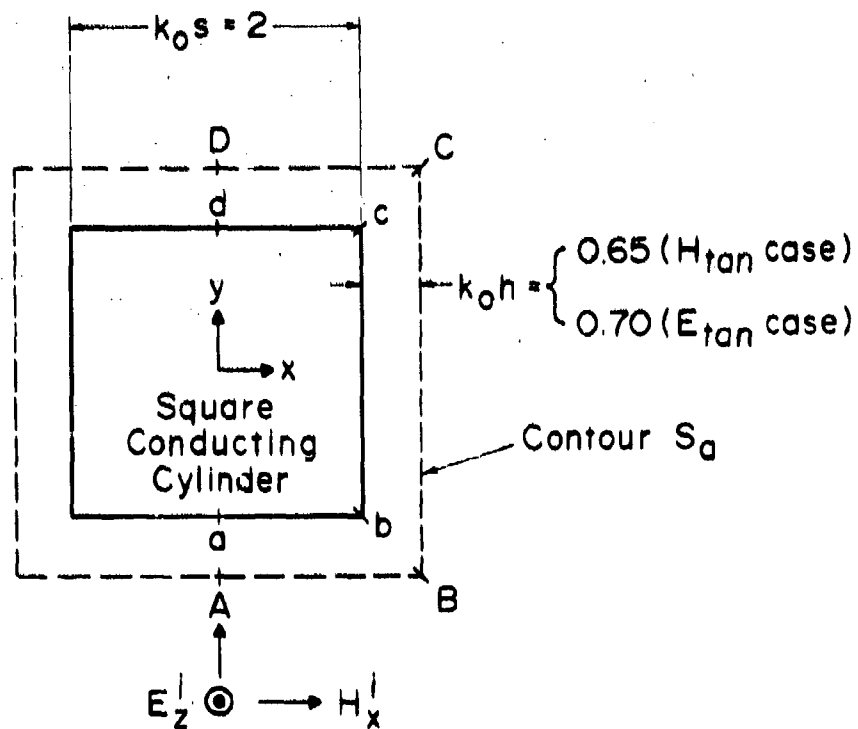


Fig. 20. GEOMETRY FOR TWO-DIMENSIONAL SCATTERING  
EXAMPLE: SQUARE CONDUCTING CYLINDER  
ILLUMINATED BY A PLANE WAVE AT NORMAL  
INCIDENCE ( $\phi = 0^\circ$ )



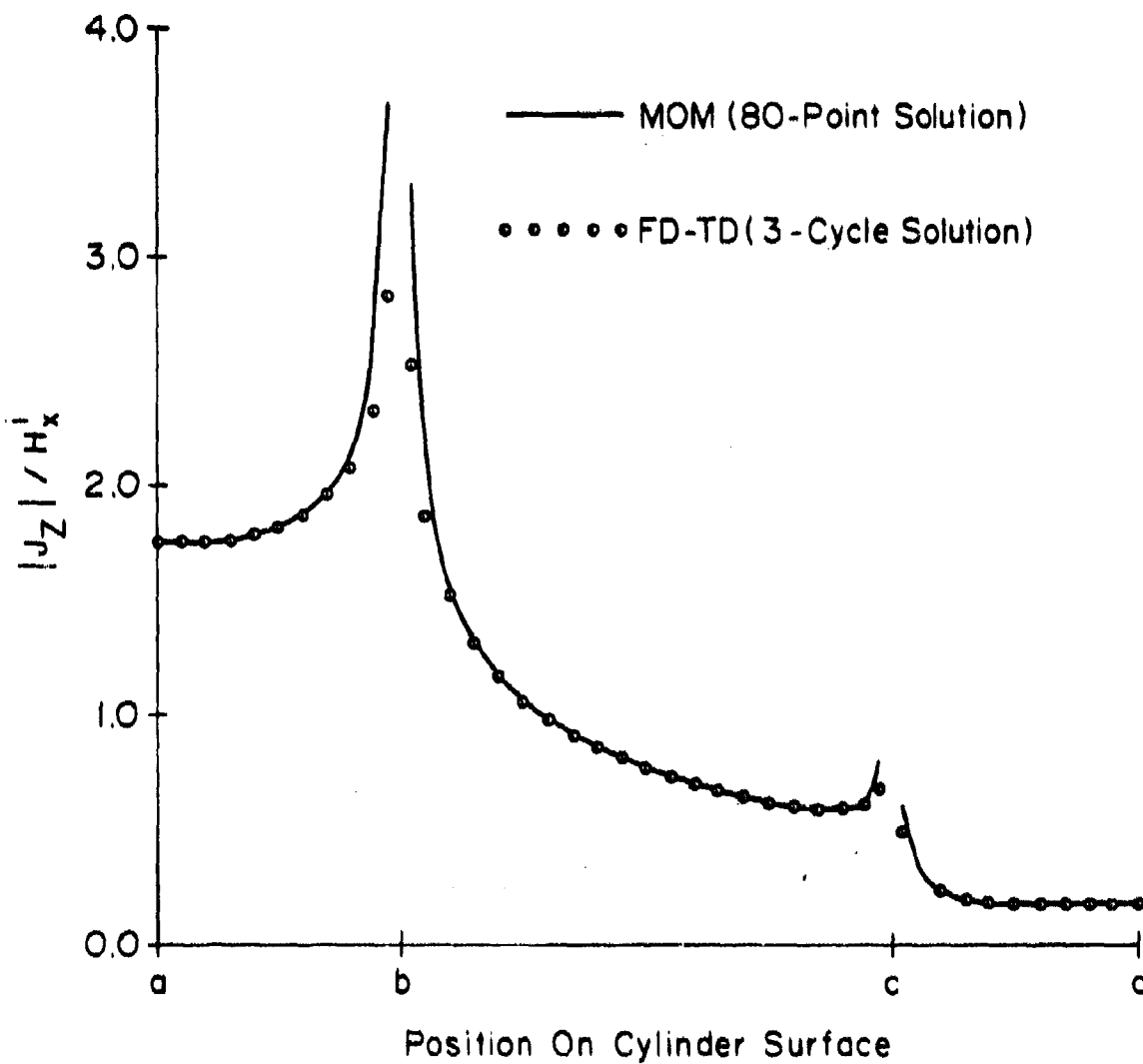


Fig. 21a. COMPARISON OF MOM AND FD-TD RESULTS FOR MAGNITUDE OF ELECTRIC CURRENTS ON SURFACE OF CYLINDER.

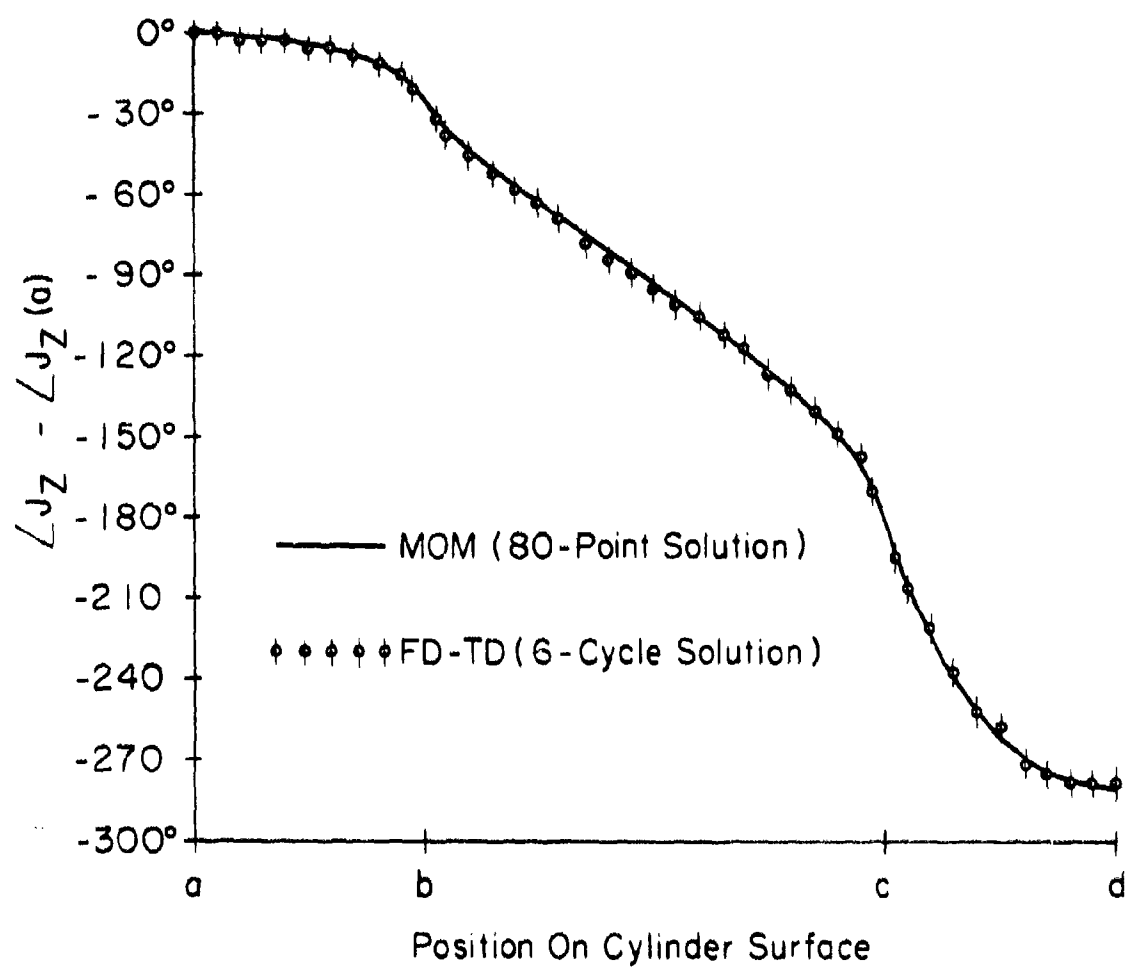


Fig. 21b. COMPARISON OF MOM AND FD-TD RESULTS FOR PHASE OF ELECTRIC CURRENTS ON SURFACE OF CYLINDER

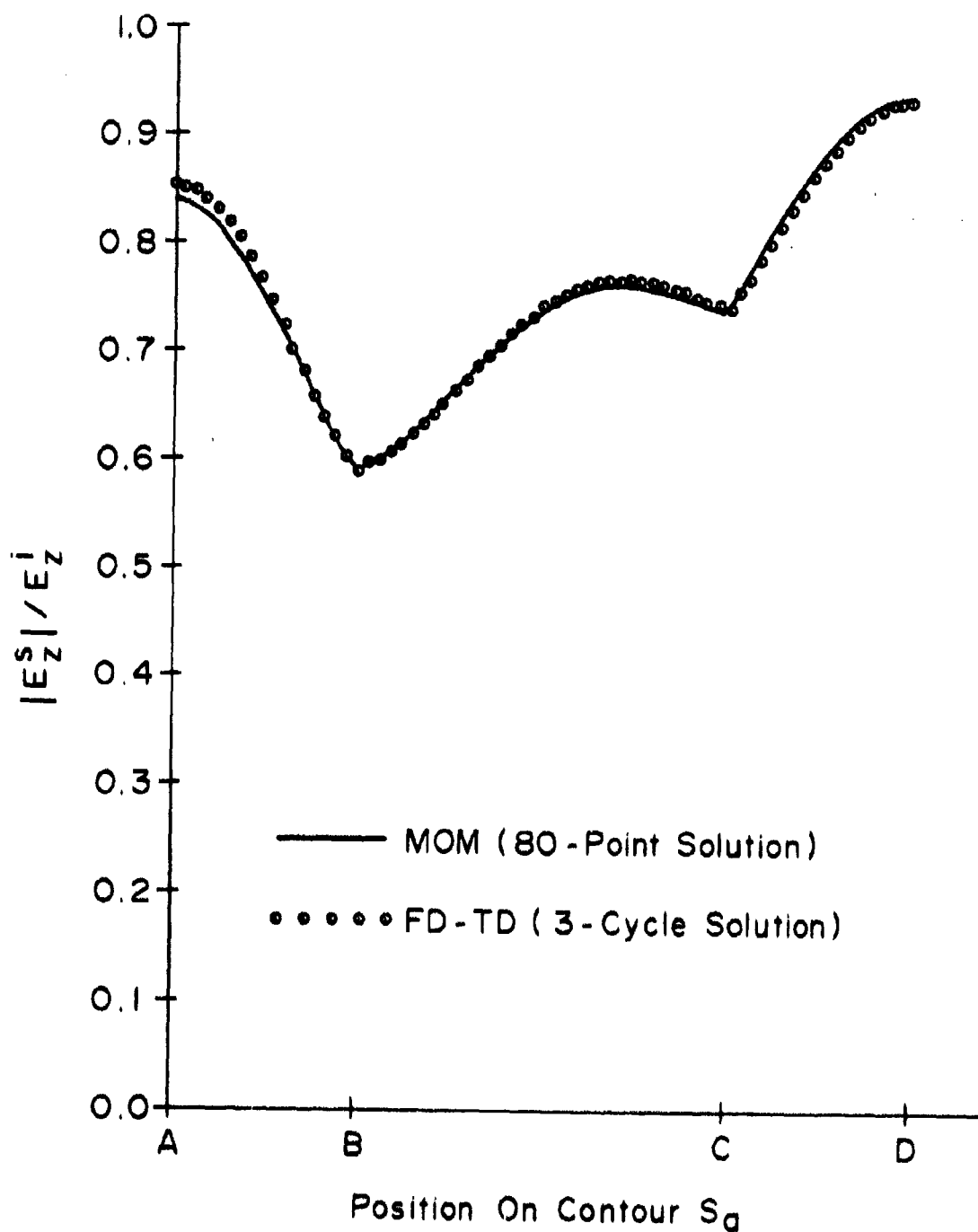


Fig. 22a. COMPARISON OF MOM AND FD-TD RESULTS FOR NEAR ELECTRIC FIELD TANGENTIAL TO CONTOURS  $S_0$

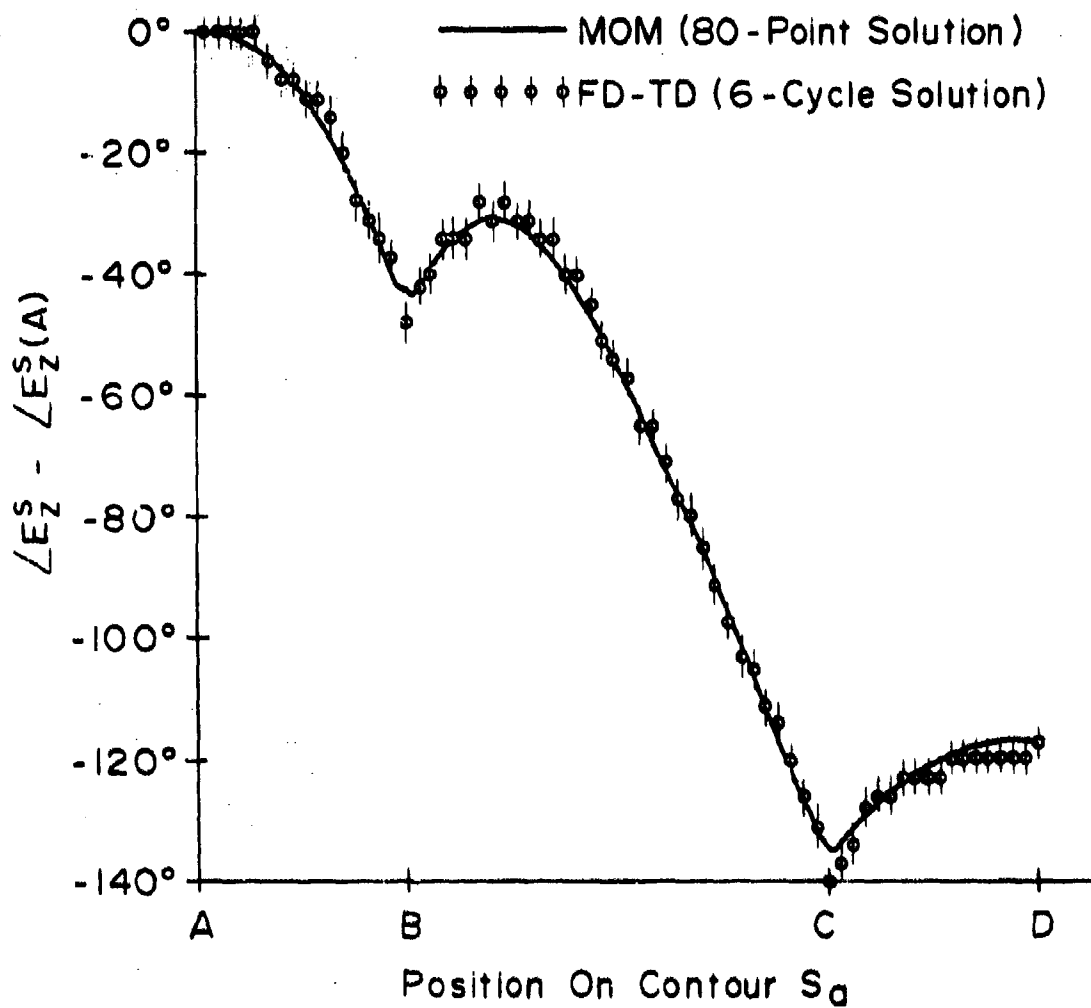


Fig. 22b. COMPARISON OF MOM AND FD-TD RESULTS  
FOR PHASE OF NEAR ELECTRIC FIELD  
TANGENTIAL TO CONTOUR  $S_d$

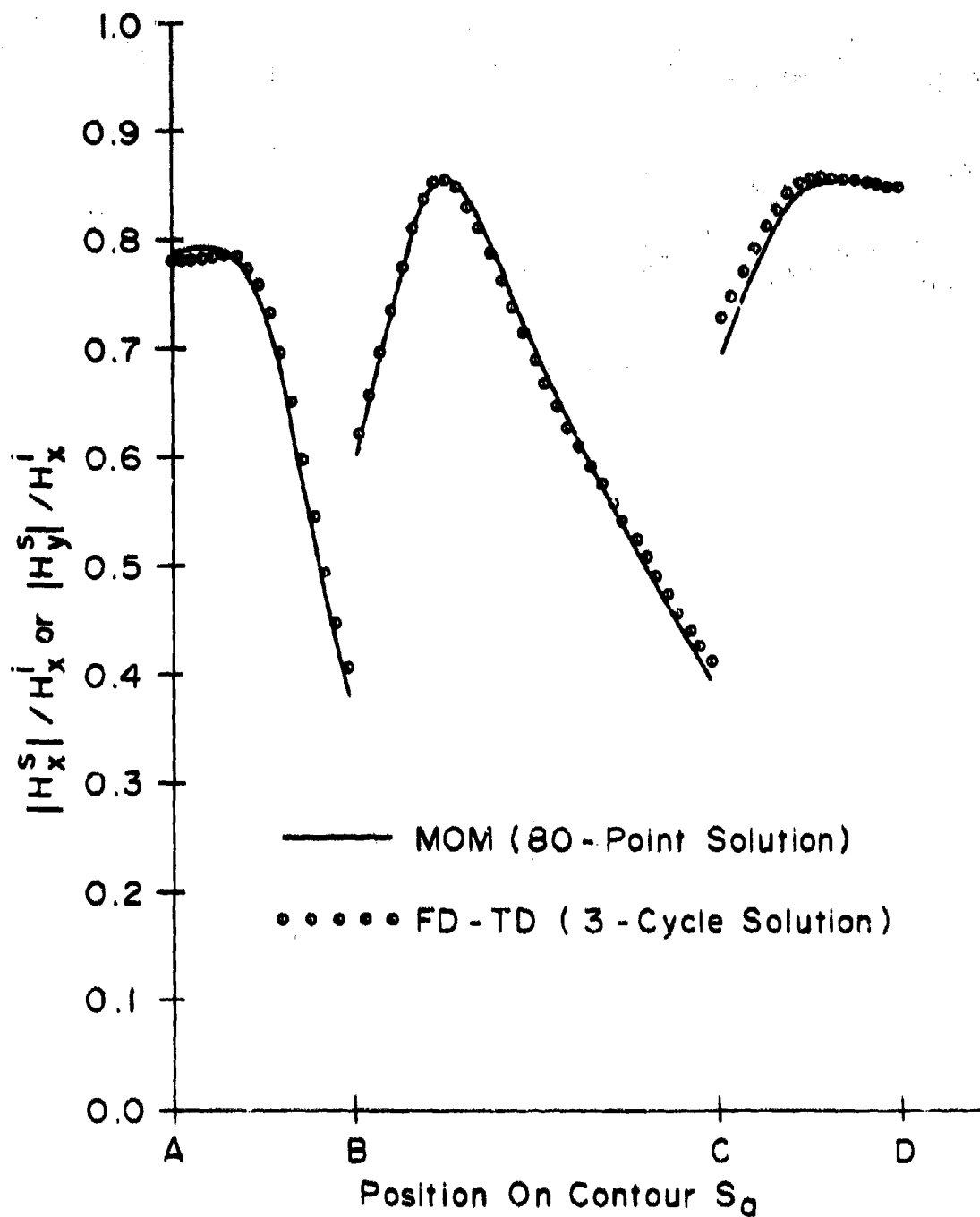


Fig. 23a. COMPARISON OF MOM AND FD-TD RESULTS FOR NEAR MAGNETIC FIELD TANGENTIAL TO CONTOURS  $S_0$

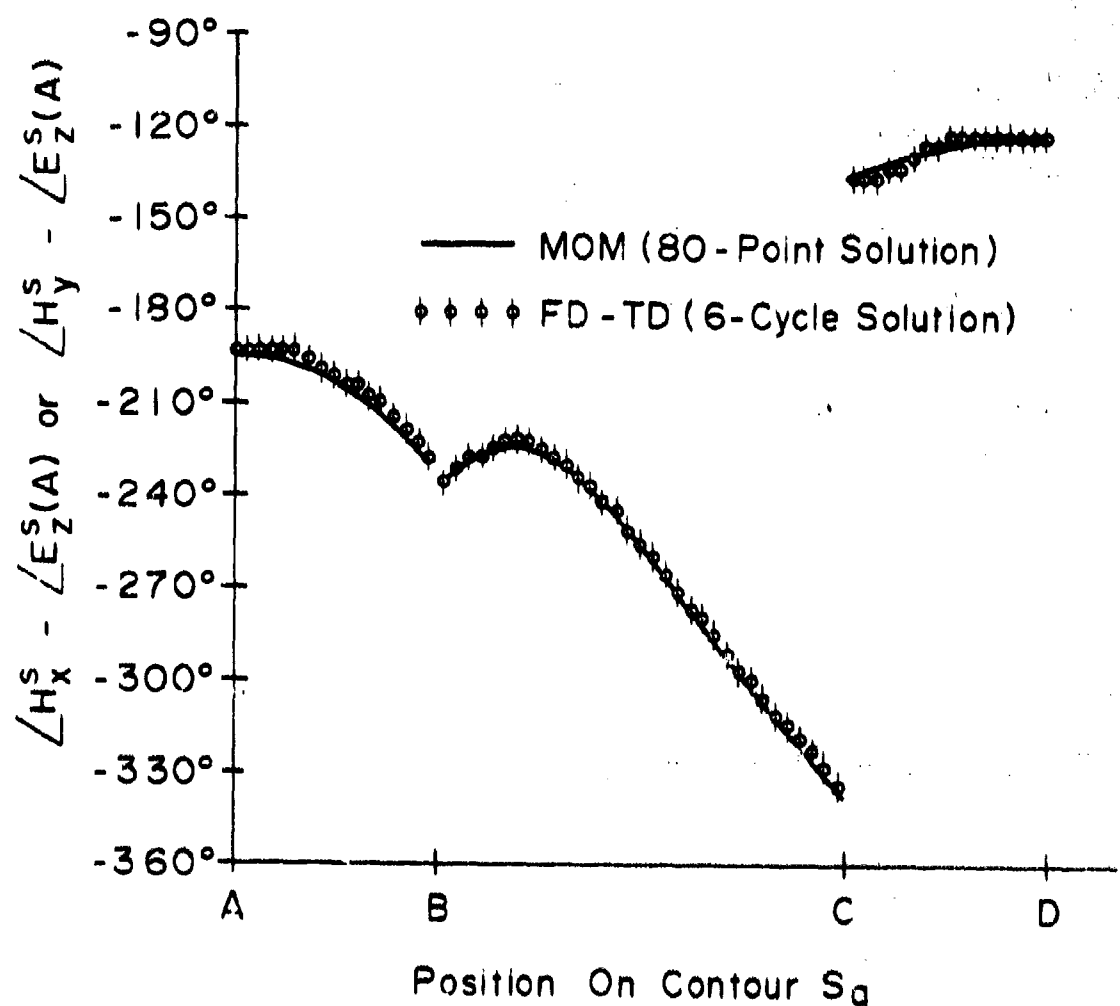


Fig. 23b. COMPARISON OF MOM AND FD-TD RESULTS FOR PHASE OF NEAR MAGNETIC FIELDS TANGENTIAL TO CONTOUR  $S_0$

phase of the near scattered electric and magnetic fields computed by the FD-TD method and MOM. The electric field is tangential to a virtual surface,  $S_a$ , located at a uniform distance of  $h = 7$  space cells from the cylinder surface; and the magnetic field is tangential to a virtual surface,  $S'_a$ , located at 6.5 cells from the cylinder surface. Both virtual surfaces are embedded in the scattered-field region of the FD-TD lattice. The level of correspondence between the FD-TD and MOM results is  $\pm 2.5\%$  ( $\pm 0.2$  dB) and  $\pm 3^\circ$ .

In order to obtain the far-field pattern and the scattering cross-section, the near-field to far-field transformation discussed in Section 2.2.5 is followed for two-dimensional structures. The near scattered fields shown in Figures 22a, 22b, 23a and 23b are converted into the corresponding equivalent electric and magnetic current distributions along  $S_a$  according to Equations (14a) and (14b). The far field is then computed by applying Equations (17a) - (17e).

Figure 24 plots the normalized radar cross section (RCS) versus scattering angle,  $\phi$ , for the square, conducting cylinder. Two cases are plotted. First, the solid curve represents the RCS computed directly from the induced surface electric currents of the cylinder. These surface currents were derived via a MOM solution of Equation (18), and the far field derived by performing the integration of Equation (19). Second, the dots represent RCS values computed by converting the FD-TD derived near electric and magnetic fields of Figures 22a, 22b, 23a, 23b to the far field by applying Equations (14a), (14b), and (17a) - (17e). A very high degree of correspondence is indicated between the two sets of results. This correspondence indicates the validity of the hybrid FD-TD method for computing the far field and radar cross section, as well as the accuracy of the new FD-TD algorithm provisions.

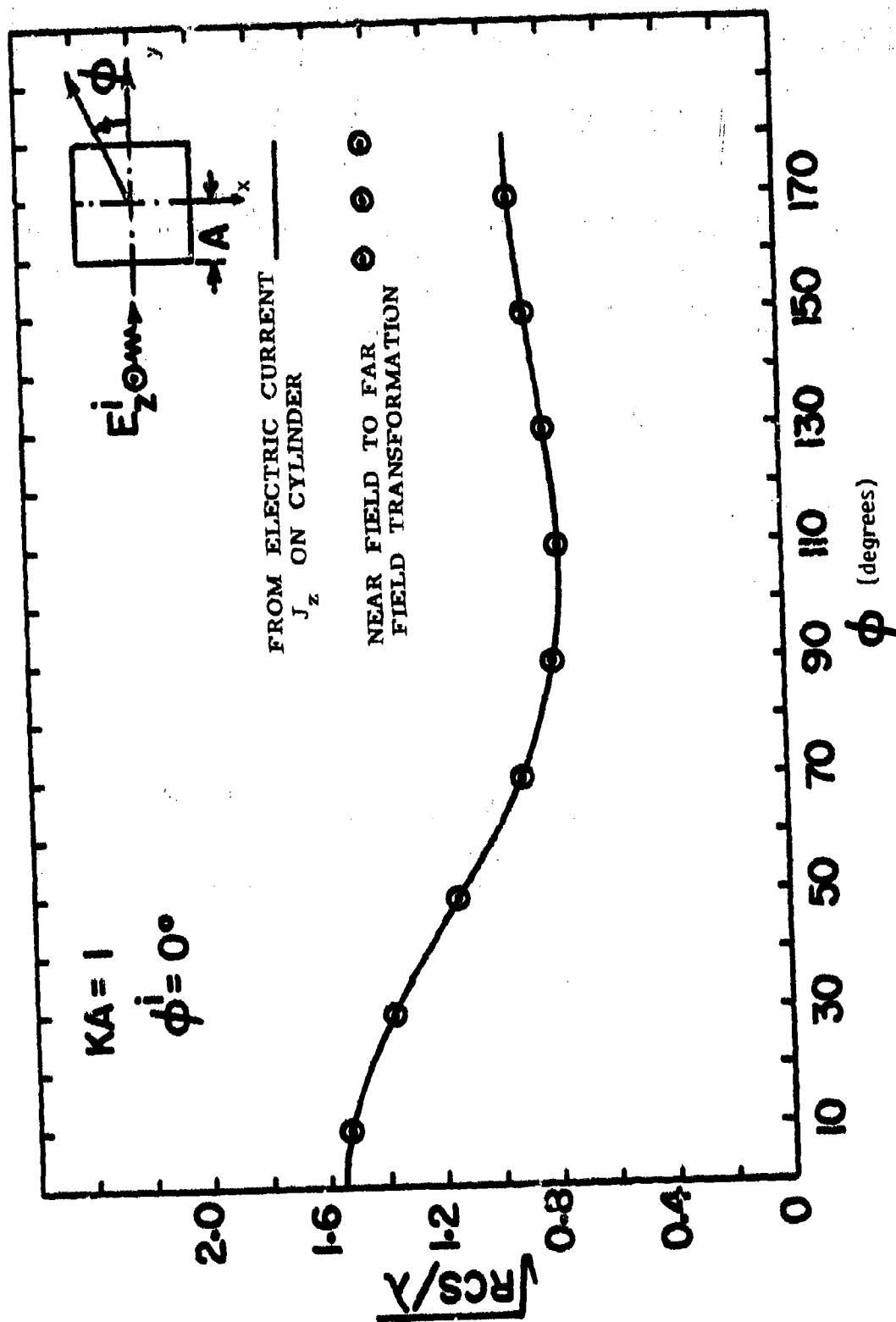


Figure 24. EQUIVALENCE OF COMPUTED RESULTS FOR RADAR CROSS SECTION OBTAINED USING THE MOW SURFACE CURRENTS APPROACH AND THE HYBRID FD-TO NEAR-TO-FAR FIELD TRANSFORMATION TECHNIQUE



### **\*\*3.3.2 Square Metal Cylinder, Oblique (45°) Incidence, TM Polarization of Incident Wave**

We next consider the oblique illumination of the square metal cylinder of the previous example. Figure 25 shows the geometry of the square cylinder, the incident plane wave, and the loci  $\overline{abc}$  (cylinder surface) and  $\overline{ABC}$  (off-surface, near-scattered field) along which comparative FD-TD and MOM results will be graphed. The only change made from the previous scattering example is that the incident wave is assumed to propagate at an angle of 45° relative to one side of the cylinder ( $\phi^i = 45^\circ$ ). This change is made simply by altering one data statement of the Fortran computer program.

Figures 26a and 26b graph the comparative results for the FD-TD and MOM analyses of the magnitude and phase of the cylinder surface electric current distribution for this case. Again, the FD-TD computed surface current is taken as  $\hat{n} \times \hat{H}_{\text{tan}}$ , where  $\hat{n}$  is the unit normal vector at the cylinder surface, and  $\hat{H}_{\text{tan}}$  is the FD-TD value of the magnetic field parallel to the cylinder surface, but at a distance of 0.5 space cell from the surface. In Figure 26a, the magnitude of the FD-TD computed surface current agrees again with the 84-point MOM solution to better than  $\pm 1\%$  ( $\pm 0.09$  dB) at all comparison points more than 2 cells from the cylinder edges (current singularities). In Figure 26b, the phase of the FD-TD solution again agrees with the MOM solution to within  $\pm 3^\circ$  at virtually each comparison point, including the shadow region.

Figure 27a, 27b, 28a, and 28b show the comparison of the magnitude and phase of the near-scattered electric and magnetic fields computed by the FD-TD method and MOM. Again, the electric field is tangential to a virtual surface,  $S_a$ , located at a uniform distance of  $h = 7$  space cells from the cylinder surface; and the magnetic field is tangential to a virtual surface,  $S'_a$ , located at 6.5 cells from the cylinder surface. The level of correspondence between the FD-TD and MOM results is again  $\pm 2.5\%$  ( $\pm 0.2$  dB) and  $\pm 3^\circ$ .

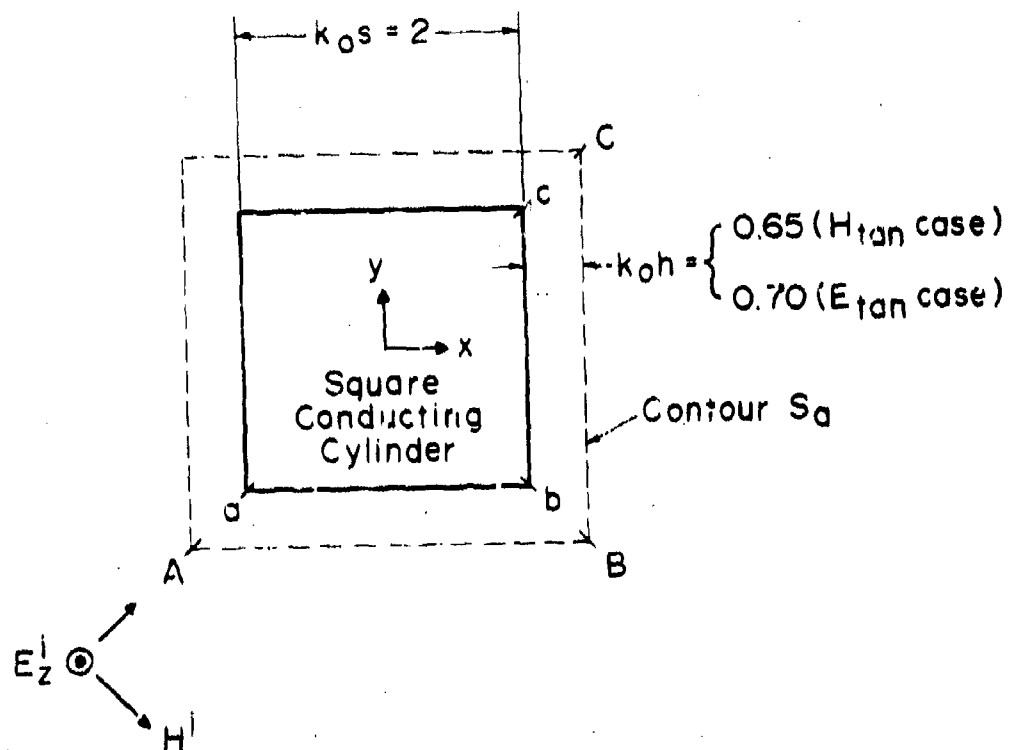


Fig. 25. GEOMETRY FOR TWO-DIMENSIONAL SCATTERING  
EXAMPLE: SQUARE CONDUCTING CYLINDER  
ILLUMINATED BY A PLANE WAVE AT OBLIQUE  
INCIDENCE ( $\phi = 45^\circ$ )

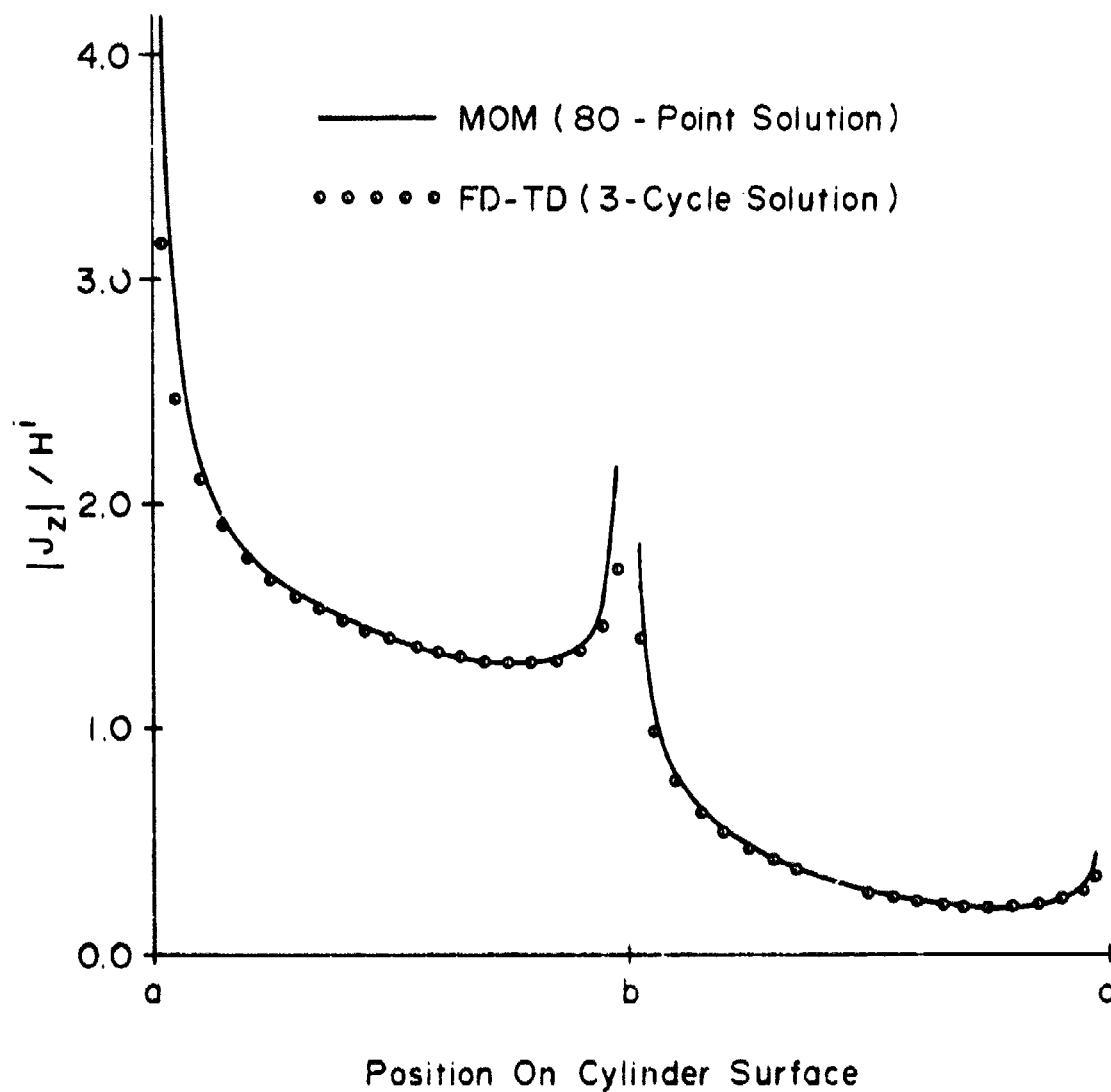


Fig. 26a. COMPARISON OF MOM AND FD-TD RESULTS FOR MAGNITUDE OF ELECTRIC CURRENTS ON SURFACE OF CYLINDER, OBLIQUE INCIDENCE CASE ( $\phi = 45^\circ$ )

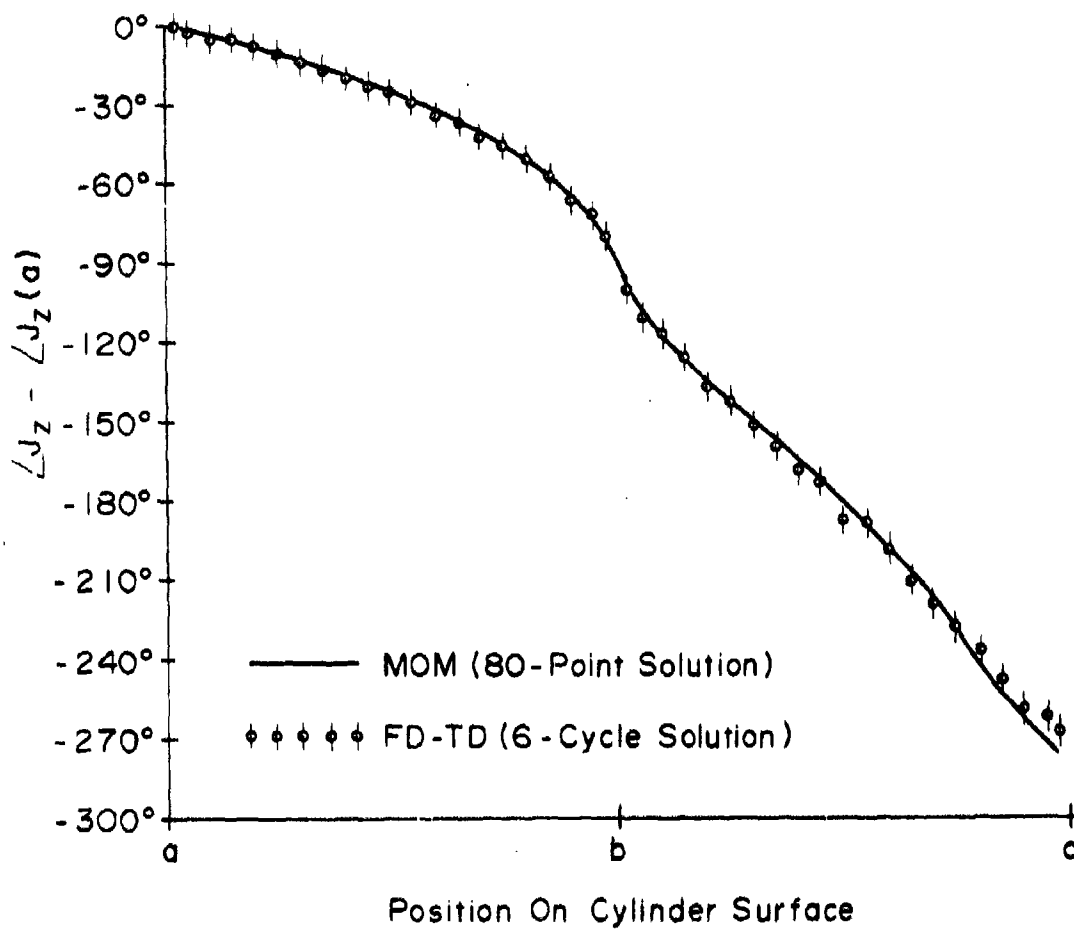


Fig. 26b. COMPARISON OF MOM AND FD-TD RESULTS FOR PHASE OF ELECTRIC CURRENTS ON SURFACE OF CYLINDER, OBLIQUE INCIDENCE CASE ( $\phi = 45^\circ$ )

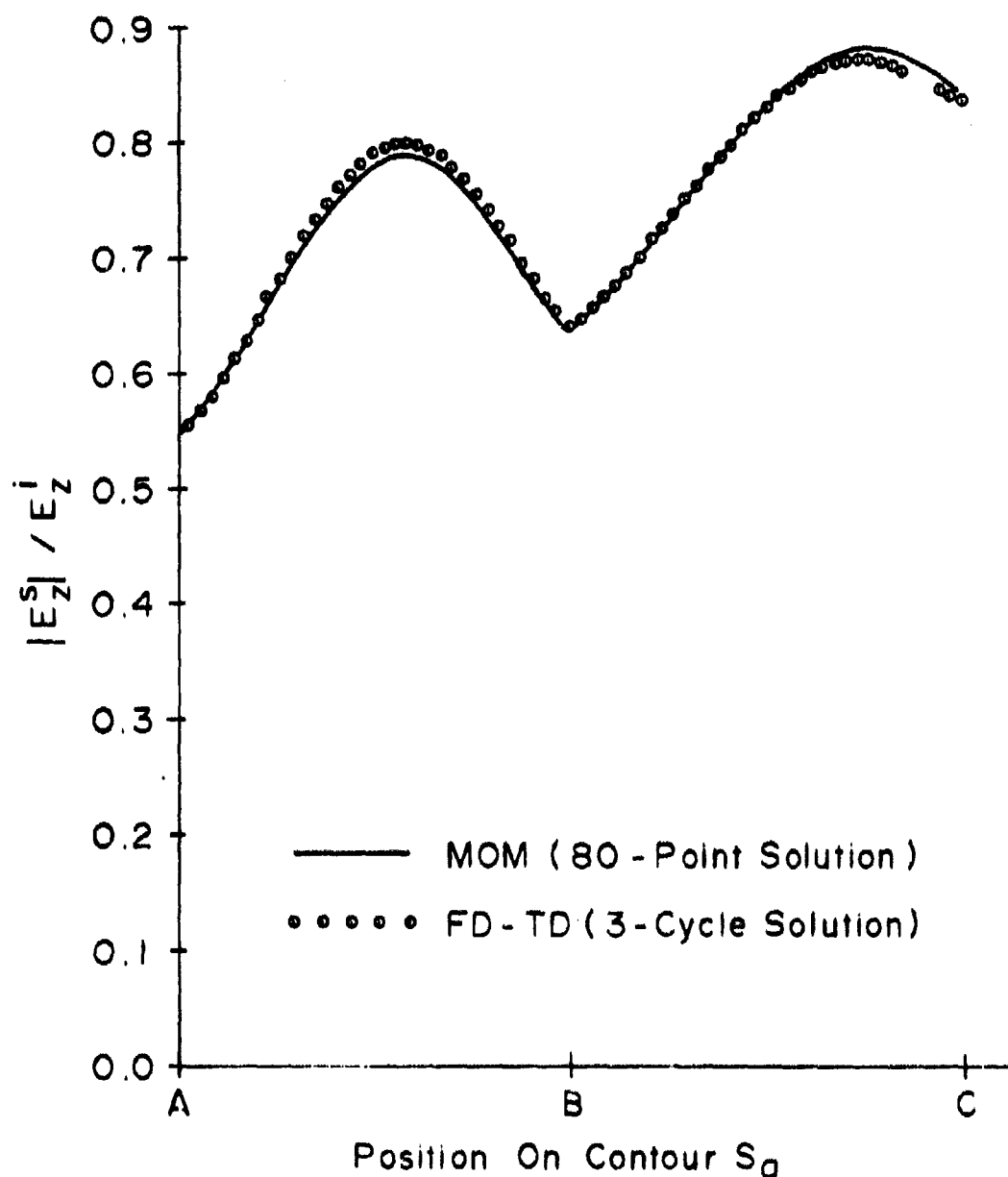


Fig. 27a. COMPARISON OF MOM AND FD-TD RESULTS FOR NEAR ELECTRIC FIELD TANGENTIAL TO CONTOUR  $S_0$  FOR OBLIQUE INCIDENCE CASE ( $\phi = 45^\circ$ )

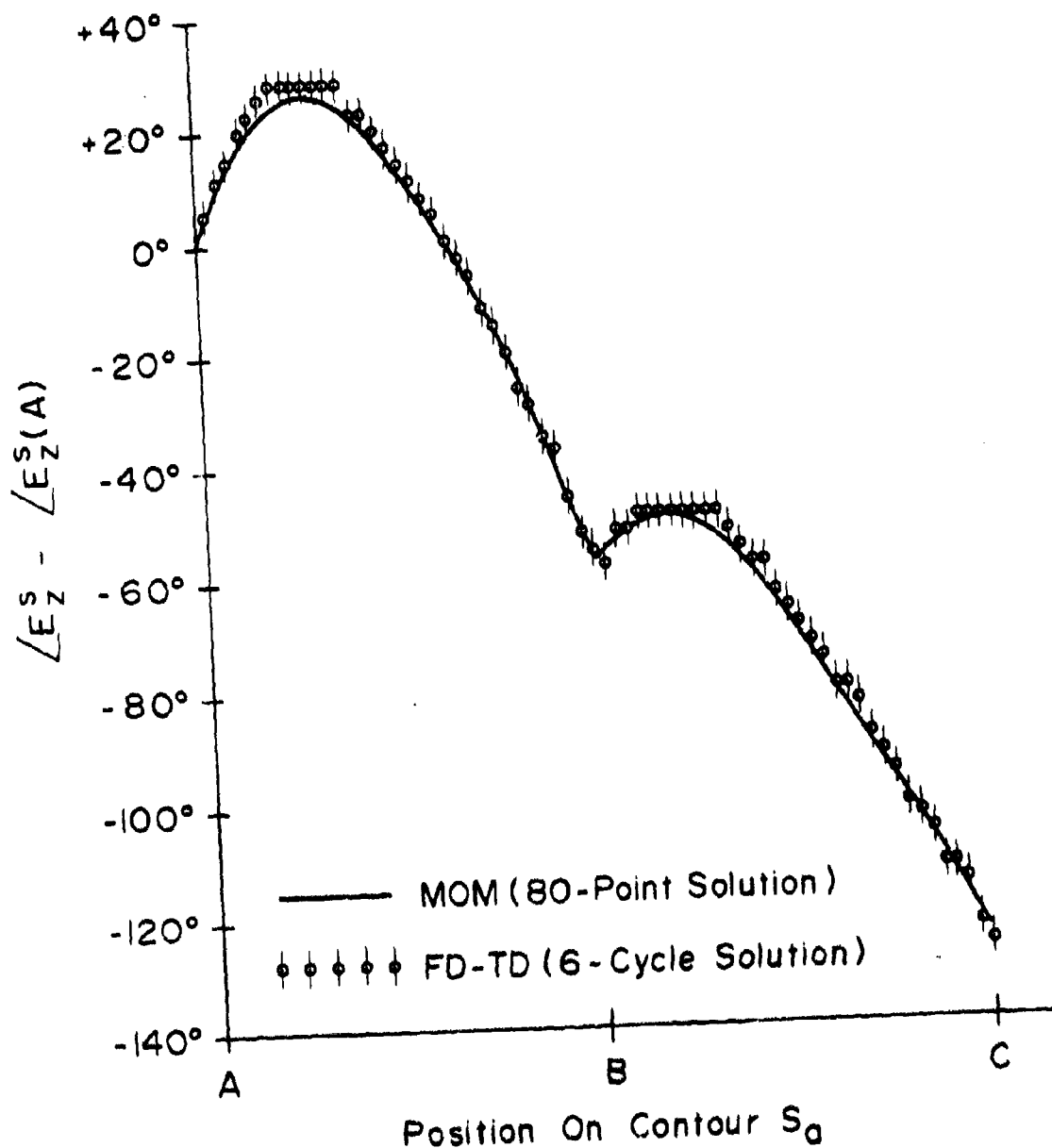


Fig. 27b. COMPARISON OF MOM AND FD-TD RESULTS FOR PHASE OF NEAR ELECTRIC FIELD TANGENTIAL TO CONTOUR  $S_0$  FOR OBLIQUE INCIDENCE CASE ( $\phi = 45^\circ$ )

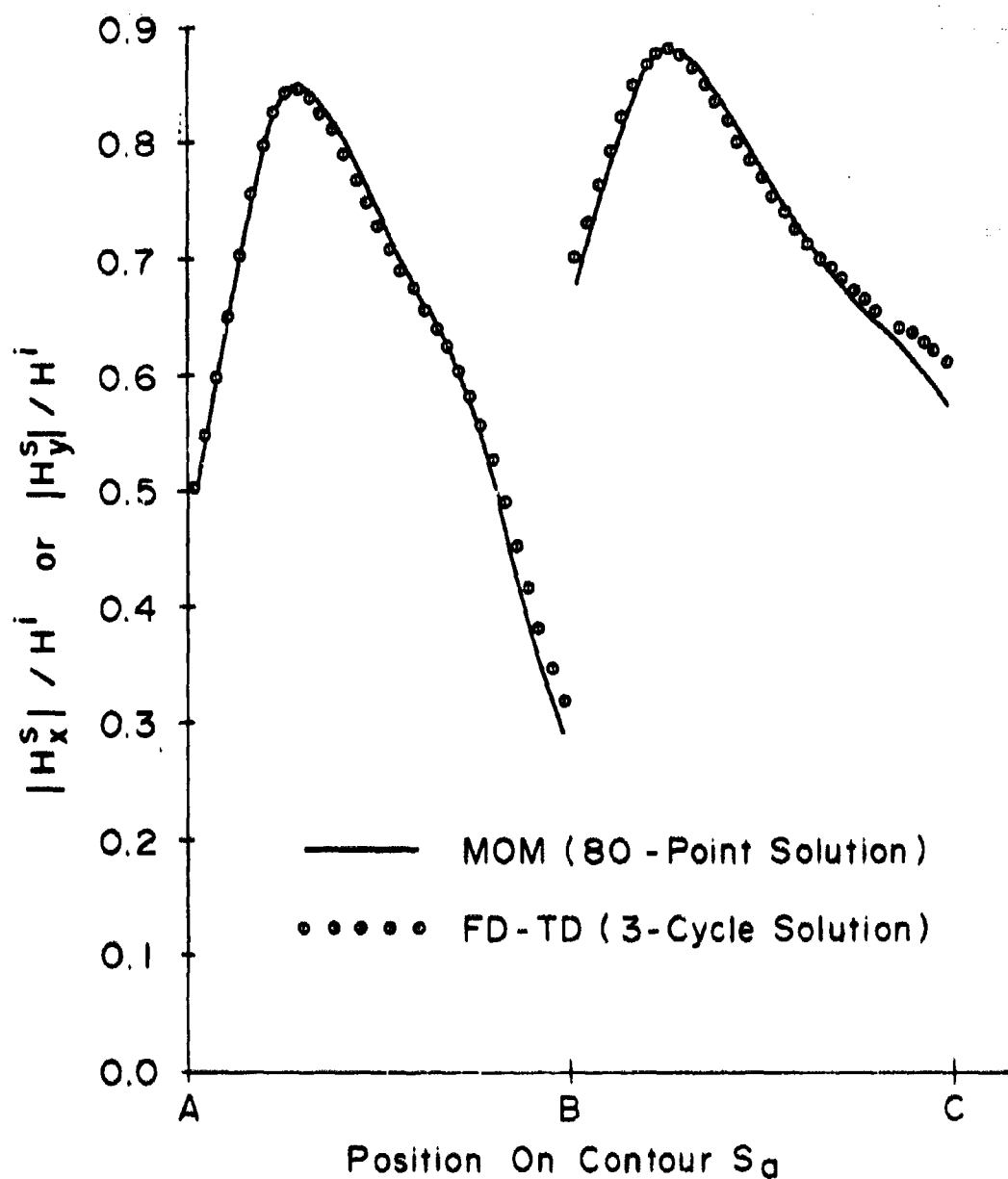


Fig. 28a. COMPARISON OF MOM AND FD-TD RESULTS FOR NEAR MAGNETIC FIELD TANGENTIAL TO CONTOUR  $S_a$  FOR OBLIQUE INCIDENCE CASE ( $\phi = 45^\circ$ )

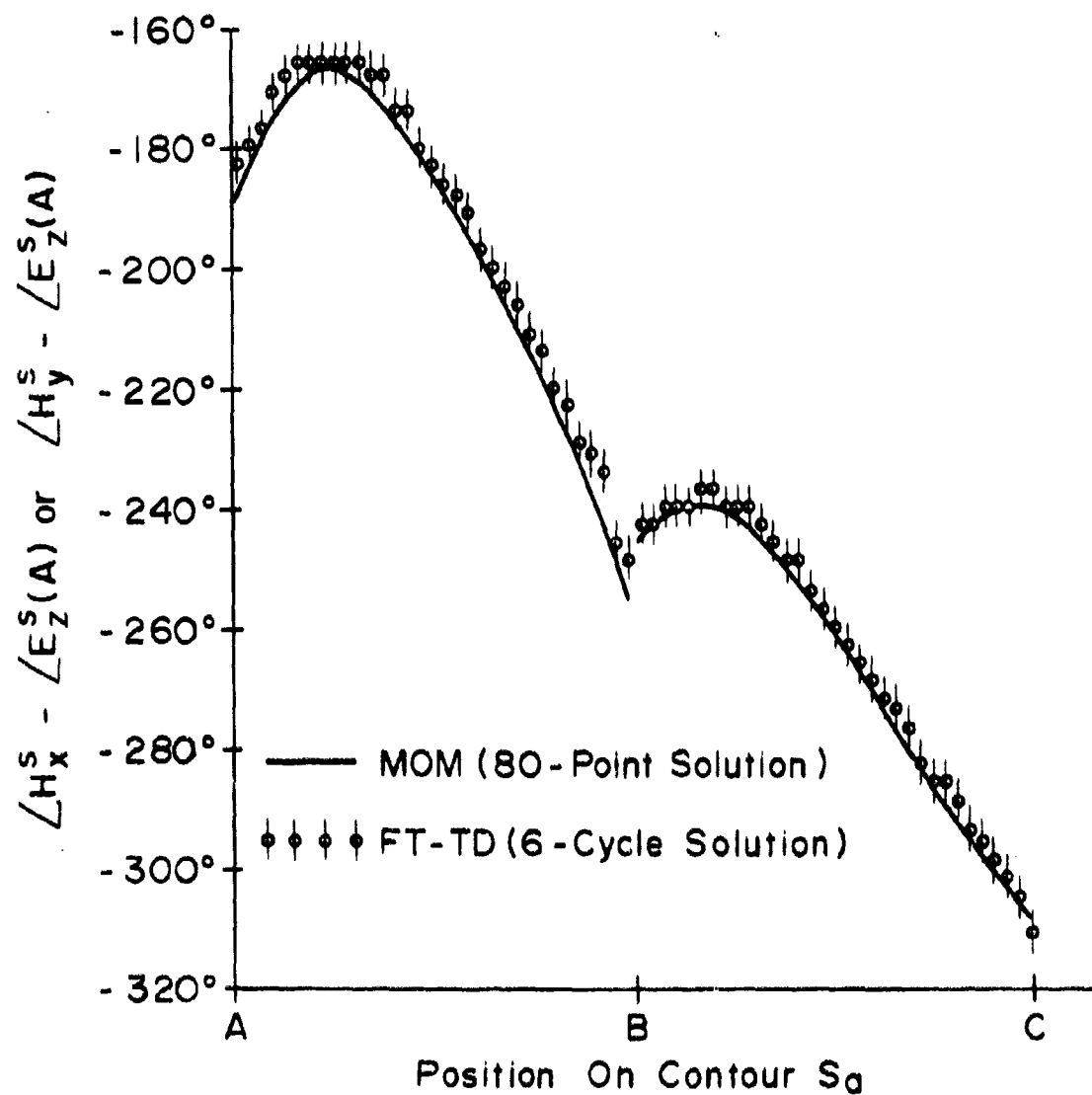


Fig. 28b. COMPARISON OF MOM AND FD-TD RESULTS FOR PHASE OF NEAR MAGNETIC FIELD TANGENTIAL TO CONTOUR  $S_0$  FOR OBLIQUE INCIDENCE CASE ( $\phi = 45^\circ$ )



The high level of agreement between the FD-TD and MOM results for both the  $\phi^i = 0^\circ$  and  $\phi^i = 45^\circ$  angles of incidence verifies that the key, new FD-TD features (variable-incidence plane wave, second-order-correct lattice truncations, sinusoidal steady-state magnitude and phase computations) work, and work very well. In fact, the observed level of accuracy for these latest results is as much as 5 to 10 times as good as the previously-observed [12], [13] FD-TD accuracy level of  $\pm 10\%$  ( $\pm 1$  dB). It is expected that the new, enhanced accuracy levels will be observed when the present two-dimensional FD-TD computer programs are modified to the three-dimensional case.

### **\*\*3.3.3 Verification of Near-to-Far Field Transformation for Circular Metal and Dielectric Cylinders**

To provide further verification of the application of the near-to-far field transformation of Section 2.2.5, pure MOM studies have been performed during this research program on a metal and a dielectric circular cylinder. These studies concern the computation of scattering from such cylinders for the two-dimensional case of plane wave illumination (TM polarization).

Figure 29 shows the normalized radar cross section (RCS) computed for a metal cylinder of size  $k_0 a = 1$ . The solid line shows the RCS computed directly from the surface electric current,  $J_z$ , on the cylinder. The dots show the RCS computed using the near-to-far field transformation executed along a square virtual surface located at an electrical distance  $k_0 h = 0.38$  from the surface of the cylinder. The agreement of the two solutions for the RCS is extremely high (to better than 4 decimal places at each point of comparison).

Figure 30 shows the normalized RCS computed for a dielectric cylinder of size  $k_0 a = .63$ . The solid line shows the RCS computed directly from the equivalent electric and magnetic currents on the surface of the cylinder, which had been previously derived using a MOM solution of a surface integral equation. The dots show the RCS computed using the near-to-far field transformation executed along a square virtual surface located at an electrical

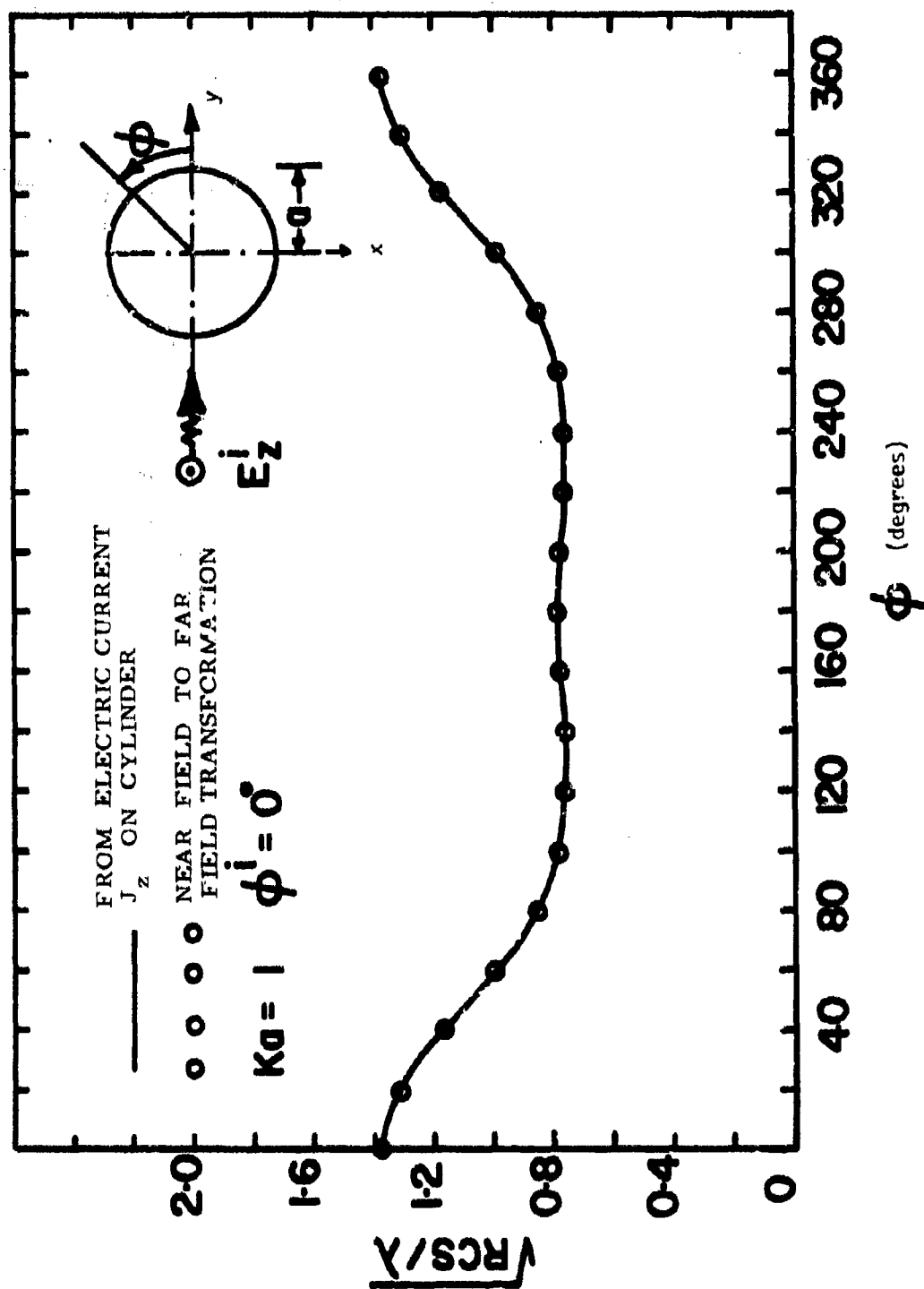


Figure 29. EQUIVALENCE OF COMPUTED RESULTS FOR RADAR CROSS SECTION OBTAINED USING THE MOM SURFACE CURRENTS APPROACH AND THE HYBRID MOM NEAR-TO-FAR FIELD TRANSFORMATION TECHNIQUE

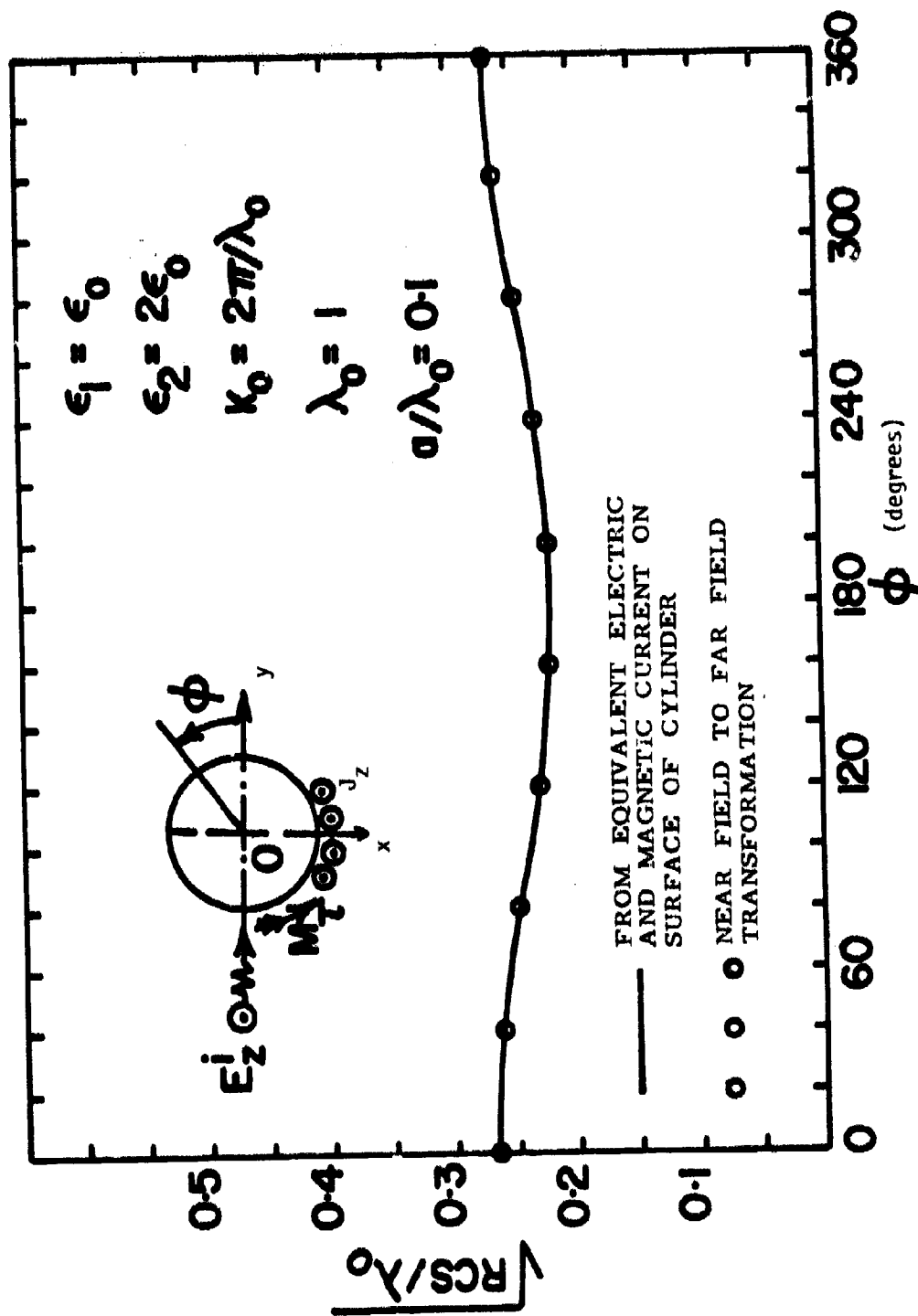


Figure 30. EQUIVALENCE OF COMPUTED RESULTS FOR RADAR CROSS SECTION OBTAINED USING THE MOM SURFACE CURRENTS APPROACH AND THE HYBRID MOM NEAR-TO-FAR FIELD TRANSFORMATION TECHNIQUE

distance  $k_0 h = 0.24$  from the surface of the cylinder. Again, the agreement of the two solutions for the RCS is extremely high (to better than 4 decimal places at each point of comparison).

It is therefore concluded that the application of the near-to-far field transformation along a rectangular locus surrounding a scatterer is, for all practical purposes, an exact procedure for deriving the far fields. The validity of this near-to-far field transformation is the heart of the proposed hybrid FD-TD method for computing the far scattered fields and RCS from arbitrary, extremely-complex structures in three dimensions. It should be noted that this procedure should also be equally valid and useful in computing the far-field radiation patterns of extremely-complex source regions and antennas.

#### 4.0 SUMMARY AND CONCLUSIONS

Electromagnetic penetration and scattering problems are difficult to treat with many analytical or numerical methods because of the inability of these methods to simply deal with the effects of structure materials, apertures, curvatures, corners, and internal contents. In two earlier RADC contracts, IITRI investigated the application of a new approach for the direct modeling of very complex electromagnetic interaction problems: the finite-difference, time-domain (FD-TD) solution of Maxwell's equations. The FD-TD method has key advantages relative to available modeling approaches. These advantages permit it to accurately treat complex problems that are beyond the scope of solution by any other method. The ultimate aim of research in this area is to develop an accurate, easily-used, general computer program solving for either electromagnetic field penetration, scattering, or radiation for arbitrary metal/dielectric structures spanning up to 10 or more wavelengths in three dimensions with a spatial resolution better than 0.1 wavelength.

In order to more fully determine the usefulness of the FD-TD method, RADC thought that it is desirable to distribute this technique to as wide a range of users as possible so that it can be tested by actual implementation. The overall objectives of algorithm development in this case are to allow RADC to write a user-oriented computer program for the FD-TD technique.

The goals of the present IITRI research effort for RADC include the development of specific algorithms of high importance to help provide a flexible, simple-to-use, and highly accurate user-oriented FD-TD computer program. To meet these goals, IITRI has tested five key improvements in the FD-TD algorithm during this effort, including the following:

1. Total-field/scattered-field lattice division.

This permits a very high computational dynamic range to accurately model fields within shadow zones or cavities. This further permits programming of variable angle of incidence and the second-order correct radiation condition, summarized below.

2. Variable angle of incidence.

For two-dimensional problems, this permits a single data card or Fortran statement to specify in a very accurate manner the angle of incidence of a plane wave illuminating a structure. For three-dimensional problems, both the angle of incidence and polarization could be specified. There is no requirement to rotate the geometry of the interacting structure in the FD-TD lattice.

3. Second-order accurate radiation condition.

This reduces the uncertainty of the final computed results by as much as ten-to-one. FD-TD computations using this radiation condition now have estimated field-magnitude uncertainties of better than  $\pm 2.5\%$  ( $\pm 0.2$  dB) versus previous uncertainties of  $\pm 10\%$ - $\pm 15\%$  ( $\pm 1$  dB).

4. Magnitude and phase computation condition for the sinusoidal steady state.

This permits accurate determination of the magnitude and phase of FD-TD computed fields at any desired points for later use in computations involving scattering, radiation or coupling to wires. This approach avoids any ambiguity due to either a possible DC offset of the fields or the repetitive nature of the sinusoidal waveform.

5. Near-to-far field transformation.

This permits the far scattered fields and radar cross section of arbitrary structures modeled by the FD-TD method to be easily and accurately determined. Observed accuracy of the radar cross section using this feature is in the order of  $\pm 1\%$  ( $\pm 0.09$  dB).

In addition to the five algorithm improvements tested by IITRI, this report also summarized a FD-TD feature which has recently appeared in the literature that permits computation of the coupling of currents to thin wires and struts.

The conclusions of this report are as follows:

1. The accuracy of the pure FD-TD method for electromagnetic interaction problems can reach the high levels previously attained only by method-of-moments (MOM) approaches when the second-order accurate radiation condition is used in the FD-TD algorithm. The FD-TD method retains its key advantages over MOM in terms of the much larger electrical size and greater complexity of the structures that can be modeled.
2. The specification of variable angle of incidence and polarization of an illuminating wave can be achieved with the FD-TD method using only a single data card or Fortran statement.<sup>1</sup>
3. The total-field/scattered-field regional division of the FD-TD lattice can be successfully implemented and offers the significant advantage of a high computational dynamic range. In addition, this lattice division provides a framework for programming variable wave incidence and polarization, improved radiation conditions, and the near-field to far-field transformation for scattering problems.
4. The near-to-far field transformation along a rectangular virtual surface surrounding a scatterer makes it possible to use the FD-TD method to compute the far scattered fields and radar cross section of complex, arbitrary structures with great precision.

It is the opinion of the authors of this report that the FD-TD method deserves additional investigation to probe just what are the limits of application of this extremely promising approach to accurately model electromagnetic penetration, scattering, and radiation problems.

---

<sup>1</sup>This incident wave specification is now as simple for the FD-TD method as it has been with MOM. However, the FD-TD approach requires re-running the entire problem for each new incident wave angle. With MOM, only a single inversion of the system matrix is required. Subsequently, arbitrary wave excitation is treated as a simple matrix multiplication of the equivalent excitation vector. MOM therefore permits a conceptually simpler treatment of the variable wave incidence problem.

## REFERENCES

- [1] K.S. Yee, "Numerical Solution of Initial Boundary Value Problems Involving Maxwell's Equations in Isotropic Media," IEEE Trans. Antennas Prop., Volume AP-14, May 1966, pp. 302-307.
- [2] E.K. Miller and A.J. Poggio, "Moment-Method Techniques in Electromagnetics from an Application Viewpoint," Chapter 9 in Electromagnetic Scattering, P.L.E. Uslenghi, ed., Academic Press, New York, 1978.
- [3] C.D. Taylor, D.H. Lam, and T.H. Shumpert, "Electromagnetic Pulse Scattering in Time-Varying Inhomogeneous Media," IEEE Trans. Antenna Prop., Volume AP-17, September 1969, pp. 585-589.
- [4] D.E. Merewether, "Transient Currents Induced on a Metallic Body of Revolution by an Electromagnetic Pulse," IEEE Trans. Electromagnetic Compatibility, Volume EMC-13, May 1971, pp. 41-44.
- [5] R. Holland, "Threde: A Free-Field EMP Coupling and Scattering Code," IEEE Trans. Nuclear Science, Vol. NS-24, December 1977, pp. 2416-2421.
- [6] K.S. Kunz and K.M. Lee, "A Three-Dimensional Finite-Difference Solution of the External Response of an Aircraft to a Complex Transient EM Environment: Part I - The Method and its Implementation," IEEE Trans. Electromagnetic Compatibility, Volume EMC-20, May 1978, pp. 328-333.
- [7] R. Holland, L. Simpson, and K.S. Kunz, "Finite-Difference Analysis of EMP Coupling to Lossy Dielectric Structures," IEEE Trans. Electromag. Compat., Vol. EMC-22, August 1980, pp. 203-209.
- [8] R. Holland and L. Simpson, "Finite-Difference Analysis of EMP Coupling to Thin Struts and Wires," IEEE Trans. Electromag. Compat., Vol. EMC-24, May 1981, pp. 88-97.



- [9] A. Taflove and M.E. Brodwin, "Numerical Solution of Steady-State Electromagnetic Scattering Problems Using the Time-Dependent Maxwell's Equations," IEEE Trans. Microwave Theory Tech., Vol. MTT-23, August 1975, pp. 623-630.
- [10] A. Taflove and M.E. Brodwin, "Computation of the Electromagnetic Fields and Induced Temperatures Within a Model of the Microwave-Irradiated Human Eye," IEEE Trans. Microwave Theory Tech., Vol. MTT-23, November 1975, pp. 888-896.
- [11] A. Taflove, "Application of the Finite-Difference Time-Domain Method to Sinusoidal Steady-State Electromagnetic-Penetration Problems," IEEE Trans. Electromagnetic Compatibility, Volume EMC-22, August 1980, pp. 191-202.
- [12] A. Taflove, "Time Domain Solutions for Electromagnetic Coupling," Final Report RADC-TR-78-142, Contract No. F30602-77-C-0163, Rome Air Development Center, Griffiss AFB, Rome, New York, with IIT Research Institute, Chicago, IL, June 1978, A056728.
- [13] A. Taflove, "Evaluation of Time Domain Electromagnetic Coupling Techniques," Final Report RADC-TR-80-251 by IIT Research Institute, Chicago, IL to Rome Air Development Center, Griffiss AFB, New York, on Contract F30602-79-C-0039, 1980, Vol 1 - A092031, Vol 11 - A092032.
- [14] A. Taflove and K.R. Umashankar, "A Hybrid FD-TD Approach to Electromagnetic Wave Backscattering", 1981 URSI/APS International Symposium, Los Angeles, California, June 1981.
- [15] A. Taflove and K.R. Umashankar, "Solution of Complex Electromagnetic Penetration and Scattering Problems in Unbounded Regions", (Invited Paper), Proceedings of Winter Annual Meeting, American Society of Mechanical Engineers, November 1981.

- [16] G. Mur, "Absorbing Boundary Conditions for the Finite-Difference Approximation of the Time-Domain Electromagnetic-Field Equations", paper accepted for publication in IEEE Trans. Electromagnetic Compatibility, 1981.
- [17] J. Van Bladel, Electromagnetic Fields, McGraw-Hill, New York, 1964.
- [18] B. Engquist and A. Majda, "Absorbing Boundary Conditions for the Numerical Simulation of Waves," Math. Comp., Vol. 31, July 1977, pp. 629-651.
- [19] G.A. Kriegsmann and C.S. Morawetz, "Solving the Helmholtz Equation for Exterior Problems with Variable Index of Refraction: I," SIAM J. Sci. Stat. Comput., Volume 1, September 1980. pp. 371-385.
- [20] S.A. Schelkunoff, "Field Equivalence Theorems," Comm. Pure Appl. Math., Vol. 4, 43-59, June 1951.
- [21] R.F. Harrington, Field Computation by Moment Methods, MacMillan, New York 1968.
- [22] K.K. Mei and J. Van Bladel, "Scattering by Perfectly Conducting Rectangular Cylinders", IEEE Trans. on Antennas and Propagation, Vol. AP-11, No. 2, pp. 185-192, March 1963.
- [23] K.R. Umashankar and C.E. Baum, "Transient Electromagnetic Characterization of Arbitrary Conducting Bodies Through an Aperture - Perforated Conducting Screen," Interaction Note 343, March 1978, Air Force Weapons Lab. Albuquerque, NM.
- [24] C.E. Baum, "EMP Simulators for Various Types of Nuclear EMP Environments: An Interim Categorization," Sensor and Simulation Note 151, July 1972, Air Force Weapons Lab, Albuquerque, NM.

- [25] C.J. Bouwkamp, "Theoretical and Numerical Treatment of Diffraction Through a Circular Aperture," IEEE Trans. Antennas Prop., Vol. AP-18, March 1970.
- [26] K.R. Umashankar and C.M. Butler, "A Numerical Solution Procedure for Small Aperture Integral Equations," Interaction Note 212, July 1974, Air Force Weapons Lab, Albuquerque, NM.
- [27] D.R. Wilton and O.C. Dunaway, "Electromagnetic Penetration Through Apertures of Arbitrary Shape: Formulation and Numerical Solution Procedure," Interaction Note 214, July 1974, Air Force Weapons Lab, Albuquerque, NM.
- [28] D.R. Wilton, C.M. Butler, and K.R. Umashankar, "Penetration of Electromagnetic Fields Through Small Apertures in Planar Screens: Selected Data," Interaction Note 213, September 1974, Air Force Weapons Lab, Albuquerque, NM.
- [29] C.M. Butler and K.R. Umashankar, "Electromagnetic Penetration Through an Aperture in an Infinite Planar Screen Separating Two Half Spaces of Different Electromagnetic Properties," Radio Science, Vol. II, July 1976.
- [30] T.B.A. Senior and G.A. Desjardins, "Field Penetration Into a Spherical Cavity," Interaction Note 142, August 1973, Air Force Weapons Lab, Albuquerque, NM.
- [31] H.K. Schumann and D.E. Warren, "Aperture Coupling in Bodies of Revolution," IEEE Trans. Antennas Prop., Vol. AP-26, November 1978, pp. 778-783.
- [32] C.M. Butler and K.R. Umashankar, "Electromagnetic Excitation of a Wire Through an Aperture Perforated Conducting Screen," IEEE Trans. Antennas Prop., Vol. AP-24, July 1976, pp. 456-462.

- [33] K.R. Umashankar and J.R. Wait, "Electromagnetic Coupling in an Infinite Cable Placed Behind a Slot Perforated Screen, "IEEE Trans. Electromagnetic Compatibility, Vol. EMC-20, August 1978, pp. 406-411.
- [34] A. Taflove and K.R. Umashankar, "A Hybrid Moment Method/Finite Difference Time Domain Approach to Electromagnetic Coupling and Aperture Penetration into Complex Geometries," Chap. 14 in Applications of the Method of Moments to Electromagnetic Fields, B.J. Strait, ed., SCEE Press, Orlando, Florida, 1980.
- [35] A. Taflove and K.R. Umashankar, "A Hybrid Moment Method/Finite Difference Time Domain Approach to Electromagnetic Coupling and Aperture Penetration into Complex Geometries," Paper accepted (July, 1981) for publication in IEEE Antennas Prop.
- [36] S. Ramo, J.R. Whinnery, and T. Van Duzer, Fields and Waves in Communication Electronics, Section 5.13 - 5.18. Wiley, New York, 1965.
- [37] A.W. Glisson and D.R. Wilton, "Simple and Efficient Numerical Techniques for Treating Bodies of Revolution," Report RADC-TR-79-22, Rome Air Development Center, Griffiss Air Force Base, New York, March 1979, A067361.

## APPENDIX A

### Listing of Fortran Computer Program

This appendix contains the listing of the Fortran computer program used to obtain the FD-TD results for the square-cylinder scattering problems of Section 3.3 of this report. This computer program contains all of the new FD-TD algorithms that have been examined during the present research effort, except the thin-wire coupling algorithm of Section 2.2.7.2. This program provides a general treatment of two-dimensional penetration and scattering problems for the transverse magnetic (TM) polarization case, and utilizes a 50 x 49-cell Yee grid. The following is a succinct description of the user inputs to this program.

<u>Program Line</u>	<u>Symbol or Data Input</u>	<u>Function</u>
004	FREQ	Illumination frequency (Hz)
005	DX	Lattice cell size (meters)
006	NCYCS	Number of complete cycles of the sinusoidal incident wave that the program is time-stepped
007	MEDIA	Equal to 2 + number of distinct dielectric or conducting materials modeled in the FD-TD grid
008	DATA EPS	Relative permittivity of materials modeled. User specification begins with data item #4 in list. External air is item #1.
009	DATA SIG	Electric conductivity (mhos/m) of materials modeled. User specification begins with data item #4 in list. Air is item #1.
010	PHI	Angle of incidence (degrees) relative to y axis of grid. Limited to range $0^\circ$ - $90^\circ$ in present program.
011	ISA	FD-TD "i" coordinate of left field matching plane (between total-field and scattered-field regions).

<u>Program Line</u>	<u>Symbol or Data Input</u>	<u>Function</u>
012	ISB	FD-TD "i" coordinate of right field-matching plane (between total-field and scattered-field regions).
013	JSA	FD-TD "j" coordinate of front field-matching plane (between total-field and scattered-field regions).
014	JSB	FD-TD "j" coordinate of back field-matching plane (between total-field and scattered-field regions).
103 - 107	MEZ(I,J)	<p>Assigns a material-medium type number to the <math>E_z</math> field components of the grid that comprise the structure to be modeled. The type number corresponds to the EPS and SIG specifications of program lines 008 and 009. Arbitrary specification is possible simply by using any number of Fortran statements here to make the assignment. In the example shown, a single DO loop suffices to specify that the object is square and has a surface composed of material-medium type #4 (<math>\epsilon_r = 1.0</math>, <math>\sigma = 3.72 \cdot 10^7</math> mhos/meter). The side of the square object is specified to be 20 grid cells across with corners at (16,16), (36,16), (16,36), and (36,36).</p>

```

1001      PROGRAM EDIT (INPUT,END-INPUT,TAPE-NO-INPUT,TAPE-NAME-INPUT)

C
C
C      PROJECT E6502, RUN 5
C      TWO-DIMENSIONAL PROPAGATION, TM POLARIZATION
C      TEST OF NEW PHASE COMPUTATION CONDITION
C      TEST OF NEW CHLIQUE WAVE SOURCE CONDITION
C      TEST OF NEW LATTICE TRUNCATION CONDITION
C      50 X 49 CELL YEE GRID IS USED
C      INDUCED ELECTRIC CURRENTS ON SQUARE METAL CYLINDER
C
1002      REAL MUZ
1003      DIMENSION FZ(51,50),FNZ(51,50),HX(51,50),HY(52,50),WFZ(51,50),
1          FDL(2,50,2),FDH(2,50,2),FDF(51,2,2),FDH(51,2,2),
2          IPR(52),EPS(4),SIG(4),CA(4),CH(4),
3          IPHA(51,50),PA(4),DH(4),FAHX(51,50),FNHY(52,50),
4          IPHHY(51,50),IPHHY(52,50),DFZ(51,50),DHX(51,50),
5          DHY(52,50),WFZ1(50),WFZ2(50),WFZ3(50),WFZ4(50),
6          WHX1(50),WHY2(50),WHY3(50),WHX4(50),FZ1(90),HX1(90)

C
C      .....PROBLEM PARAMETERS.....
004      FREQ = 3.0E+8
005      DX = 1.59155E-2
006      NCYC8 = 6
007      MEDIA = 4
008      DATA EPS /1.0, 1.0, 1.0, 1.0/
009      DATA SIG /0.0, 0.0, 0.0, 3.72E+7/
010      PHT = 45.0

C
C      .....BASIC AND DERIVED CONSTANTS.....
011      ISA = 11
012      ISH = 41
013      JSA = 11
014      JSH = 41

C
015      DMX = FLOAT(ISA) = 0.5
016      DMY = FLOAT(JSA) = 0.5
017      SIDFX = FLOAT(ISH-ISA) + 0.5
018      SIDFY = FLOAT(JSH-JSA) + 0.5
019      ISAA = ISA + 1
020      ISHH = ISH - 1
021      JSAA = JSA + 1
022      JSRH = JSH - 1
023      ISAAA = ISA - 1
024      JSAAA = JSA - 1
025      ISRHH = ISH + 1
026      JSRHH = JSH + 1
027      PI = 3.14159265
028      OMEGA = 2.0 * PI * FREQ
029      SPHI = SIN(PI * PHT / 180.0)
030      CPHI = COS(PI * PHT / 180.0)
031      MUZ = 4.0 * PI * 1.0E-7
032      EPSZ = 8.854E-12
033      DT = DX / 6.0E+8
034      NMIN = 1.0 / FREQ / DT
035      NMID = NMIN
036      NMAX = NCYC8 * NMIN
037      NMINA = FLOAT(NMIN) / 2.0
038      NMIDA = NMINA
039      NMAXA = NCYC8 * 2 * NMINA

```

```

040      W = DT / 2.0 / EPS7
041      WA = DT**2 / DX**2 / MU2 / EPS7
042      RH = DT / DX / MU2
043      RC = 1000.0 / RH
044      WD = OMEGA * DT
045      RF = -360.0 * FREQ * DT
046      RE = 1.0 / RC
047      RG = 1.0 / 3767340.0
048      RH = RH / 10000.0
049      DO 1 I=1,MEDIA
050      FAF = W * SIG(I) / EPS(I)
051      CA(I) = (1.0-FAF) / (1.0+FAF)
052      CH(I) = WA / EPS(I) / (1.0+FAF)
053      HAF = SIG(I)*MU2/EPS7 + DT/2.0/MU2
054      DA(I) = (1.0-HAF) / (1.0+HAF)
055      DH(I) = 1.0 / (1.0+HAF)
056      DO 901 I=ISA,ISP
057      TERM = (F(DAT(I)-DHY) * SPHI
058      REZ1(I) = TERM + 0.5*CPHI - 0.5
059      REZ4(I) = TERM + SIDEV*CPHI - 0.5
060      RHX1(I) = TERM
061      401 RHX4(I) = TERM + (SIDEV+0.5)*CPHI
062      DO 902 J=JSA,JSH
063      TERM = (F(DAT(J)-DRY) * CPHI
064      REZ2(J) = TERM + 0.5*SPHI - 0.5
065      REZ3(J) = TERM + SIDEV*SPHI - 0.5
066      RHV2(J) = TERM
067      902 RHV3(J) = TERM + (SIDEV+0.5)*SPHI

```

C  
C           .....LOAD THE MATRICES.....

```

1068      DO 903 J=1,90
1069      FZ1(J) = 0.0
1070      403 HX1(J) = 0.0
1071      DO 2 J=1,50
1072      DO 2 I=1,51
1073      FZ(1,J) = 0.0
1074      HX(1,J) = 0.0
1075      HY(1,J) = 0.0
1076      ENZ(1,J) = 0.0
1077      DEZ(1,J) = 0.0
1078      FHHX(1,J) = 0.0
1079      DHX(1,J) = 0.0
1080      FHHY(1,J) = 0.0
1081      DHY(1,J) = 0.0
1082      2 MEZ(1,J) = 1
1083      FS22 = 0.0
1084      FS11 = 0.0
1085      ED22 = 0.0
1086      ED11 = 0.0
1087      DO 902 I=ISA,ISP
1088      MEZ(I,JSA) = 2
1089      902 MEZ(I,JSH) = 2
1090      DO 903 J=JSA,JSH
1091      MEZ(ISA,J) = 2
1092      903 MEZ(ISH,J) = 2
1093      DO 803 N=1,2
1094      DO 803 I=1,2
1095      DO 803 J=1,50
1096      FDI(1,J,N) = 0.0
1097      803 EDH(1,J,N) = 0.0

```



```

009A      DO 404 N=1,2
009B      DO 404 J=1,2
0100      DO 404 I=1,51
0101      FDF(I,J,N) = 0.0
0102      404 FDF(I,J,N) = 0.0

C
C      .....SPECIFY THE SCATTERER.....
0103      DO 44 I=16,36
0104      MEZ(I,16) = 4
0105      MEZ(I,36) = 4
0106      MEZ(16,I) = 4
0107      44 MEZ(36,I) = 4

C
C      .....TIME-STEPPING LOOP.....
0108      DO 21 N=1,NMAX
0109      FNMID = F(0.0AT(N) / F(0.0AT(NMID))
0110      NA = N - F(1X(FNMID)*NMID)
0111      JSTOP = 49

C
C      .....F7 ITERATION.....
0112      DO 4 J=2,JSTOP
0113      DO 4 I=2,50
0114      MF = MEZ(I,J)
0115      IF(MF.EQ.2) GO TO 904
0116      STORE = FZ(I,J)
0117      FZ(I,J) = CA(MF)*FZ(I,J) + CH(MF)*(MX(I,J-1)-MX(I,J)+
1          HY(I+1,J)-HY(I,J))
0118      DEZNU = FZ(I,J) - STORE
0119      IF(DEZNU*DEZ(I,J).GT.0.0) GO TO 984
0120      FNZ(I,J) = FZ(I,J)
0121      IF(DEZNU.LT.0.0) IPHA(I,J)ENA
0122      984 DEZ(I,J) = DEZNU
0123      904 CONTINUE
0124      4 CONTINUE
0125      DO 405 J=2,49
0126      405 FZ(I,J) = FZ(I,J) + RA* (HXT(J-1) - HXT(J))

C
C      .....ORLQHF WAVE SOURCE CONDITION (E7).....
0127      EZI(3) = FZ(3) + RA*SIN(HD*F(0.0AT(N))
0128      DO 930 I=ISA,ISHR
0129      L = RHX1(I)
0130      G = L
0131      HXINC = ( (RHX1(I)-G)*HXT(L+6) + (G+1.0-RHX1(I))*HXT(L+5) ) * CPM1
0132      HXT = HX(I,JSAAA) + HXINC
0133      FZ(I,JS4) = FZ(I,JS4) + RA* (HXT-MX(I,JS4)+HY(I+1,JS4)-HY(I,JS4))

C
0134      L = RHX4(I)
0135      G = L
0136      HXINC = ( (RHX4(I)-G)*HXT(L+6) + (G+1.0-RHX4(I))*HXT(L+5) ) * CPM1
0137      HXT = HX(I,JSR) + HXINC
0138      430 FZ(I,JSR) = FZ(I,JSR) + RA* (HXT-MX(I,JSR)-HXT+HY(I+1,JSR)-HY(I,JSR))

C
0139      DO 435 J=JSAAA,ISHH
0140      L = RHV2(J)
0141      G = L
0142      HYINC = -( (RHV2(J)-G)*HXT(L+6) + (G+1.0-RHV2(J))*HXT(L+5) ) * SPM1
0143      HXT = HY(ISA,J) + HYINC
0144      EZ(ISA,J) = FZ(ISA,J) + RA* (HY(ISA,J-1)-MX(ISA,J)+HY(ISA,J)-HXT)

C
0145      L = RHV3(J)

```

```

146      G = L
147      HYINC = -((RHY3(J)-G)*HXT(I+6) + (G+1.0-RHY3(J))*HXT(I+5)) * SPH1
148      HVT = HY(ISHRPH,J) + HYINC
149      FZ(ISH,J) = FZ(ISH,J) + RAO * (HXT(ISH,J-1)-HXT(ISH,J)+HVT-HY(ISH,J))
C
150      I = ISA
151      J = JSA
152      L = RHXT(I)
153      G = L
154      HXINC = ((RHXT(I)-G)*HXT(I+6) + (G+1.0-RHXT(I))*HXT(I+5)) * CPH1
155      HXT = HX(I,JSAAA) + HXINC
156      I = RHY2(J)
157      G = L
158      HYINC = -((RHY2(J)-G)*HXT(I+6) + (G+1.0-RHY2(J))*HXT(I+5)) * SPH1
159      HVT = HY(I,J) + HYINC
160      FZ(I,J) = FZ(I,J) + RAO * (HXT-HX(I,J)+HVT-HY(ISA,J)-HVT)
C
161      I = ISH
162      L = RHXT(I)
163      G = L
164      HXINC = ((RHXT(I)-G)*HXT(I+6) + (G+1.0-RHXT(I))*HXT(I+5)) * CPH1
165      HXT = HX(I,JSAAA) + HXINC
166      I = RHY3(J)
167      G = L
168      HYINC = -((RHY3(J)-G)*HXT(I+6) + (G+1.0-RHY3(J))*HXT(I+5)) * SPH1
169      HVT = HY(ISHHH,J) + HYINC
170      FZ(I,J) = FZ(I,J) + RAO * (HXT-HX(I,J)+HVT-HY(ISH,J)-HVT)
C
171      I = ISA
172      J = JSH
173      L = RHXT(I)
174      G = L
175      HXINC = ((RHXT(I)-G)*HXT(I+6) + (G+1.0-RHXT(I))*HXT(I+5)) * CPH1
176      HXT = HX(I,J) + HXINC
177      I = RHY2(J)
178      G = L
179      HYINC = -((RHY2(J)-G)*HXT(I+6) + (G+1.0-RHY2(J))*HXT(I+5)) * SPH1
180      HVT = HY(I,J) + HYINC
181      FZ(I,J) = FZ(I,J) + RAO * (HXT-HX(ISHHH)-HXT+HVT-HY(ISA,J)-HVT)
C
182      I = ISH
183      L = RHXT(I)
184      G = L
185      HXINC = ((RHXT(I)-G)*HXT(I+6) + (G+1.0-RHXT(I))*HXT(I+5)) * CPH1
186      HXT = HX(I,J) + HXINC
187      I = RHY3(J)
188      G = L
189      HYINC = -((RHY3(J)-G)*HXT(I+6) + (G+1.0-RHY3(J))*HXT(I+5)) * SPH1
190      HVT = HY(ISHHH,J) + HYINC
191      FZ(I,J) = FZ(I,J) + RAO * (HXT-HX(ISHHH)-HXT+HVT-HY(ISH,J)-HVT)
C
C .....FZ SOFT GRID TRUNCATION.....
192      FZ(1) = F822
193      F822 = F811
194      F811 = FZ(2)
C
195      FZ(90) = F822
196      F822 = F811
197      F811 = FZ(90)
C

```

```

198      DO M06 J=2,49
199      FZ(1,J) = -EDL(2,J,2) = 0.33333*(FZ(2,J)+EDL(1,J,2))
      1      +1.16667*(EDL(1,J,1)+EDL(2,J,1))
      2      +0.08333*(EDL(1,J+1,1)+EDL(1,J-1,1)+
      3      EDL(2,J+1,1)+EDL(2,J-1,1))
200      M06 FZ(51,J) = -EDR(2,J,2) = 0.33333*(FZ(50,J)+EDR(1,J,2))
      1      +1.16667*(EDR(1,J,1)+EDR(2,J,1))
      2      +0.08333*(EDR(1,J+1,1)+EDR(1,J-1,1)+
      3      EDR(2,J+1,1)+EDR(2,J-1,1))
201      DO M07 I=2,50
202      FZ(I,1) = -EDF(1,2,2) = 0.33333*(FZ(I,2)+EDF(1,1,2))
      1      +1.16667*(EDF(1,1,1)+EDF(1,2,1))
      2      +0.08333*(EDF(1+1,1,1)+EDF(1-1,1,1)+
      3      EDF(1+1,2,1)+EDF(1-1,2,1))
203      M07 FZ(I,50) = -EDH(1,2,2) = 0.33333*(FZ(I,49)+EDH(1,1,2))
      1      +1.16667*(EDH(1,1,1)+EDH(1,2,1))
      2      +0.08333*(EDH(1+1,1,1)+EDH(1-1,1,1)+
      3      EDH(1+1,2,1)+EDH(1-1,2,1))
C
204      FZ(1,1) = 0.292893*FOL(1,1,2) + 0.707107*FOL(2,2,2)
205      FZ(1,50) = 0.292893*FOL(1,50,2) + 0.707107*FOL(2,49,2)
206      FZ(51,1) = 0.292893*FOL(1,1,2) + 0.707107*FOL(2,2,2)
207      FZ(51,50) = 0.292893*FOL(1,50,2) + 0.707107*FOL(2,49,2)
C
208      DO A16 I=1,2
209      IA = 52 - I
210      DO A16 J=1,50
211      FOL(I,J,2) = FOL(I,J,1)
212      FOL(I,J,1) = FZ(I,J)
213      FOL(I,J,2) = FOL(I,J,1)
214      A16 FOL(I,J,1) = FZ(IA,J)
C
215      DO A17 J=1,2
216      JA = 51 - J
217      DO A17 I=1,51
218      EDF(I,J,2) = EDF(I,J,1)
219      EDF(I,J,1) = FZ(I,J)
220      FOL(I,J,2) = FOL(I,J,1)
221      A17 FOL(I,J,1) = FZ(I,JA)
C
C      .....HX ITERATION.....
222      DO A J=1,JSTOP
223      IFLAG = 0
224      IF(J,FO,JSAAA,CF,J,FO,JSP) IFLAG=1
225      DO A I=1,51
226      IF(IFLAG,FO,1,AND,I,GE,ISA,AND,I,LE,ISH) GO TO A1
227      STORE = HX(I,J)
228      HX(I,J) = HX(I,J) + FZ(I,J) - FZ(I,J+1)
229      DMXN0 = HX(I,J) - STORE
230      IF(DMXN0*DMX(I,J).GT,0.0) GO TO 985
231      ENHX(I,J) = HX(I,J)
232      IF(DMXN0.LT,0.0) IPHX(I,J)=A
233      985 DMX(I,J) = DMXN0
234      61 CONTINUE
235      * CONTINUE
236      DO 90A J=1,89
237      90A HX(I,J) = HX(I,J) + FZ(I,J) - FZ(I,J+1)
C
C      .....DR1 INLE WAVE SOURCE CONDITION (HX).....
238      DO 950 I=ISA,ISP

```

```

239      L = REZ1(I)
240      G = L
241      FZINC = (REZ1(I)-G)*FZ1(I+7) + (G+1.0-REZ1(I))*FZ1(L+6)
242      FZS = FZ(I,JS4) = FZINC
243      HX(I,JSAAA) = HX(I,JSAAA) + FZ(I,JSAAA) = FZS

C
244      L = REZ4(I)
245      G = L
246      FZINC = (REZ4(I)-G)*FZ1(I+7) + (G+1.0-REZ4(I))*FZ1(L+6)
247      FZS = FZ(I,JS4) = FZINC
248      HX(I,JS4) = HX(I,JS4) + FZS = FZ(I,JS4HH)
249      450 CONTINUE

C
C      .....HY ITERATION.....
250      DO 9 J=2,JSTOP
251      IFLAG = 0
252      IF(J,GF,JS4,AND,J,LF,JS4) IFLAG=1
253      DO 9 I=2,51
254      IF(IFLAG,FQ,1,AND,I,FQ,ISA) GO TO 71
255      IF(IFLAG,FQ,1,AND,I,FQ,ISRRH) GO TO 71
256      STORE = HY(I,J)
257      HY(I,J) = HY(I,J) + FZ(I,J) = FZ(I+1,J)
258      DHYNU = HY(I,J) = STORE
259      IF(DHYNU-DHY(I,J),GT,0.0) GO TO 986
260      FHMY(I,J) = HY(I,J)
261      IF(DHYNU,LT,0.0) IFHMY(I,J)=NA
262      986 DHY(I,J) = DHYNU
263      71 CONTINUE
264      9 CONTINUE

C
C      .....ORIGINE WAVE SOURCE CONDITION (HY).....
265      DO 470 J=JS4,JS4
266      L = REZ2(J)
267      G = L
268      FZINC = (REZ2(J)-G)*FZ1(I+7) + (G+1.0-REZ2(J))*FZ1(L+6)
269      FZS = FZ(ISA,J) = FZINC
270      HY(ISA,J) = HY(ISA,J) + FZS = FZ(ISA+1,J)

C
271      L = REZ3(J)
272      G = L
273      FZINC = (REZ3(J)-G)*FZ1(I+7) + (G+1.0-REZ3(J))*FZ1(L+6)
274      FZS = FZ(IS4,J) = FZINC
275      HY(IS4,J) = HY(IS4,J) + FZS = FZ(IS4+1,J)
276      470 CONTINUE

C
C      .....PRINT-OUT ROUTINE.....
C
C      .....PRINT-OUT INTERVAL (ENVELOPE MAGNITUDES).....
277      DO 12 N=NMINA,NMAXA,NMIDA
278      IF(N,FR,K)GO TO 13
279      12 CONTINUE
280      GO TO 20

C
C      .....ENVELOPE OF FZ (MAGNITUDE).....
281      13 DO 14 IA=25,50,25
282      IH = IA = 23
283      IC = IA + 1
284      PRINT 14, N
285      14 FORMAT(1H1,77.53X,24H2 GRID FOR TIME STEP = ,I4,/,2X,1HJ,/)
286      DO 16 JA=1,50

```

```

287      J = 51 = JA
288      DO 15 I=IH,IC
289      IPR(I) = RC * FNZ(I,J)
290      15 FNZ(I,J) = 0.0
291      16 PRINT 17, J, (IPR(I),I=IH,IC)
292      17 FORMAT (1Y,12,1X,25I5)
293      DO 18 I=IH,IC
294      18 IPR(I) = I
295      19 PRINT 19, (IPR(I),I=IH,IC)
296      19 FORMAT (/,4X,25I5,/,67X,1H1)

C
C      .....MY ENVELOPE (MAGNITUDE).....
297      DO 188 IA=25,50,25
298      IH = IA = 23
299      IC = IA + 1
300      PRINT 114, N
301      114 FORMAT (1H1,/,53X,24HHY GRID FOR TIME STEP = ,14,/,2X,1HJ,/)
302      DO 116 JA=1,49
303      J = 50 = JA
304      DO 115 I=IH,IC
305      IPR(I) = 376734.0 * ENMX(I,J)
306      115 ENMX(I,J) = 0.0
307      116 PRINT 17, J, (IPR(I),I=IH,IC)
308      DO 118 I=IH,IC
309      118 IPR(I) = I
310      118 PRINT 19, (IPR(I),I=IH,IC)

C
C      .....MY ENVELOPE (MAGNITUDE).....
311      DO 288 IA=25,50,25
312      IH = IA = 23
313      IC = IA + 1
314      PRINT 214, N
315      214 FORMAT (1H1,/,53X,24HHY GRID FOR TIME STEP = ,14,/,2X,1HJ,/)
316      DO 216 JA=2,49
317      J = 51 = JA
318      DO 215 I=IH,IC
319      IPR(I) = 376734.0 * ENMY(I,J)
320      215 ENMY(I,J) = 0.0
321      216 PRINT 17, J, (IPR(I),I=IH,IC)
322      DO 218 I=IH,IC
323      218 IPR(I) = I
324      288 PRINT 19, (IPR(I),I=IH,IC)

C
C      .....PRINT-OUT INTERVAL (ENVELOPE PHASES).....
325      20 DO 512 K=NMIN,AMAX,NMID
326      IF(N,EO,K) GO TO 513
327      512 CONTINUE
328      GO TO 520

C
C      .....F7 ENVELOPE (PHASE).....
329      513 DO 40 IA=25,50,25
330      IH = IA = 23
331      IC = IA + 1
332      PRINT 24, N
333      24 FORMAT (1H1,/,53X,26HF7PH GRID FOR TIME STEP = ,14,/,2X,1HJ,/)
334      DO 26 JA=1,50
335      J = 51 = JA
336      DO 25 I=IH,IC
337      IPR(I) = FLNAT(IPH(I,J)) * HF
338      IF(AHS(IZ(I,J)),LT,PH) IPR(I)=0

```

```

339      25 IPHA(1,J) = 0
340      26 PRINT 17, J, (IPR(1),I=IH,IC)
341      DO 27 I=IR,IC
342      27 IPR(1) = 1
343      19 PRINT 19, (IPR(1),I=IH,IC)
C
C      .....MY ENVELOPE (PHASE).....
344      DO 189 IAS25,50,25
345      IH = IA = 23
346      IC = IA + 1
347      PRINT 124, N
348      124 FORMAT (1H1,/,53X,26PHXPH GRID FOR TIME STEP = ,14,/,2X,1HJ,/)
349      DO 126 JAS1,49
350      J = 50 = JA
351      DO 125 I=IH,IC
352      IPR(1) = FLOAT(IPHHX(1,J)) * RE
353      IF(AHS(HY(1,J)),17,4G) IPR(1)=0
354      125 IPHHX(1,J) = 0
355      126 PRINT 17, J, (IPR(1),I=IH,IC)
356      DO 127 I=IH,IC
357      127 IPR(1) = 1
358      189 PRINT 19, (IPR(1),I=IR,IC)
C
C      .....MY ENVELOPE (PHASE).....
359      DO 289 IAS25,50,25
360      IH = IA = 23
361      IC = IA + 1
362      PRINT 224, N
363      224 FORMAT (1H1,/,53X,26HHYPH GRID FOR TIME STEP = ,14,/,2X,1HJ,/)
364      DO 226 JAS2,49
365      J = 51 = JA
366      DO 225 I=IH,IC
367      IPR(1) = FLOAT(IPHHY(1,J)) * RE
368      IF(AHS(HY(1,J)),17,4G) IPR(1)=0
369      225 IPHHY(1,J) = 0
370      226 PRINT 17, J, (IPR(1),I=IH,IC)
371      DO 227 I=IH,IC
372      227 IPR(1) = 1
373      289 PRINT 19, (IPR(1),I=IR,IC)
C
374      520 CONTINUE
375      21 CONTINUE
376      STOP
377      END
NO ERRORS

```



## **MISSION of Rome Air Development Center**

RADC plans and executes research, development, test and selected acquisition programs in support of Command, Control Communications and Intelligence (C<sup>3</sup>I) activities. Technical and engineering support within areas of technical competence is provided to ESD Program Offices (POs) and other ESD elements. The principal technical mission areas are communications, electromagnetic guidance and control, surveillance of ground and aerospace objects, intelligence data collection and handling, information system technology, ionospheric propagation, solid state sciences, microwave physics and electronic reliability, maintainability and compatibility.